Title

Theoretical Study of Tellurium Isotope Fractionations in Ore-Forming Systems, and Studies of Doubly Substituted Isotopologues of Methane

Author

Haghnegahdar, Mojhgan

Publication Date

2018

Peer reviewed|Thesis/dissertation

UNIVERSITY OF CALIFORNIA

Los Angeles

Theoretical Study of Tellurium Isotope Fractionations in Ore-Forming Systems, and Studies of Doubly Substituted Isotopologues of Methane

A dissertation submitted in partial satisfaction of the

requirements for the degree Doctor of Philosopy

in Geochemistry

by

Mojhgan Haghnegahdar

2018

ABSTRACT OF THE DISSERTATION

Theoretical Study of Tellurium Isotope Fractionations in Ore-Forming Systems, and Studies of Doubly Substituted Isotopologues of Methane

by

Mojhgan Haghnegahdar

Doctor of Philosophy in Geochemistry

University of California, Los Angeles, 2018

Professor Edwin Arthur Schauble, Chair

This thesis encompasses three research projects on the stable isotopes of tellurium and multiply substituted isotopologues of methane. In the first project (Chapter 2), I used theoretical techniques to predict tellurium isotope signatures of ore formation processes.

In this study, equilibrium mass-dependent isotopic fractionation among Te-bearing species relevant to the formation of precious-metal ores is estimated with first-principles thermodynamic calculations. This work is the first theoretical study on the isotope fractionation of tellurium in ore-forming systems.

In the second project (Chapter3), I investigated the potential of $^{13}CH_3D$ and $^{12}CH_2D_2$, the doubly substituted mass-18 isotopologues of methane, as tools for tracking atmospheric methane sources and sinks. Methane is the most abundant organic chemical

and the second most important long-lived greenhouse gas in the atmosphere. It also has a significant impact on the chemistry of the troposphere and stratosphere. However, there are large uncertainties in the sources and sinks of methane to the atmosphere, as well as in their variability in time and space. I used electronic structure methods and initial isotopologue abundance measurements, from the UCLA Nu Panorama and other laboratories [Stolper et al., 2015; Wang et al., 2015; Young et al., 2017], to estimate kinetic and equilibrium isotope signatures for $^{13}CH_3D$ and $^{12}CH_2D_2$. Then I predicted the abundances of singly and doubly substituted methane species in atmosphere in different scenarios using a whole-atmosphere box model. This study is the first model ever to describe the atmospheric methane budget that includes both doubly substituted isotopologues, $^{13}CH_3D$ and $^{12}CH_2D_2$.

The third project (Chapter 4) focused on measuring $^{13}CH_3D$ and $^{12}CH_2D_2$ in methane samples from natural boreal lakes, collected in Alaska, Canada, and Siberia. Wetlands are among the largest methane sources, and they will need to be characterized as part of the construction of any realistic global budget of $^{13}CH_3D$ and $^{12}CH_2D_2$. In this project all measurements were performed using gas chromatography and a high-resolution gas-source multiple-collector mass spectrometer (the UCLA Nu Panorama).

Finally, these data are combined with recent predictions of future emissions growth to model the likely impacts of boreal lakes on the future atmospheric CH_4 isotopologue budget up to year 2100. In addition to testing our model atmospheric budget, doubly substituted isotopologue measurements of CH_4 appear to provide information about the likely production mechanism for natural CH_4 samples.

This dissertation of Mojhgan Haghnegahdar is approved.

Kevin D McKeegan

Jochen Peter Stutz

Edward Donald Young

Edwin Arthur Schauble, Committee Chair

University of California, Los Angeles

2018

DEDICATION

To the memory of all brave Iranian students, who have been fighting for freedom and democracy in our homeland Iran especially, to those who have given their lives for our dream and will have never had chance to finish their education.

Also, to the loving memory of Reza Shah Pahlavi and Mohammad Reza Shah Pahlavi who were the best thing ever happened to Iranian women.

آباد باش ای **ایران**
آزاد باش ای **ایران**
ازما فرزندان خود
دلشاد باش ای **ایران**

Table of Contents

Chapter 3:

A Model for $^{12}CH_2D_2$ and $^{13}CH_3D$ as Complementary Tracers for the Budget of Atmospheric CH_4

List of Figures

Chapter 2

Chapter 3

Chapter 4

List of Tables

Chapter 2

Chapter 3

Chapter 4

ACKNOWLEDGEMENTS

I would like to give my special thanks to my advisor Prof. Edwin Schauble for all his guidance and support. During my years at UCLA, Edwin has patiently taught me and enlightened me how to be a better scientist. I would not have been able to complete my PhD without his consistent support. Taking the isotope geochemistry course with Edwin was the best thing that happened to me during my entire education. That course changed my life. I am grateful to Edwin for trusting me and accepting me as his PhD student. Also, I am thankful to him for always encouraging me to work on the subjects that I have been passionate about. Due to his support and encouragement, I have had the opportunity working on such a diverse range of projects. I am particularly grateful to Edwin for encouraging me to work on methane clumped isotopes and to get involved with the Panorama lab.

Also, I want to thank Edward Young for giving me the opportunity to collaborate with him on methane clumped isotopes. I greatly appreciate Ed's generosity and keeping his door open along with his timely advice and support.

I am thankful to both Edwin and Ed for their trust, support, encouragement, advice, thoughtful comments, and most importantly being interested in my ideas of working on atmospheric methane. I have been very fortunate to have the opportunity of working closely with two different types of excellent scientists on a very diverse range of research subjects and from different aspects. No words can describe how much I am grateful to Edwin and Ed for being there for me all these years and all the opportunities

they have provided me, including attending various domestic and international conferences and workshops during my PhD.

I also would like to express my sincere gratitude to the other members of my thesis committee, Prof. Kevin McKeegan, and Prof. Jochen Stutz for their support, and wonderful advice. All the great suggestions made by my committee members enriched my thesis.

I am grateful to Pamela Hill for all her help. She is such a great mentor and source of support. I have learned from Pam what kind of attitude is required by a scientist to encourage others and have an impact on them. Also, I would like to thank Alexander Sedlak for all his help and support. I am so happy that he decided to join our group for pursuing his PhD. I feel lucky having Alex in our group for the past three years.

It would not be possible for me to complete my PhD without so much help and encouragement from my friends and colleagues at EPSS. I would especially like to thank the former and current members of Ed Young's group for treating me as one of them. I appreciate all the support I have received from Michelle Jordan, Kaitlyn McCain, Alexandra Schneider, Haolan Tang, Jabrane Labidi, and Issaku Kohl. Additionally, I am thankful to my collaborators Issaku and Jabrane for helping and training me to use the vacuum line and the Panorama.

I want to also thank my other co-authors and collaborators who have contributed greatly to the development of my research: Paul Spry and Andrew Fornadel at Iowa State University; Katey Walter Anthony at University of Alaska Fairbanks; and Matthias

Winkel at GFZ German Research Centre for Geosciences. I am grateful for the generosity of Katey who provided me natural methane samples from various boreal lakes. In addition, I want to thank Douglas Rumble, and Kevin McKeegan. Though, we have not collaborated directly I have always benefited from their support and guidance.

Additionally, I would like to thank the Earth, Planetary, and Space Sciences department personnel and staff for their unflagging support. Throughout my time here at UCLA, I will always appreciate this opportunity and the many experiences I have had with the people I have met and worked with, and the friendships that have been established. My gratitude extends to the professors, graduate advisors and chairs of the Earth, Planetary, and Space Sciences department with whom I interacted and who taught me so much. I appreciate everyone who has helped me through my journey as a PhD student at EPSS. I would have not been able to do it without them. I am grateful to Lauri Holbrook for supporting me from the very first day that I decided to join EPSS, as well as to Kathleen Micham, Carlene Brown, Hilda Avanesian, Micheal Rathjen, and Elyse Chou. Additionally, my work at UCLA would not have been as enjoyable without constant interaction with graduate students and postdoctoral scholars. I am grateful to all who made my work at UCLA enjoyable and unforgettable, especially my friends at EPSS and AOS. It is impossible to list them all here. But I would like to thank all former and current EPSS graduate students, post doctoral scholars, researchers, staff, and faculty who have been like a family to me for their continuing kindness, support, and encouragements. I have had a lot of fun and precious memories from my time at UCLA. Thanks especially to Cigdem Akan, Zeyneb Kurt, Christine Gabrielse Lin, Beatriz Gallardo-Lacourt, Jennifer Scully, Elizabeth Palmer, Junko Isa, Patrick Boehnke,

Elizabeth Bell, Amanda Garcia, Bryce Mitsunaga, Ellen Harju, Michelle Jordan, Richard Hart, Elizabeth McKenzi, Emily Hawkins, Michaela Villarreal, Kynan Hughson, Alexander Sedlak, Kaitlyn McCain, Alexandra Schneider, Matthew Walker, Sean Faulk, Erin Leonard, Raquel Nuno, Deborah Weiser, Haolan Tang, Christopher Snead, Ellen Alexander, Heather Kirkpatrick, Tersi Arias, Ashley Schoenfeld, Carolyn Crow, Daniel Fineman, and Erik Weidner.

And last I would like to thank my family, especially my dad, for their faith in me. I am grateful that you have supported me and let me pursue my dreams.

Mojhgan Arianna Haghnegahdar

Los Angeles, California

2018

Vita

Mojhgan A. Haghnegahdar

Education

University of California, Los Angeles (UCLA)
- Master of Science in Geochemistry

California State University, Northridge (CSUN)
- Master of Science in Chemistry

M.S. Thesis**:** Quantitation of Estrogen Receptor Alpha mRNA in MCF-7 Breast Cancer Cell Line by Real-Time Reverse Transcriptase-Polymerase Chain Reaction (RT-PCR)

Shiraz University
- Bachelor of Science in Chemistry

Additional Training
- NASA Astrobiology Institute: 2018 International Summer School in Astrobiology, "Biomarkers: Signs of Life Through Space and Time", Universidad Internacional Menendez Pelayo (UIMP), Scholarship Recipient, Palacio de la Magdelena, Santander

Professional Experience

University of California, Los Angeles (UCLA)
- Research Assistant - Earth, Planetary, and Space Sciences Department (advisor: Prof. Edwin Schauble; other supervisory faculty: Prof. Edward Young)

California State University, Northridge (CSUN)
- Research Assistant - Chemistry and Biochemistry Department (advisors: Prof. Jheem Medh; and Prof. Sheri Lillard)

Shiraz University
- Director of Administrative Affairs & Computer Center in Students Affair Department

TeachingExperience

University of California, Los Angeles (UCLA)
- Teaching Assistant: Introduction to Earth Science (1 time), Introduction to Oceanography, Blue Planet (3 times), Dinosaurs and their Relatives (2 times), Solar System and Planets (1 time)

California State University, Northridge (CSUN)
- Chemistry Lab Instructor: General Chemistry, Introduction to Chemistry

Razi High School
- Science Teacher

Selected Honors and Distinctions
- 2018 EPSS Outreach Award (awarded for excellence in education and public outreach)
- 1st Place Winner (team) - 2018 NASA (Astrobiology) PWR competition

- Full funded by NASA to attend The 2018 International Summer School in Astrobiology
- Full funded by NASA Astrobiology Graduate Conference to attend 2018 PWR, and 2018 AbGradcon
- 2nd Place Winner - 2014 UCLA Earth, Planetary, and Space Sciences Student Research Symposium (Poster)
- Geochemical Society Student Travel Award to attend Goldschmidt 2015, Prague
- UCLA EPSS Department Fellowship: Winter 2013, Spring 2014, and Fall 2014
- UCLA Travel Fellowship: Winter 2014, and Summer 2014
- AGU (American Geophysical Union) Student Travel Award (AGU 2013)

Publications

1- A model for $^{12}C_2D_2$ and $^{13}CH_3D$ as complementary tracers for the budget of Atmospheric CH_4, M.A. Haghnegahdar, E.A. Schauble, E.D. Young, 2017, *Global Biogeochemical Cycles*, 31,9:1387-1407

2- Stable Te isotope fractionation in tellurium-bearing minerals from precious metal hydrothermal ore deposits; A.P.Fornadel, P.G.Spry, M. A. Haghnegahdar,E. A. Schauble, S.E.Jackson, S.J.Mills, 2017, *Geochimica et Cosmochimica Acta*, 202, 215-230

3- The relative abundances of resolved $^{12}C_2D_2$ and $^{13}CH_3D$ and mechanisms controlling isotopic bond ordering in abiotic and biotic methane gases; E.D. Young, I.E. Kohl, B. Sherwood Lollar, G. Etiope, D. Rumble III, S. Li (李姝 宁), M.A. Haghnegahdar, E.A. Schauble, K.A. McCain, D.I. Foustoukos,C. Sutclife, O. Warr, C.J. Ballentine, T.C. Onstott, H. Hosgormez, A. Neubeck, J.M. Marques, I. Pérez-Rodríguez, A.R. Rowe, D.E. LaRowe, C. Magnabosco, Laurence Y. Yeung, Jeanine L. Ash, L.T. Bryndzia, 2017, *Geochimica et Cosmochimica Acta*, 203, 235-264

Manuscripts in Preparation

1- First-principles Models of Equilibrium Tellurium Isotope Fractionation, M. A. Haghnegahdar, E. A.Schauble, P.G. Spry, A.P. Fornadel

2- Effects of Boreal Lake Wetlands on Atmospheric $^{12}C_2D_2$ and $^{13}CH_3D$, M.A. Haghnegahdar, E.A. Schauble, J. Labidi, I. Kohl, K. Walter Anthony, M. Winkel, and E.D. Young

Conference Presentations

- 2018 Goldschmidt Conference (Talk)
- 2018 AbGradCon (Talk)
- 2018 Southern California Geobiology Symposium (Talk)
- 2017 Goldschmidt Conference (Talk)
- 2017 AGU Fall Meeting (Poster)
- 2016 AGU Fall Meeting (Poster)
- 2015 AGU Fall Meeting (Poster)
- 2015 Goldschmidt Conference (Poster)
- 2014 Goldschmidt Conference (Poster)
- 2013 AGU Fall Meeting (Poster)

Invited Talk

- Caltech Geoclub (April 2018)

Chapter 1. Introduction

Stable isotope abundances have been commonly used as geochemical tracking tools. Traditional stable isotope analysis focuses on the isotopes of the light elements, including H, C, N, O, and S [Valley et al., 2001], whereas non-traditional stable isotope geochemistry usually involves isotopes of heavier elements. The extension of stable isotope geochemistry to heavier elements has been greatly aided by the development of multi-collector inductively coupled plasma mass spectrometry (MC-ICPMS) [Schauble, 2004]. Factors expected to control the degree of isotope fractionation in traditional and non-conventional stable isotopes in various processes include: the relative mass difference between isotopes, volatility, changes in oxidation state, and sensitivity to biological factors. Stable isotopes, traditional and non-traditional, have had a wide range of applications in geology and geochemistry.

Additionally, stable isotopes have been valuable tools for solving biogeochemical problems including environmental and atmospheric analysis. Stable isotopes can track both sources and sinks of biologically significant elements and molecules helping geochemists to understand the global cycles of elements such as carbon and nitrogen.

1.1 Introduction to chapter 2

Chapter 2 presents a theoretical study of equilibrium stable isotope fractionation for tellurium. The goal of this chapter is to model tellurium isotope signatures relevant to ore formation process, especially in gold deposits. Recent developments in analytical instruments, including MC-ICP-MS, have made measurements on tellurium possible in both terrestrial and meteorite samples [Fornadel et al., 2014 and 2017; Fehr et al., 2005, 2009, and 2018, Moynier et al., 2009].

The motivation for this work is investigate whether tellurium isotope

geochemistry can shed light on the formation process of epithermal and orogenic gold telluride-bearing deposits, and thus indirectly on gold mineralogy. Tellurium (Te) bonds with gold (Au) in more minerals than any other element, however the formation and transport process for bringing Te and Au to the site of mineralization still are not clear. The focus of this study is tellurides [compounds with Te (-II)], which are most common in magmatic and hydrothermal ore deposits, along with gas phase species. Prior to this study, the theoretical study on isotope fractionation of tellurium goes back to 1968 and was limited to several gas molecules [Smithers and Krouse; 1968]. The present study benefited from advice given by Edwin Schauble. Edwin Schauble also performed the PBC model calculations as well as writing the related section. In addition, this work is part of a collaboration with Paul Spry and Andrew Fornadel from Iowa state university, who made Te isotope measurements on minerals. Two manuscripts have already been published on the measurements [Fornadel et al., 2014; and 2017]. Some initial results of the theoretical study have also been published as part of a paper led by our collaborators [Fornadel et al., 2017]. We plan to publish this chapter separately.

1.1.1 Equilibrium stable isotope fractionation

When a chemical process induces isotopic fractionations, isotopic signature can be a potential tool for learning about that process.

For the general case of thermodynamic equilibrium involving with isotope exchange reaction between two substances, for instance XA and XB [Schauble, 2004]

$$^{light}XA + {}^{heavy}XB \leftrightarrows {}^{heavy}XA + {}^{light}XB. \quad (1)$$

The equilibrium constant (K_{eq}) for the above reaction is:

$$K_{eq} = \frac{(^{heavy}_{XA})\,(^{light}_{XB})}{(^{light}_{XA})\,(^{heavy}_{XB})} = \frac{R_{XA}}{R_{XB}}. \quad (2)$$

The isotope fractionation factor (α) for $^{light}X/^{heavy}X$ between two substances XA and XB is defined as the ratio of the two isotope ratios

$$\alpha_{XA-XB} = \frac{R_{XA}}{R_{XB}}. \quad (3)$$

Therefore, α is related to K_{eq} for isotope exchange reactions (as long as one atom is exchanged and symmetry numbers are ignored):

$$K_{eq} = \alpha_{XA-XB}\,. \quad (4)$$

A simplified equation for estimating mass-dependent fractionation assuming rigid rotation and harmonic vibrations only needs frequencies:

$$\beta = \prod_{i=1}^{3n-6} \frac{U_i^*}{U_i} \exp\left(\frac{U_i - U_i^*}{2}\right) \frac{1-\exp(-U_i)}{1-\exp(-U_i^*)} \quad \text{[Bigeleisen \& Mayer, 1947]. (5)}$$

In this equation, β (the reduced partition function ratio between the isotopic forms) is the fractionation factor of the molecule relative to an ideal atomic gas, *n* is the number of atoms in the molecule, *3n-6* is the number of vibrational frequencies in the molecule (for a linear molecule it is *3n-5*), U_i is $\frac{h\nu}{k_B T}$ for the *i*th vibrational mode (*h* is Planck's constant, *v* is vibrational frequency, k_B is Boltzman's constant), and U_i* is the analogous term for the molecule substituted with a heavier isotope. A fractionation factor (α) between two substances A and B can be calculated using reduced partition function ratios (β) as:

$$\alpha = \frac{\beta_A}{\beta_B}. \quad (6)$$

As a quantum mechanical phenomenon, equilibrium mass-dependent isotopic fractionation is primarily determined by changes in molecular and crystalline vibrational

frequencies when one isotope is substituted for another [Urey, 1947]. However, measurements of vibrational frequencies have been limited mostly to simple molecules, as vibrational frequencies are often hard to measure for natural and complicated systems, including minerals and crystals. First-principles methods have been able to provide theoretical estimation of the frequencies for molecules with even more than 100 atoms.

1.2 Introduction to chapter 3 and 4

The later parts of this thesis (chapters 3 and 4) focus on the study of doubly substituted isotopologues of atmospheric methane. The overarching goal is to use $^{13}CH_3D$ and $^{12}CH_2D_2$ to track the methane budget in the atmosphere, including sources and sinks, and their variability in time and space. For instance, recent increases in atmospheric methane concentrations could be caused by increased emission, decreases in •OH that reacts with CH_4 to remove it from the atmosphere, or a combination of both. Therefore, tracing atmospheric methane and developing a model based on its chemical behavior in the atmosphere could be useful for studies of climate and atmospheric chemistry. Identifying atmospheric methane sources and sinks could help understand and ultimately control CH_4 emission to the atmosphere. The work described in the last two chapters is motivated chiefly by the recent discovery of clumped isotope signatures of methane. High-precision isotopic measurements are now possible for not only all elements on the periodic table, but also for doubly substituted isotopologues of molecules such as methane. Doubly substituted methane isotopologue signatures are a potential tool for distinguishing between methane sources [Ma et al., 2008; Stolper et al., 2014a; Wang et al., 2015; Young et al., 2016, 2017; Haghnegahdar et al., 2017].

The consequence of increasing atmospheric methane concentration on global climate is an important social concern. Although the magnitudes of various sources and sinks in the global methane budget have been estimated, there are still considerable uncertainties in individual sources and their rates of change, especially during recent decades. More work is needed to reliably characterize sources and sinks. Chapter 3 and 4 of this thesis investigate the potential of using $^{13}CH_3D$ and $^{12}CH_2D_2$ abundances in the atmosphere as a new tool to track atmospheric methane sources and sinks. Chapter 3 has been published as a manuscript [Haghnegahdar et al., 2017]. This work has benefited from advice given by Edwin Schauble and Edward Young, who are the co-authors of the published manuscript.

Wetlands are among the largest methane sources. The goal of this final chapter is to better understand the atmospheric global budget by measuring $^{13}CH_3D$ and $^{12}CH_2D_2$ in natural methane samples from boreal wetlands (using the UCLA Nu Panorama). We then combine the data with recent predictions of future emissions growth to model the likely impacts of boreal lakes on the future atmospheric CH_4 isotopologue budget up to year 2100. Methane samples analyzed in this work were collected from high latitude lakes by Katey Walter Anthony (from University of Alaska Fairbanks). Samples were measured with the help of Issaku Kohl and Jabrane Labidi. Potential electron acceptors in various depths of two of the lakes in Alaska, were evaluated by Matthias Winkel (GFZ German Research Centre for Geosciences). This study has benefited from advice given by Edwin Schauble and Edward Young, and also collaboration with Katey Walter Anthony, Issaku Kohl, and Jabrane Labidi, and Matthias Winkel who are all co-authors on the manuscript that is being prepared based on this chapter.

1.2.1 Singly and doubly substituted isotope signatures

The δ and Δ for methane isotopologues in ‰ are:

$$\delta^i = \left(\frac{{}^iR_{sample}}{{}^iR_{standard}} - 1\right)(1000‰) \quad (7)$$

$$\Delta_j = \left(\frac{{}^jR_{sample}}{{}^jR_{stochastic}} - 1\right)(1000‰) \quad (8)$$

where R represents abundance ratios $^{13}CH_3D/^{12}CH_4$ or $^{12}CH_2D_2/^{12}CH_4$ for a sample, standard (Standard Mean Ocean Water (SMOW) for hydrogen and Pee Dee Belemnite (PDB) for carbon) , or stochastic equivalent. D/H and $^{13}C/^{12}C$ ratios for the stochastic reference for each gas are calculated solely from the abundance ratios $^{12}CH_3D/^{12}CH_4$ and $^{13}CH_4/^{12}CH_4$, i.e. D/H=1/4($^{12}CH_3D/^{12}CH_4$) and $^{13}C/^{12}C=^{13}CH_4/^{12}CH_4$ as explained below. $X^{13}C$ and X(D) are respectively, the fraction of ^{13}C and D:

$$X^{13}C = \frac{{}^{13}C}{{}^{13}C + {}^{12}C} \quad (9)$$

$$X(D) = \frac{D}{D+H} \ . \quad (10)$$

The random distribution of methane isotopologues are estimated probabilistically as:

$$X(^{12}CH_4) = X(^{12}C)(X(H))^4 \quad (11)$$

$$X(^{13}CH_4) = X(^{13}C)(X(H))^4 \quad (12)$$

$$X(^{12}CH_3D) = 4X(^{12}C)(X(H))^3(X(D)) \quad (13)$$

$$X(^{13}CH_3D) = 4X(^{13}C)(X(H))^3(X(D)) \quad (14)$$

$$X(^{12}CH_2D_2) = 6X(^{12}C)(X(H))^2(X(D))^2 . \quad (15)$$

For the exchange reactions, equilibrium abundances of isotopologues are calculated assuming harmonic vibrations and rigid rotation:

$$^{13}CH_4 + {}^{12}CH_3D \rightleftharpoons {}^{12}CH_4 + {}^{13}CH_3D \quad (16)$$

$$K_{eq} = \frac{[^{13}CH_3D][^{12}CH_4]}{[^{13}CH_4][^{12}CH_3D]} \quad (17)$$

and

$$2\ ^{12}CH_3D \rightleftharpoons\ ^{12}CH_4 + {}^{12}CH_2D_2 \quad (18)$$

$$K_{eq} = \frac{[^{12}CH_2D_2][^{12}CH_4]}{[^{12}CH_3D]^2}\ . \quad (19)$$

By substituting the fractional abundences (Eqs. 11, to 15) in Eqs. 17 and 19, K_{eq} can be evaluated as:

$$K_{eq} = \frac{4X(^{13}C)(X(H))^3(X(D))\ X(^{12}C)(X(H))^4}{4X(^{12}C)(X(H))^3(X(D))\ X(^{13}C)(X(H))^4} = 1 \quad (20)$$

and

$$K_{eq} = \frac{6X(^{12}C)(X(H))^2(X(D))^2\ X(^{12}C)(X(H))^4}{4X(^{12}C)(X(H))^3(X(D))\ 4X(^{12}C)(X(H))^3(X(D))} = \frac{6}{16} = \frac{3}{8} \quad (21)$$

These equilibrium constants are sensitive to temperature, with $K_{eq}(^{13}CH_3D) \approx 1.007$ and $K_{eq}(^{12}CH_2D_2) \approx 1.02 \times (3/8)$ at ~300K, where $K_{eq}(^{12}CH_2D_2) = 3/8$ represents the stochastic distribution of isotopologues.

All electronic structure calculations in this thesis are made using the Gaussian09 software package (Gaussian 09: AM6 4 L-G09RevB.01 12 August 2010) on the UCLA Hoffman2 cluster.

References:

Bigeleisen, J., Mayer, M.G., 1947. Calculations of Equilibrium Constants for Isotopic Exchange Reactions. *J. Chem. Phys.* 261, 261–267.

Fehr, M.A., Hammond, S.J., Parkinson, I.J., 2018. Tellurium stable isotope fractionation in chondritic meteorites and some terrestrial samples. *Geochim. Cosmochim. Acta* 222, 17–33.

Fehr, M.A., Rehkämper, M., Halliday, A.N., 2004. Application of MC-ICPMS to the precise determination of tellurium isotope compositions in chondrites , iron meteorites and sulfides 232, 83–94.

Fornadel, A.P., Spry, P.G., Haghnegahdar, M.A., Schauble, E.A., Jackson, S.E., Mills, S.J.,2017. Stable Te isotope fractionation in tellurium-bearing minerals from precious metal hydrothermal ore deposits. Geochim. *Cosmochim. Acta* 202, 215-230.

Fornadel, A.P., Spry, P.G., Jackson, S.E., Mathur, R.D., Chapman, J.B., Girard, I., 2014. Methods for the determination of stable Te isotopes of minerals in the system Au–Ag–Te by MC-ICP-MS. *J. Anal. At. Spectrom.* 29, 623.

Haghnegahdar, M.A., Schauble, E.A., Young, E.D., 2017. A model For $^{12}CH_2D_2$ and $^{13}CH_3D$ as complementary tracers for the budget of atmospheric CH_4. Global Biogeochem. Cycles 31, 1387–1407. doi:10.1002/2017GB005655

Ma, Q., Wu, S., Tang, Y., 2008. Formation and abundance of doubly-substituted methane isotopologues ($^{13}CH_3D$) in natural gas systems. Geochim. Cosmochim. Acta 72, 5446 –5456. doi:10.1016/j.gca.2008.08.014

Moynier, F., Fujii, T., Albarede, F., 2009. Nuclear field shift effect as a possible cause of Te isotopic anomalies in the early solar system—An alternative explanation of Fehr et al. (2006 and 2009). *Meteoritics & Planetary Science*, *44*(Nr 11), 1735–1742.

Schauble, E. A., 2004. Fractionation Theory to New Systems. *Reviews in Mineralogy & Geochemistry*, *55*, 65–111.

Smithers, R.M., Krouse, H.R., 1968. Tellurium isotope fractionation study. *Can. J. Chem.* 46, 583–591.

Stolper, D.A., Lawson, M., Davis, C.L., Ferreira, A.A., Santos Neto, E. V, Ellis, G.S., Lewan, M.D., Martini, A.M., Tang, Y., Schoell, M., Sessions, A.L., Eiler, J.M., 2014. Formation temperatures of thermogenic and biogenic methane. Science 344, 1500–3. doi:10.1126/science.1254509

Stolper, D.A., Martini, A.M., Clog, M., Douglas, P.M., Shusta, S.S., Valentine, D.L., Sessions, A.L., Eiler, J.M., 2015. Distinguishing and understanding thermogenic and biogenic sources of methane using multiply substituted isotopologues. Geochim. Cosmochim. Acta 161, 219–247. doi:10.1016/j.gca.2015.04.015

Urey H. C., 1947. The thermodynamic properties of isotopic substances. J. Chem. Soc. (London), 562-581

Valley, J. W., Cole, D. R., Biical, M., Iietnr, S. C., 2001. Stable isotope Geochemistry Reviews in Mineralogy & Geochemistry, 43, 1–658.

Wang, D.T., Gruen, D.S., Lollar, B.S., Hinrichs, K.-U., Stewart, L.C., Holden, J.F., Hristov, A.N., Pohlman, J.W., Morrill, P.L., Könneke, M., Delwiche, K.B., Reeves, E.P., Sutcliffe, C.N., Ritter, D.J., Seewald, J.S., McIntosh, J.C., Hemond, H.F., Kubo, M.D., Cardace, D., Hoehler, T.M., Ono, S., 2015. Methane cycling. Nonequilibrium clumped isotope signals in microbial methane. Science 348, 428–31. doi:10.1126/science.aaa4326

Young, E.D., Rumble, D., Freedman, P., Mills, M., 2016. A large-radius high-mass-resolution multiple-collector isotope ratio mass spectrometer for analysis of rare isotopologues of O_2, N_2, CH_4 and other gases. Int. J. Mass Spectrom. 401, 1–10. doi:10.1016/j.ijms.2016.01.006

Young, E.D., Kohl, I.E., Sherwood Lollar, B., Etiope, G., Rumble III, D., Li, S., Haghnegahdar, M. a., Schauble, E. a., Mccain, K. a, Foustoukos, D.I., Sutclife, C.,Warr, O., Onstott, T.C., Hosgormez, H., Neubeck, a, Marques, J.M., Rowe, R., Larowe, D.E., Bryndzia, T., 2017. The relative abundances of resolved $^{12}CH_2D_2$ and $^{13}CH_3D$ and mechanisms controlling isotopic bond ordering in abiotic and biotic methane gases. Geochim. Cosmochim. Acta 203, 235–264. doi:10.1016/j.gca.2016.12.041

Chapter 2. First-principles Models of Equilibrium Tellurium Isotope Fractionation

Abstract

We present theoretical models of tellurium isotope signatures, which are of interest as geochemical tracers for ore forming processes. Tellurium has a unique crystal-chemical role as a bond partner for gold and silver in epithermal and orogenic gold deposits. We predict $^{130}Te/^{125}Te$ isotope fractionations in representative tellurium-bearing species and crystals of varying complexity and chemistry, combining gas-phase calculations with supermolecular cluster models of aqueous and solid species. These in turn are compared with plane-wave density functional theory calculations with periodic boundary conditions. In general, $^{heavy}Te/^{light}Te$ is predicted to be higher for more oxidized species, and lower for reduced species, with $^{130}Te/^{125}Te$ fractionations as large as 3‰ at 100^{o}C between coexisting Te (IV) and Te (-II) or Te (0) compounds. We compare the predicted fractionations with observed isotopic compositions, however, these data are not well suited make any conclusive statements about fractionation processes. More focused experimental investigations on naturally occurring redox pairs (i.e., Te (0) or Te (-II) vs. Te (IV) species) are needed.

1. Introduction

In this study, we model equilibrium $^{130}Te/^{125}Te$ isotope fractionations in naturally occurring tellurides and tellurium species, to investigate their potential as a geochemical tool to understand gold ore formation.

Understanding ore formation has always been an important research area in geochemistry. Isotopic signatures of some members of the chalcogen group, including sulfur and selenium, have already been used as geochemical tracers to better understand the process of ore formation [e.g., Fry, 1988; Johnson, 2004; Cook et al., 2009]. Their broad range of oxidation states and bond partners are important factors making them favorable for these studies [Li and Liu, 2011]. However, the isotopic behavior of tellurium, the heaviest stable chalcogen, is largely unstudied [Smithers and Krouse, 1968; Fehr et al., 2004; 2018; Fornadel et al., 2014; 2017].

Tellurium, with atomic number 52, is located below selenium in the chalcogen group. It has an outer electron configuration of $5s^2\ 5p^4$ in its neutral atomic ground state. Tellurium has eight naturally occurring stable isotopes: ^{120}Te(0.09%), ^{122}Te(2.5%), ^{123}Te(0.9%), ^{124}Te(4.6%), ^{125}Te(7.0%), ^{126}Te(18.7%), ^{128}Te(31.8%), and ^{130}Te(34.5%), and forms inorganic and organic compounds with oxidation states (-II), (-I), (0), (+II), (+IV), and (VI) [Chivers and Laitinen, 2015; Knockaert, 2012].

With an estimated crustal abundance of 1μg/kg [Grundler et al., 2013], tellurium is one of the rarest stable solid elements in the Earth's crust and ocean water; however, its cosmic abundance is as great or greater than that of any other element with an atomic number higher than 40 [Cohen, 1984; Grundler et al., 2013]. Te (VI) and Te (IV) are the most thermodynamically stable oxidation states at the Earth's surface [Chasteen et al.,

2009]. Tellurium has a scavenging-type distribution in the ocean; occurring predominantly as Te (VI). This means thermodynamically stable Te (IV) is less abundant than Te (VI) in ocean water because of preferential scavenging of Te (IV) by FeOOH in Fe-Mn crusts and colloids in the water column [Hein et al., 2003].

Tellurium is most characteristically found as tellurides in ore deposits, More than 50 different Te-bearing minerals have been identified [Lueth et al., 2015]. Tellurides, (Te (-I, -II)) and native tellurium (Te (0)) are found in primary hypogene deposits, whereas tellurates (Te (VI) and Te (IV)) occur in secondary supergene deposits. Secondary Te minerals are relatively rare due to the high stability of native tellurium and many tellurides in weathering environments [Lueth et al., 2016]. The association of tellurium with gold is well recognized. In epithermal gold deposits a substantial amount of gold is chemically bound with tellurium in addition to being found in the native form [Nikolaev et al., 2013; Grundler et al., 2013]. An example is the Kalgoorlie gold mines, one of the largest gold system in the world, with more than 1,457 tons of gold deposits [Shackleton et al., 2003]. The Golden Mile deposit, Kalgoorlie, Australia, tellurides are responsible for approximately 20% of gold production, in the form of at least 19 tellurium-bearing minerals including the precious metal tellurides, calaverite, krennerite, sylvanite stützite, petzite, hessite, montbrayite, and nagyagite [Shackleton et al., 2003].

Tellurides of different elements including Au, Ag, Bi, Pb are reported as trace minerals in gold deposits [Ciobanu et al., 2006]. This association, along with high Te:Au ratios in many hydrothermal ores, suggests that hydrothermal fluids can carry significant amounts of Te [Grundler et al., 2013]. Although it is known that gold telluride deposits generally result from low temperature ($<300^{o}C$) hydrothermal processes, the mechanism

of telluride precipitation is still unclear [Cook, 2009]. Cooke and McPhail [2001] proposed vapor phase transport of Te, with condensation of Te_2 (g) and H_2Te (g) into precious metal tellurides as a possible mechanism for telluride precipitation. In this model, the phase change process during evolution, separation, and re-condensation of the vapor phase could induce an isotopic signature on Te. On the other hand, aqueous Te (IV) species such as H_2TeO_3 may play a role in transportation of tellurium to form Te (-II)-bearing crystals in epithermal and orogenic gold deposits as the dominant Te-bearing species in hydrothermal solutions [Grundler et. al., 2013]. Based on this model, if Te in hydrothermal fluids is transported as Te (IV) species, then a reduction process could be responsible for the formation of Au-tellurides. In this case, strong isotopic fractionation could result from the reduction of mobile Te (IV) species to Te (-II), (-I), and (0) in crystals. A third possibility is that Te is transported in reduced form in the liquid phase, for instance in the form of polytelluride complexes (Te_2^{2-}), and is then precipitated as Au-tellurides during cooling of hydrothermal fluids [Grundler et. al., 2013]. This would involve more subtle or only partial redox reaction for Te, and large isotopic fractionations would not be expected in this scenario. Therefore, isotope fractionation of tellurium may be a good tool for tracing the transport process. Recent developments in analytical chemistry have made precise isotope measurements of Te possible. Tellurium isotope variations have been studied in both terrestrial and meteorite samples [Fornadel et al., 2014; 2017; Fehr et al., 2005; 2009; 2018; Moynier et al., 2009].

There is no recent theoretical study on the isotope fractionation of tellurium in ore-forming systems. Published thermodynamic models of tellurium isotope fractionations have been limited to small gas-phase molecules, including a few charged

molecules analogous to aqueous species, with no direct modeling of crystals or more complex molecules. Previous theoretical calculations indicate that Te-isotopic fractionation is sensitive to differences in bond partner, bond stiffness, coordination number, bond length, and oxidation state [Bigeleisen and Mayer, 1947; Smithers and Krouse, 1968]. In order to better understand potential isotopic signatures of Te-transport, reaction, and precipitation, we use first-principles theoretical models to estimate isotope fractionations between different tellurium-bearing crystals, along with gas and aqueous species, mainly using hybrid density functional theory (B3LYP) [Becke, 1993]. These in turn are compared with isotope fractionations estimated with plane-wave density functional theory using periodic boundary conditions. We expanded our study to different tellurides to shed light on the effective factors on tellurium fractionation in these types of crystals including different structural properties, bond lengths, and oxidation states.

2. Methods

We model mass-dependent fractionation following the standard approach, i. e. assuming harmonic vibrations

$$\beta = \prod_{i=1}^{3n-6} \frac{U_i^*}{U_i} \exp\left(\frac{U_i - U_i^*}{2}\right) \frac{1-\exp(-U_i)}{1-\exp(-U_i^*)}$$ [Bigeleisen and Mayer, 1947].

In this equation, β is the fractionation factor of the molecule relative to an ideal gas, n is the number of atoms in the molecule, *3n-6* is the number of vibrational frequencies in the molecule (for a linear molecule it is *3n-5*), U_i is $\frac{h\upsilon}{k_B T}$ for the *i*th vibrational mode (h is Planck's constant, υ is vibrational frequency, k_B is Boltzman's constant), and U_i* is the analogous term for the molecule substituted with a heavier tellurium isotope. A

fractionation factor (α) between two substances can be calculated using reduced partition function ratios (β) as: $\alpha = \frac{\beta_1}{\beta_2}$.

By using the Bigeleisen and Mayer [1947] equation, we assume that fractionation of tellurium isotopes in different species including crystals and molecules is governed by small differences in the vibrational energies of substituted molecules (i.e. mass dependent fractionation). Clusters and molecules with heavier isotopes vibrate at lower frequencies and have a correspondingly lower zero-point energy compared to species substituted with lighter isotopes. Therefore, for each isotopic substitution reaction, vibrational (phonon) Helmoltz free energy can be used to estimate the driving energies such that isotopic fractionations can be estimated by knowing the isotope effects on vibrational frequencies. Unfortunately, vibrational frequencies for crystals and isotopically substituted Te-bearing species are not well known. In order to overcome these problems and limitations, first principles electronic structure calculations can be used to create vibrational models of species such as gas-phase molecules, solutes, and crystals.

Previous work has shown that observed equilibrium isotopic fractionations of other elements can be predicted with useful accuracy using the first-principles electronic structure and lattice dynamical modeling [e.g., Schauble et al., 2009; Meheut et al., 2007; Rustad et al., 2010]. These techniques are used for Te here.

In general, we adopted a cluster-based approach that is similar to Rustad et al. [2010]. In order to mimic the crystal-chemical environment of tellurium atoms in telluride minerals, we construct clusters consisting of a core group of atoms of a central tellurium surrounded by nearest neighbors, a 2nd-nearest neighbor coordination shell, and finally partially charged atoms added outside the 2nd shell to satisfy dangling bonds and

neutralize the net charge of the cluster. It is worth mentioning that in their model, Rustad et al. [2010] considered the 2nd and 3rd nearest neighbors explicitly, and so they generally worked with larger clusters than in the present study.

Core atoms are modeled with the greatest care, using medium-sized or larger basis sets to achieve reasonable accuracy. The atoms in the inner core are initially set at positions corresponding to measured X-ray crystal structures, and then allowed to relax to find their minimum-energy configuration. The force-constant (Hessian) matrix is then calculated for vibrational analysis of the relaxed structure. Atoms outside the core are treated in a more simplified way, and are fixed in position and not included in the vibrational analysis. This fixed shell is then surrounded on the outside by a mantle of pseudo-hydrogen atoms placed along each dangling bond at a distance of 1.5Å, with partial charges corresponding to the Pauling bond order of the dangling bond (Figure 1). Outer-shell and pseudo-atom electronic structures are approximated with a small basis set (LANL2DZ) [Dunning and Hay, 1977; Wadt and Hay, 1982a; b]; Rustad et al. [2010] used a similar-sized basis set (3-21G) in their preceding work on Ca and Mg in carbonate minerals. All molecular and supermolecular calculations used the Gaussian09 software package [Gaussian 09: AM64L-G09RevB.01 12-Aug-2010]. Clusters representing calaverite ($AuTe_2$; [Schutte et al., 1988]), hessite (Ag_2Te; [Schneider et al., 1993]), altaite (PbTe; [Noda et al., 1987]), CdTe [Zachariasen, 1926], and native tellurium (Te; [Bradley, 1924]) are modeled. These minerals are chosen to represent the most common and/or economically significant minerals and mineral types. Table 1 and Figure 1 present the designed structures for these clusters.

Table 1- Modeled supermolecular clusters representing different tellurides and native Te with details of their cores, 2nd layer shell, and outer layer.

Cluster	Core	2nd Shell	Outer layer (partially charged H)
Hessite (Ag_2Te)	Te bonded to 8 Ag	14 Te	88
Altaite (PbTe)	Te bonded to 6 Pb	18 Te	78
CdTe	Te bonded to 4 Cd	12 Te	36
Calaverite ($AuTe_2$)	Te bonded to 6 Au	25 Te	42
Native Te	Te bonded to 2 Te	20 Te	14

Along with the clusters, we modeled gas phase molecules and aqueous species, including TeF_6, H_6TeO_6, $H_5TeO_6^-$, H_2TeO_3, TeO_3^{2-}, H_2Te, and Te_2. They were chosen to span a range of oxidation states and include species potentially relevant to hydrothermal transport.

a)

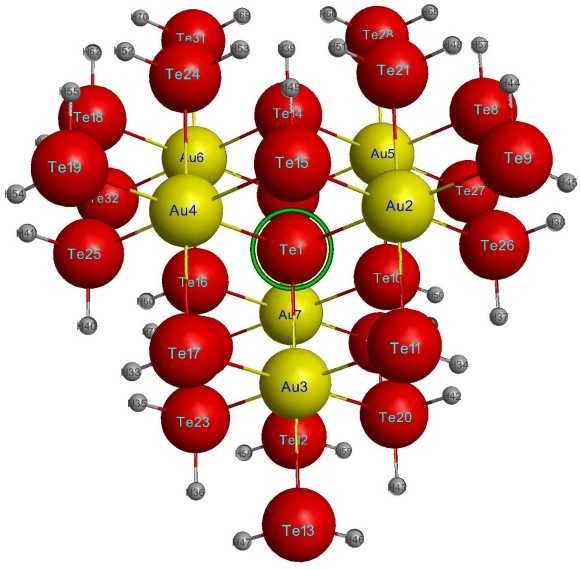

b)

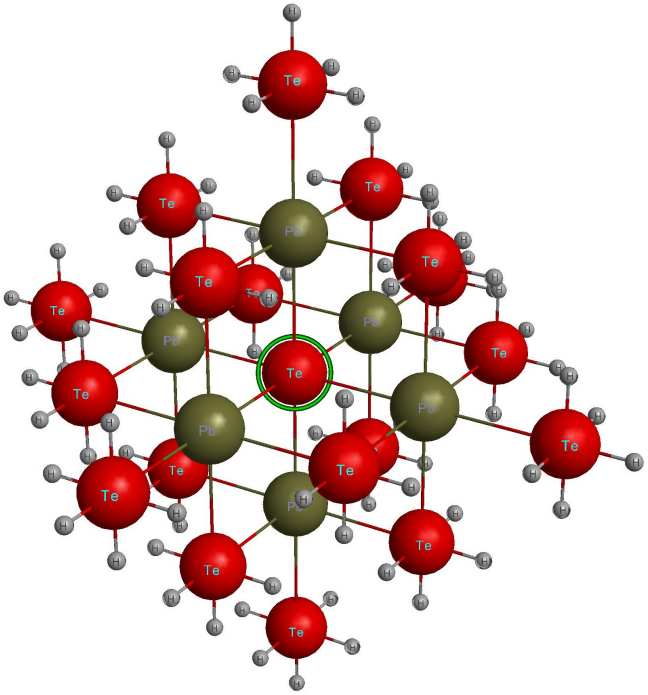

c)

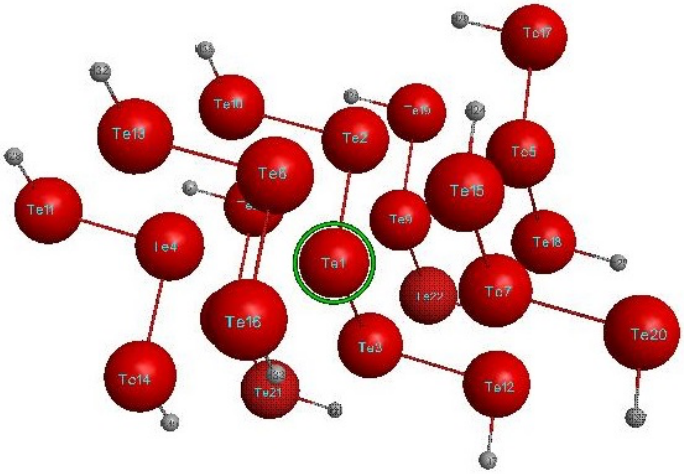
Te17
Te10
Te13
Te2
Te5
Te8
Te15
Te11
Te4
Te9
Te18
Te1
Te7
Te16
Te3
Te20
Te14
Te21
Te12

d) 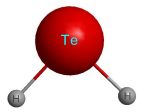

e) 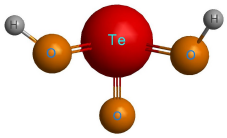

Figure 1- Clusters of (a) calaverite ($AuTe_2$), (b) altaite (PbTe), (c) native Te along with (d) H_2Te, and (e) H_2TeO_3 molecules

All models presented in detail here are constructed using hybrid density-functional theory (B3LYP; [Becke, 1993]) and the Def2-SVPD basis set [Rappoport and Furche, 2010], which seems to provide reasonably accurate results at moderate computational cost. This is indicated by good agreement with test calculations using larger (and presumably more accurate) basis sets such as Def2-TZVP [Weigend and Ahlrichs, 2005], cc-pVTZ [Dunning and Woon, 1993], and aug-cc-pVDZ [Dunning, 1989] and also with measured vibrational spectra of gas phase molecules.

Reduced partition function ratios for some crystalline species (native Te, cubic CdTe in a sphalerite-type structure, PbTe altaite, $AuAgTe_4$ sylvanite, $AuTe_2$ calaverite, and Ag_2Te hessite) are also estimated using density functional theory (DFT) with periodic boundary conditions. For calaverite we have assumed a 12-atom local unit cell structure derived from the 24-atom superstructure proposed by Krutzen and Inglesfield [1990], which approximates the estimated incommensurate modulation of the actual structure. The average calaverite unit cell structure and its high-pressure modifications were previously studied with similar modeling methods [e.g., Caracas and Gonze, 2004].

In general, our procedure for periodic boundary condition calculations is similar to previous work on ^{13}C-^{18}O clumping and $^{26}Mg/^{24}Mg$ fractionation [Schauble et al., 2006; 2011]. The present calculations use Vanderbilt-type ultrasoft pseudopotentials to describe inner-shell electrons and plane-wave basis sets to describe valence and near

valence electrons [Vanderbilt, 1990]. Pseudopotentials are taken from publicly available libraries, including the PSLibrary for tellurium [Te.pbe-dn-rrkjus_psl.1.0.0.UPF; Dal Corso, 2014] and the GBRV library for other elements [Garrity et al., 2014]. The PSLibrary pseudopotential for tellurium is chosen because it includes semi-core 4*d* electrons in the active valence, and seems to reproduce molecular structures and vibrational frequencies somewhat more accurately than the GBRV pseudopotential. We use the PBE gradient-corrected density functional of Perdew et al. [1996]. Model calculations are performed with the Quantum Espresso software package [Giannozzi et al., 2009; http://www.quantum-espresso.org], using the UCLA Geochemistry and Astrobiology computing cluster. The kinetic energy cutoff for plane wave basis sets is 82 Rydberg (1116 eV), a high value, to ensure reasonable convergence in electronic energies and phonon frequencies. Phonon frequencies are calculated at the center of the Brillouin zone and at other high-symmetry wave vectors for comparison with published infrared, Raman, and neutron-scattering spectra. Grids of non-zero phonon wave vectors are used to estimate the effect of Te-isotope substitution on the Helmholtz free energy for each crystal, and then to calculate reduced partition function ratios for isotope exchange crystal [Elcombe and Hulston, 1975]. Comparisons to published spectroscopy data for native Te [Powell and Martel, 1975], ZnTe [Vagelatos et al., 1974], cubic CdTe [Rowe et al., 1974], and PbTe-altaite [Cochran et al, 1966] suggest that the DFT models systematically underestimate phonon frequencies by approximately 6%, and a best-fit scale factor of 1.06 has been applied in all calculations of reduced partition function ratios with plane- wave basis sets. This scale factor is similar to ones used in previous

studies of oxide, carbonate, and silicate minerals using the PBE functional [e.g., Widanagamage et al., 2014; Schauble, 2011].

For PbTe altaite, we also estimated reduced partition function ratios using a published empirical lattice-dynamics model based on harmonic and coulomb potentials fit to measured phonon dispersion and elastic properties [Cochran et al., 1966; Model 3]. For cubic CdTe, we estimated reduced partition function ratios using an analytic Stillinger-Weber potential fit to previously published DFT phonon calculations using a local density functional [Han and Bester, 2017]. Calculating phonon frequencies with these potentials requires much less computational effort than the DFT models, so it is possible to sample a large number of phonon wave vectors. The results listed below for PbTe altaite and cubic CdTe are based on shifted 8x8x8 Monkhorst-Pack grids containing 120 distinct phonon wave vectors.

3. Results and Discussion

3.1. Basis sets effects on cluster models

We performed test calculations using six basis sets of varying size for core atoms in each cluster, including Def2-TZVP [Weigend and Ahlrichs, 2005; Metz et al., 2000; Peterson et al, 2003; Andrae et al., 1990], cc-pVTZ-PP [Peterson et al., 2003; Peterson and Puzzarini, 2005; Peterson, 2003], aug-cc-pVDZ-PP [Peterson et al., 2003; Peterson and Puzzarini, 2005; Peterson, 2003], Def2-SVPD [Rappoport and Furche, 2010; Metz et al., 2000; Peterson et al, 2003; Andrae et al., 1990], cc-pVDZ-PP [Peterson et al., 2003; Peterson and Puzzarini, 2005; Peterson, 2003], and LANL2DZ [Dunning and Hay, 1977; Wadt and Hay, 1982a; Wadt and Hay, 1982b]. In general, we found that fractionation factors estimated using medium-sized versus larger basis sets (i.e. all but LANL2DZ) for

the core structure agrees quite well with each other. Table 2 is a comparison of results using the B3LYP model chemistry and different basis sets at 100°C for several different clusters. Table 3 shows the same test for gas-phase species. In both cases, results based the Def2-SVPD basis sets [Rappoport and Furche, 2010; Metz et al., 2000; Peterson et al, 2003; Andrae et al., 1990], are in a good agreement with those produced by larger basis sets.

Table 2- Calculated reduced partition function ratios for cluster molecules using B3LYP chemistry model and different basis sets at 100°C.

	PbTe	**CdTe**	**Ag_2Te**	**$AuTe_2$**	**Te**
Def2-TZVP	1.00069	1.00128	1.00101	1.00149	1.00063
cc-pVTZ-PP	1.00073	1.00127	1.00103	1.00146	1.00065
aug-cc-pVDZ-PP	1.00073	1.00127	1.00102	1.00141	1.00066
Def2-SVPD	1.00072	1.00123	1.00104	1.00142	1.00070
cc-pVDZ-PP	1.00077	1.00130	1.00105	1.00146	1.00066
LANL2DZ	1.00075	1.00136	1.00109	1.00164	1.00059

Table 3- Calculated reduced partition function ratios for gas species using B3LYP chemistry model and different basis sets at 100°C.

	TeF_6	**H_6TeO_6**	**$H_5TeO_6^-$**	**H_2TeO_3**	**TeO_3^{2-}**	**H_2Te**	**Te_2**
Def2-TZVP	1.00956	1.00766	1.00715	1.00467	1.00465	1.00108	1.00075
cc-pVTZ	1.00969	1.00772	1.00718	1.00461	1.00468	1.00107	1.00075
aug-cc- pVDZ	1.00889	1.00722	1.00666	1.00430	1.00412	1.00107	1.00073
Def2-SVPD	1.00904	1.00720	1.00669	1.00423	1.00405	1.00104	1.00074
cc-pVDZ	1.00940	1.00765	1.00716	1.00437	1.00452	1.00107	1.00074
LANL2DZ	1.00813	1.00757	1.00711	1.00404	1.00392	1.00105	1.00058

For native tellurium the difference between the cc-pVTZ-PP and the Def2-SVPD model results is 0.03 ‰ at 100°C (Figure 2). Small basis sets like LANL2DZ do not agree as well, however. Tellurium clusters terminated by hydrogen atoms are within ~ 0.11 ‰ of partial-H terminated models (using Def2-SVPD); the results for both

positively and negatively partial-H terminated models are not significantly different from each other (Figure 2).

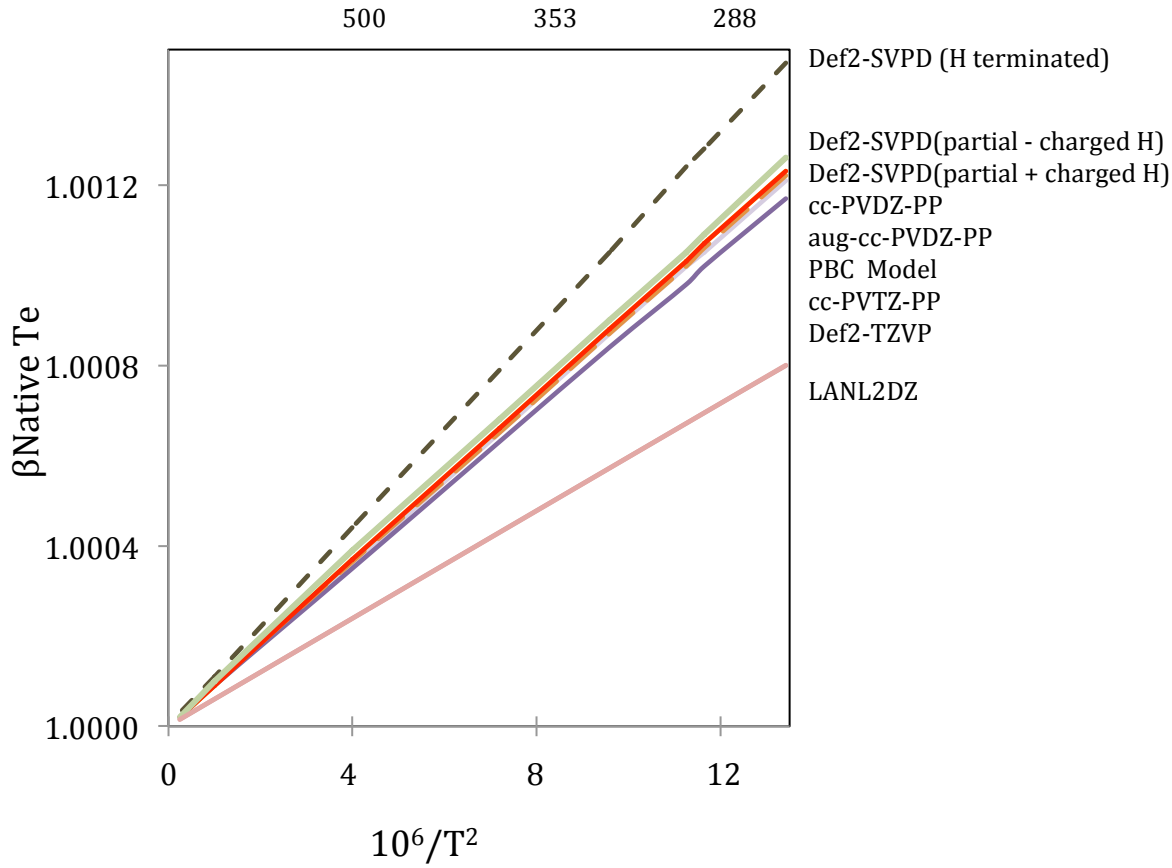

Figure 2- Calculated reduced partition function ratios comparing models of native-Te using different basis sets, with terminating hydrogen atoms or partial charges (B3LYP model and PBC model).

3.2 Effects of model chemistry

We also tested different model chemistries in addition to B3LYP, including RHF (Hartree-Fock [Hartree, 1928], and MP2 (second-order Møller-Plesset theory [Møller and Plesset, 1934]. A comparison of the test results at 100°C using the Def2-SVPD basis sets are shown in Table 4 and 5 for clusters and gas molecules, respectively. The choice of model chemistry, and particularly B3LYP vs. MP2, appears to have little effect on calculated fractionation factors.

Table 4- Calculated reduced partition function ratios for cluster molecules comparing different model chemistry, using Def2-SVPD basis set at 100°C.

	PbTe	**CdTe**	**Ag2Te**	**AuTe**	**Te**
RHF	1.00076	1.00145	1.00116	1.00170	1.00105
B3LYP	1.00072	1.00123	1.00104	1.00142	1.00070

Table 5- Calculated reduced partition function ratios for gas species comparing different model chemistry, using Def2-SVPD basis set at 100°C.

	TeF_6	**H_6TeO_6**	**$H_5TeO_6^-$**	**H_2TeO_3**	**TeO_3^{2-}**	**H_2Te**	**Te_2**
RHF	1.01150	1.00929	1.00879	1.00527	1.00539	1.00117	1.00096
B3LYP	1.00904	1.00720	1.00669	1.00423	1.00405	1.00107	1.00074
MP2	1.00947	1.00755	1.00708	1.00449	1.00426	1.00112	1.00062

3.3 Discussion

Our testing indicates that B3LYP [Becke, 1993] and the Def2-SVPD basis sets [Rappoport and Furche, 2010; Metz et al., 2000; Peterson et al, 2003; Andrae et al., 1990] are reasonably accurate, while also being computationally efficient. Calculated fractionations for gas-phase species (Table 6) using this combination are in good agreement with previously reported theoretical estimates [Smithers and Krouse, 1968]. At 100°C, TeO_3^{2-}, Te_2, and H_2Te are within ~1‰ of their results, and show the same order of ^{130}Te enrichment. For TeF_6, our estimation is ~1.6‰ lower than their value.

Table 6- Calculated reduced partition function ratios for gas-phase molecules. All models shown were calculated at the B3LYP/Def2-SVPD level.

Molecule	298K	373K	500K	1000K	Smithers & Krouse (373K)
TeF_6	1.01356	1.00904	1.00522	1.00134	1.01060
H_6TeO_6	1.01078	1.00716	1.00413	1.00108	
$H_5TeO_6^-$	1.01008	1.00669	1.00386	1.00100	
H_2TeO_3	1.00638	1.00428	1.00249	1.00065	
TeO_3^{2-}	1.00609	1.00405	1.00234	1.00061	1.00469
H_2Te	1.00140	1.00104	1.00068	1.00023	1.00098
Te_2	1.00115	1.00074	1.00041	1.00010	1.00079

Vibrational frequencies and molecular structures in gas-phase molecules TeF_6, H_2Te, TeO_3^{2-}, and Te_2 match reasonably well with measured values [Claassen et al., 1970; Siebert et al., 1955; Gomez and Jensen, 1997; Barrow and Parcq, 1972] (Table 7). In the case of TeF_6, there is an up to 10% offset from measured frequencies. For TeO_3^{2-} there is also a similar difference between modeled frequencies and measured values. For H_2Te, ~2% disagreement in determined frequencies compared to the harmonic frequency values is observed, and for Te_2 the disagreement is ~1%. Disagreements between experimental and ab initio theoretical frequencies have long been noted [Pople et al. 1993; Scott and Radom 1996; Schauble, 2004; Merrick et al., 2007; Alecu et al., 2010].

In order to correct the underestimation of model frequencies, we considered applying a frequency scaling factor. There have been numerous studies on using scale factors to improve agreement between computational and experimental frequencies [Pople et al. 1993; Scott and Radom 1996; Merrick et al., 2007; Alecu et al., 2010]. Alecu et al. [2010] determined general scale factors for vibrational harmonic and fundamental frequencies using a wide variety of different chemistry models and basis sets. Their recommended scale factors for B3LYP/Def2-TZVP are, respectively, 0.999 and 0.959 for harmonic and fundamental frequencies [Alecu et al., 2010]. However, the calibration set

of molecules in these types of studies typically do not include Te-bearing molecules, or include a very few of them. We evaluated the systematic error and scaling factors for specifically TeF_6, TeO_3^{2-}, and H_2Te (species with available experimental frequencies). Our best-fit scale factors for TeF_6, TeO_3^{2-}, and H_2Te are respectively 1.098, 1.124, and 1.013. We have calculated alternative β factors for these species using these scales factors. For the purpose of comparison, we also tried simply multiplying experimental frequencies assumed to correspond to the ^{130}Te isotopologue by the ratio of the modeled frequencies of the lighter isotopologue (with ^{125}Te) to the frequencies of the heavy one (^{130}Te). At 100°C, for TeF_6, results using the best-fit scale factor and isotopologue frequency ratios both predicts a larger β factor than unscaled frequencies do, by 1.5‰ and 1.4‰ respectively. The β factor also increases for TeO_3^{2-} by ~1.0‰ using either correction approach at 100°C. For H_2Te the adjustments are very small, +0.02‰ and +0.01‰. On the other hand, applying the recommended general harmonic frequency scale factor of 0.999 by Alecu et al. [2010] to TeF_6, TeO_3^{2-}, and H_2Te resulted in minimal changes of ~−0.2‰, 0‰, and 0‰ changes in our calculated β factors at 100°C. Thus, employing the recommended general scale factor had almost no effect on estimated β factors. Notably, Te-bearing molecules appear to behave differently than the general calibration set of molecules from previous scale factor studies.

The offsets between theoretical and measured vibrational frequencies in TeF_6, TeO_3^{2-}, and H_2Te are different from each other, and they also vary among the different vibrational modes of each molecule. Consequently, it is not clear that there is a consistent best-fit scale factor to resolve disagreements between theoretical and measured vibrational frequencies in these molecules and correct the errors. Therefore, in present

study we did not use any frequency scale factor for the calculations we report in the results for gas phase molecules and cluster models.

Table 8 compares calculated fractionations for tellurium crystals using B3LYP/Def2-SVPD and plane-wave density functional theory models with periodic boundary conditions (PBC). The cluster result for native Te is ~0.02‰ heavier than the PBC model at 100°C, The differences for altaite, cadmium telluride, hessite, and calaverite are respectively 0.2 to 0.3‰, ~0.3‰, ~0.4‰, and 0.6‰. In all cases the cluster model predicts higher $^{130}Te/^{125}Te$ fractionation value compare to PBC. The calculated $^{130}Te/^{125}Te$ fractionation between native Te and PbTe based on the cluster-model is smaller in comparison to the PBC model prediction (Figure 3).

Table 7- A comparison between vibrational frequencies of TeF_6, TeO_3^{2-}, H_2Te, and Te_2 B3LYP/Def2-SVPD level in present study with experimental values [Claassen et al., 1970; Siebert et al., 1955; Gomez and Jensen, 1997; Barrow and Parcq, 1972].

cm^{-1}	**Present Study**	**Experimental Values**
TeF_6		
T2U(3)	173.8	197
T2G(3)	271.9	314
T1U(3)	290.4	325
EG(2)	621.8	670.3
A1G(1)	624.6	697.1
T1U(3)	692.8	752
TeO_3^{2-}		
E(2)	239.3	326
A1(1)	283.5	354
E(2)	654.5	703
A1(1)	670.8	758
H_2Te		(Harmonic)
A1	893.9	877.9
A1	2113.4	2146.7
B2	2121.9	2154.4
Te_2		
ν	245.4	247.1

Table 8- Calculated reduced partition function ratios (β) for crystals at various temperatures. All cluster models shown here were calculated at the B3LYP/Def2-SVPD level.

Cluster Model	298K	373K	500K	1000K
CdTe	1.00192	1.00123	1.00069	1.00017
Ag_2Te-Hessite	1.00163	1.00104	1.00058	1.00015
PbTe-Altaite	1.00112	1.00072	1.00041	1.00010
$AuTe_2$-Calaverite	1.00221	1.00142	1.00079	1.00020
Native Te	1.00105	1.00068	1.00039	1.00010
Periodic Boundary Conditions (PBC) Model				
CdTe (DFT)	1.00152	1.00097	1.00054	1.00014
CdTe (Han & Bester)	1.00150	1.00096	1.00054	1.00013
Ag_2Te-Hessite	1.00118	1.00076	1.00042	1.00011
PbTe (DFT)	1.00079	1.00050	1.00028	1.00007
PbTe (Cochran et al.)	1.00064	1.00041	1.00023	1.00006
$AuTe_2$-Calaverite	1.00123	1.00079	1.00044	1.00011
$AuAgTe_4$-Sylvanite	1.00137	1.00088	1.00049	1.00012
Native Te (DFT)	1.00102	1.00066	1.00037	1.00009

In the supermolecular cluster model results, native tellurium is predicted to have lower $^{130}Te/^{125}Te$ than the coexisting CdTe, PbTe (altaite), $AuTe_2$ (calaverite), and Ag_2Te (hessite) at all relevant temperatures; however, plane wave calculations show the lowest $^{130}Te/^{125}Te$ for PbTe (altaite) (Figure 3). $^{130}Te/^{125}Te$ reduced partition function ratios estimated by supermolecular cluster-model has the highest value for $AuTe_2$, while it is the highest for CdTe determined by PBC model (Figure 4).

Consistent with previous studies [Smithers and Kraose 1968, Urey, 1947], $^{heavy}Te/^{light}Te$ is expected to be higher in oxidized tellurium species (Figures 5 - 7). For instance, amongst all calculated species, Te (VI) in TeF_6 displays the highest and Te (-II) and Te (0) in H_2Te and Te_2 the lowest β $^{130}Te/^{125}Te$.

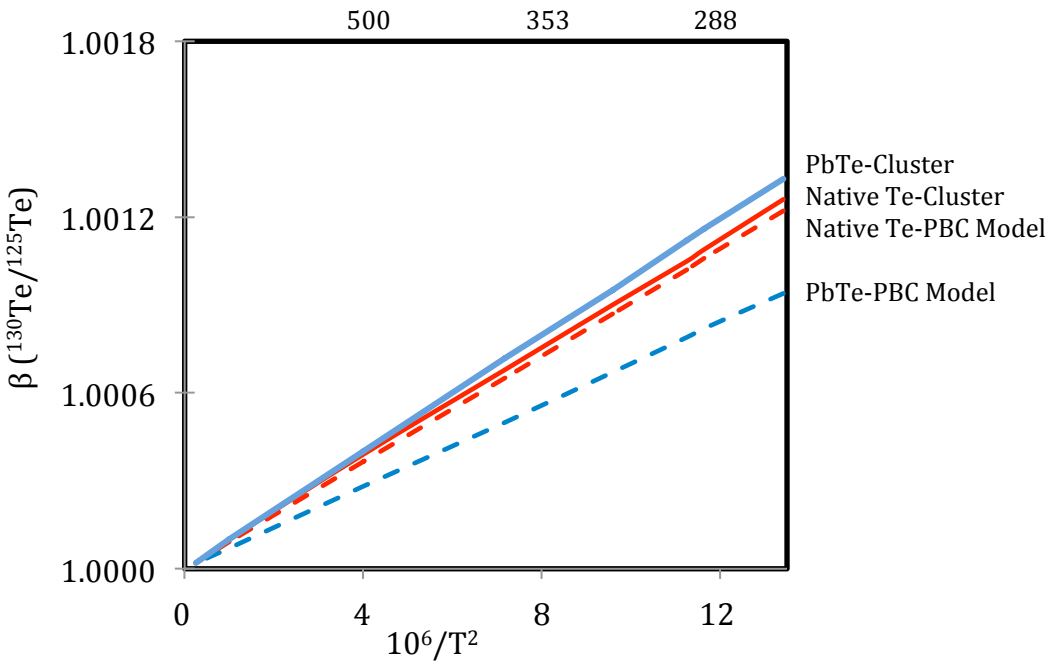

Figure 3- Calculated reduced partition function ratios for lead telluride and native tellurium, comparing supermolecular cluster (B3LYP/Def2-SVPD) and periodic boundary condition density functional theory models (using the PBE functional).

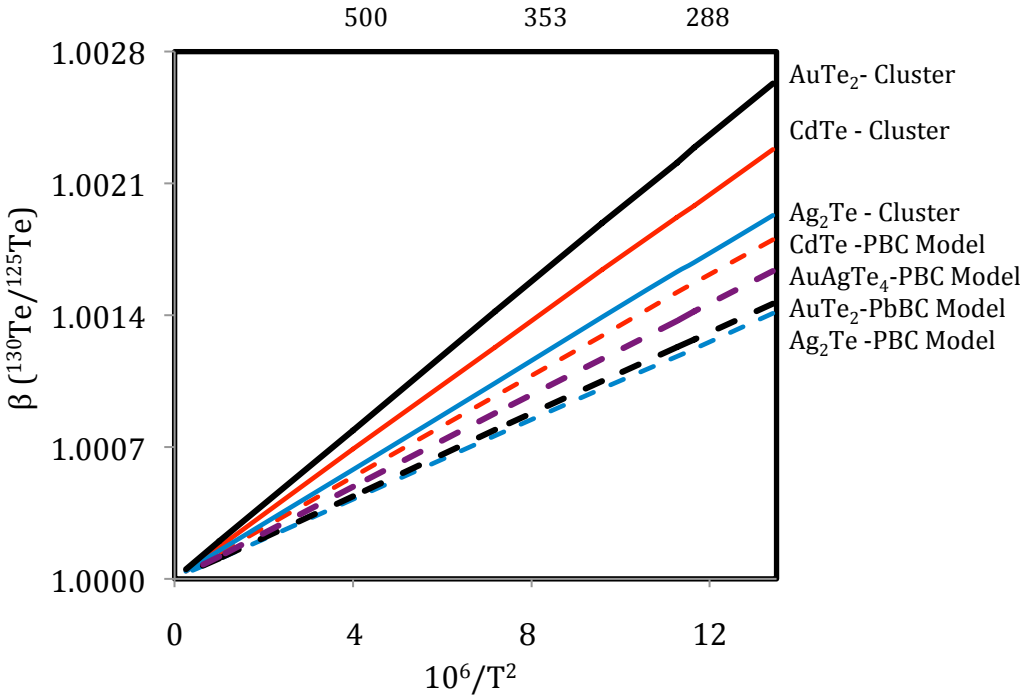

Figure 4- Calculated reduced partition function ratios for calaverite, hessite, and CdTe comparing supermolecular cluster (B3LYP/Def2-SVPD) and periodic boundary condition density functional theory models (using the PBE functional). Also, calculated value for sylvanite using periodic boundary condition density functional theory models (using the PBE functional).

Among Te (IV) species, tellurite (TeO_3^{2-}) is just 0.23 ‰ (at 100°C) lighter than Te (IV) in tellurous acid (H_2TeO_3). For Te (VI), $H_5TeO_6^-$ is 0.46 ‰ lighter than H_6TeO_6 at the same temperature (Figure 5).

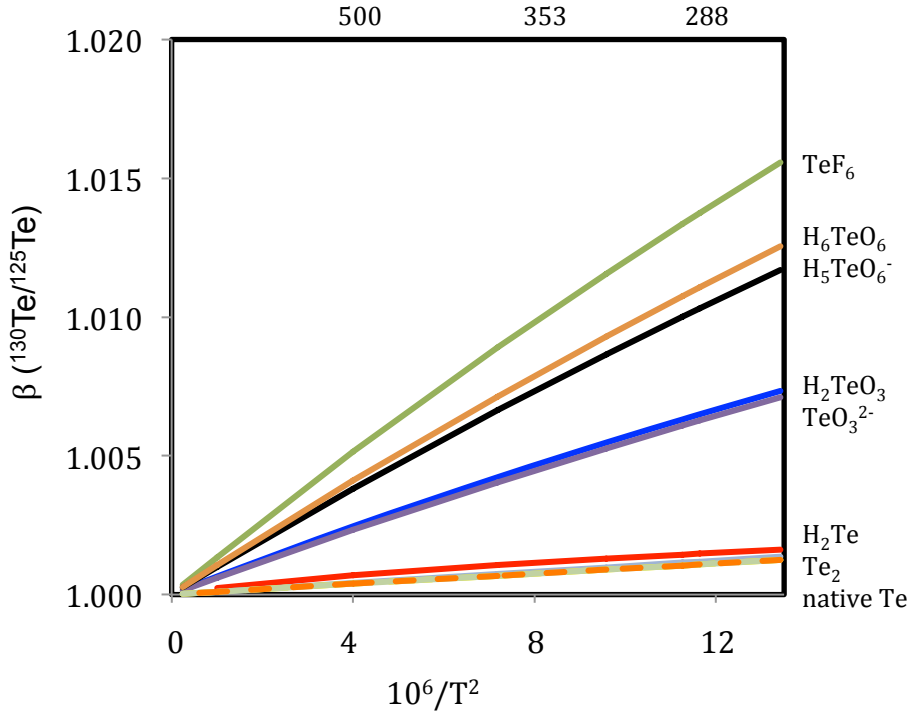

Figure 5- Calculated isotope fractionations for molecules, including gas-phase analogues of hydrothermal species. Crystalline native tellurium is shown for reference (B3LYP/ Def2-SVPD).

The PBC model for sylvanite ($AuAgTe_4$) predicts higher $^{130}Te/^{125}Te$ than in calaverite ($AuTe_2$) and hessite (Ag_2Te) (Figure 7). Estimated bond lengths using cluster model are in a better agreement with experimental values than PBC model (Figures 8, and 9).

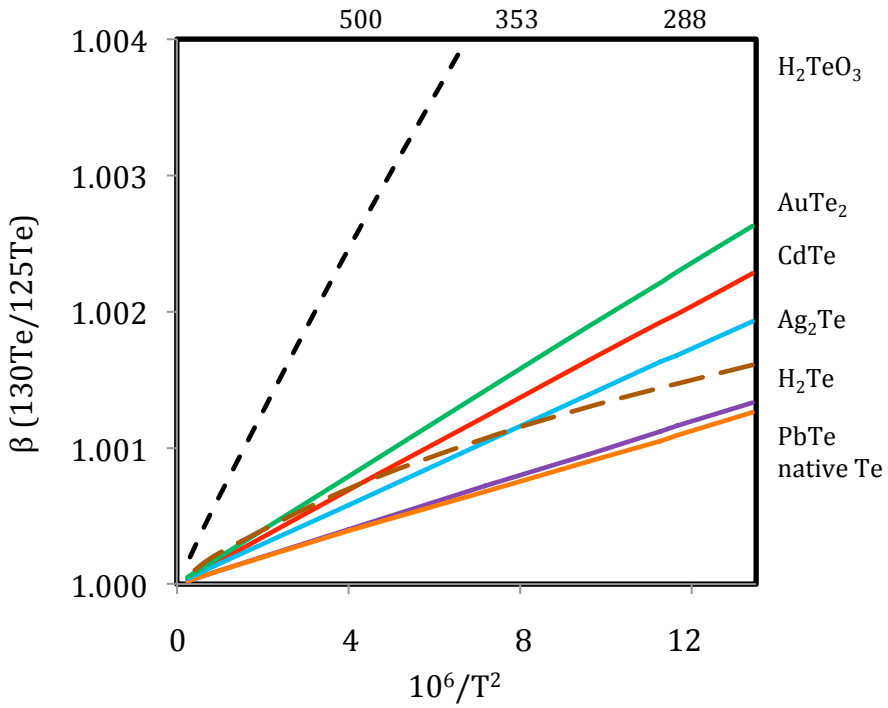

Figure 6- Calculated reduced partition function ratios for different crystals, as well as molecular H_2Te, and H_2TeO_3, using cluster models (B3LYP/Def2-SVPD).

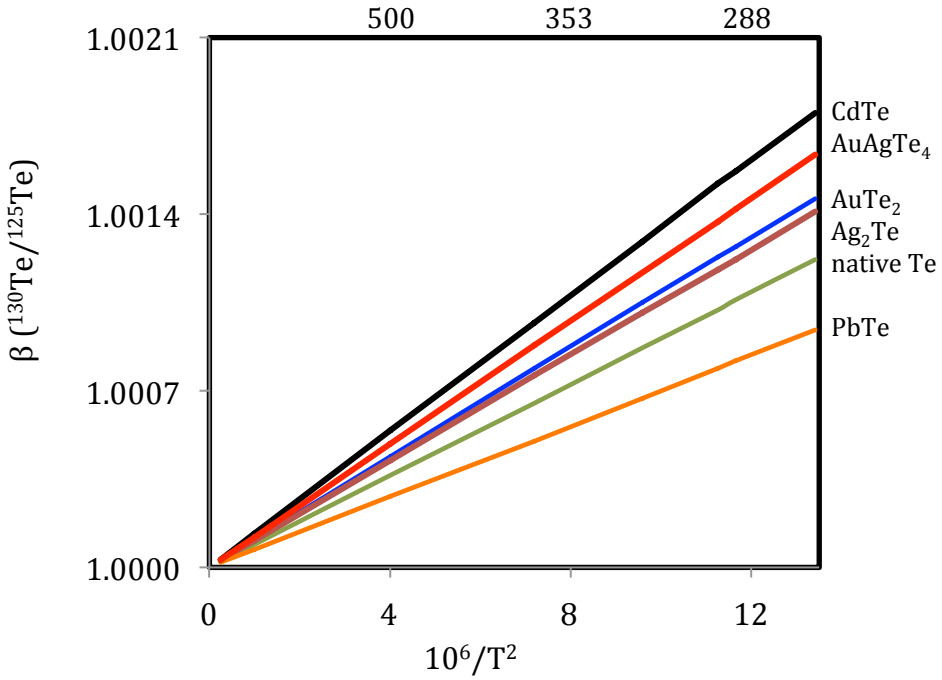

Figure 7- Calculated reduced partition function ratios for different crystals with periodic boundary condition density functional theory models (using the PBE functional).

Calculated fractionation factors decrease with increasing temperature in both gas–phase species, supermolecular clusters, and periodic-boundary condition models. $^{130}Te/^{125}Te$ fractionations are expected to be ~3-4 ‰ (at 100°C) between coexisting Te(IV) and Te (-II) compounds. Among gas-phase species, Te (VI) molecules TeF_6, H_6TeO_6, and $H_5TeO_6^-$ will have the highest $^{130}Te/^{125}Te$ at equilibrium, while Te_2 and H_2Te are lowest, with 6‰ to 8 ‰ predicted fractionation between Te (VI) and Te (-II) species at 100°C. Crystalline native tellurium and molecular Te_2 are identical within the likely uncertainty of the models. Amongst all the gas molecules with the oxidation states ranging from -II to +VI, Te_2 shows the lowest $^{130}Te/^{125}Te$. This suggests that structural properties of the molecules also play a role.

Calculated isotope fractionations using the cluster method in simple Te (-II) telluride crystals (CdTe, Ag_2Te, and PbTe) show a strong, roughly linear correlation with bond length in both models. In general $^{130}Te/^{125}Te$ is higher in tellurides with shorter bond lengths, which presumably corresponds to higher bond stiffness (Figures 8, and 9). This correlation between bond strength and calculated isotope fractionations can also be seen in the gas-phase molecules with the same oxidation state of tellurium.

The values of $^{130}Te/^{125}Te$ in Te (IV) species (TeO_3^{2-}) is predicted to be 3-4‰ higher than in reduced Te species such as calaverite ($AuTe_2$), hessite (Ag_2Te), CdTe, altaite (PbTe), and sylvanite ($AuAgTe_4$) at 100°C, suggesting that strong isotopic fractionation is a likely consequence if Te (IV) species play the role of transporter of tellurium to hydrothermal deposits. However, kinetic control of fractionation, or quantitative precipitation of aqueous tellurium species could potentially act to make observed fractionations smaller than would be predicted at equilibrium.

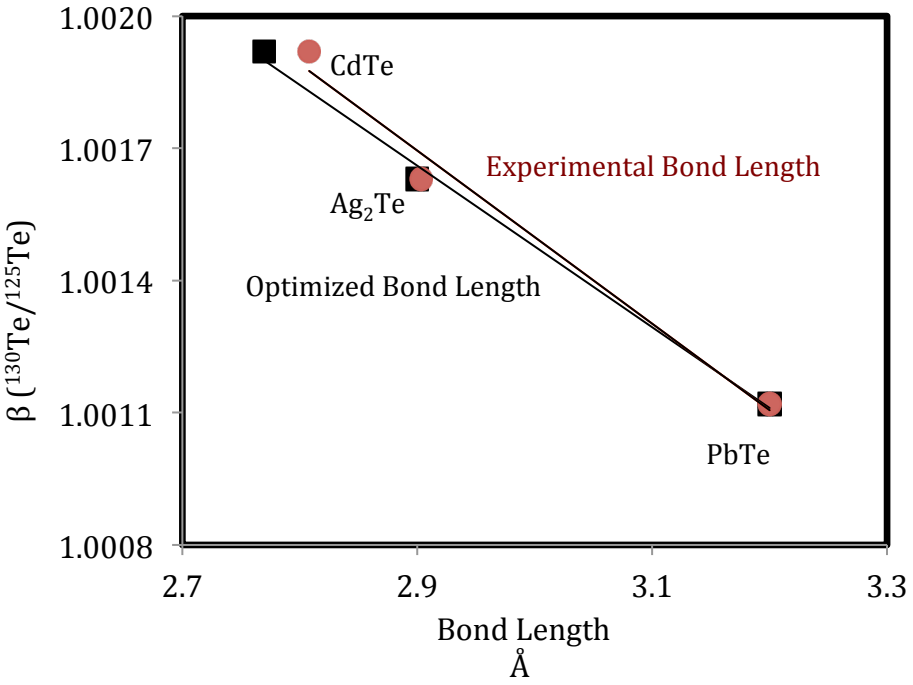

Figure 8- Calculated reduced partition function ratios using the cluster model (B3LYP/Def2-SVPD) vs. experimental (red circles [Nod et al., 1987; Wyckoff 1963; Schneider and Schulz, 1993]) and optimized bond lengths (black squares) for (-II) telluride crystals at 25°C.

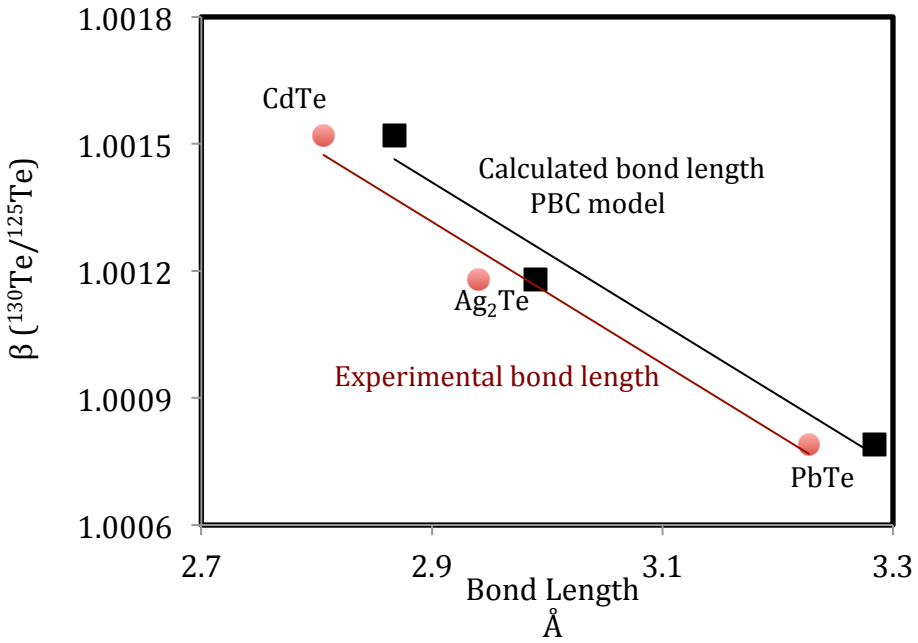

Figure 9- Calculated reduced partition function ratios using the PBC model vs. experimental (red circles [Nod et al., 1987; Wyckoff 1963; Schneider and Schulz, 1993]) and modeled bond lengths (black squares) for (-II) telluride crystals at 25°C.

Finally, we calculated α as: $\alpha = \frac{\beta}{\beta_{native\,Te}}$ for all the mineral species. For both super molecular cluster and PBC models α is the lowest for PbTe (Figures 10 and 11). The highest α for a telluride, using cluster models, is predicted for calaverite ($AuTe_2$) (Figure 10).

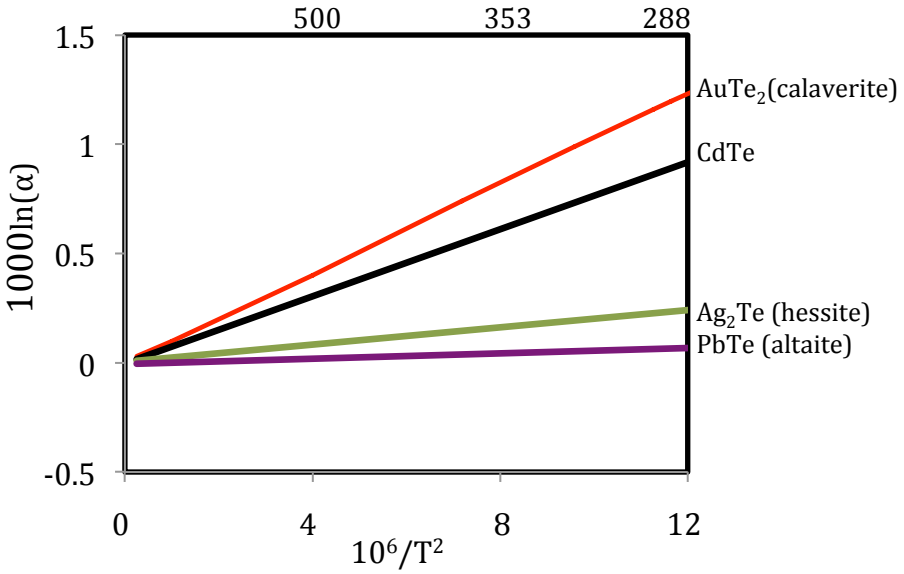

Figure 10- Calculated fractionation factors, relative to native tellurium, for crystals based on cluster models (B3LYP/Def2-SVPD).

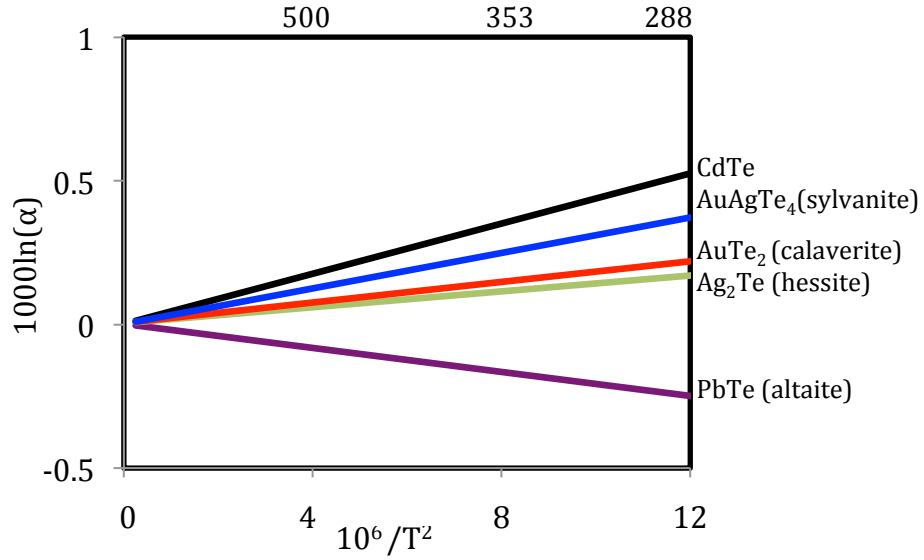

Figure 11- Calculated fractionation factors, relative to native tellurium, for crystals based on PBC models.

3.4 Comparison with measurements

Recently, analyses of naturally occurring calaverite and native Te samples in Cripple Creek, and also sylvanite along with native Te samples in Boulder County were reported based on multicollector-inductively coupled plasma-mass spectrometry (MC-ICP-MS) [Fornadel et al. 2014; 2017]. In the lack of internationally accepted standard for the measurement of Te isotopes, Fornadel et al. [2014, 2017] prepared their own standard as their reference [Fornadel et al. 2014]. Overall, measured $\delta^{130}Te/^{125}Te$ values for tellurides and native Te in the system Au-Agu-Te systems range from −1.54‰ to +0.44‰ and −0.74‰ to +0.16‰, respectively [Fornadel et al., 2014; 2017]. Values of $\delta^{130}Te/^{125}Te$ for Te (IV)-bearing tellurites (tellurite, paratellurite, emmonsite, and poughite) range from −1.58‰ to +0.59‰ [Fornadel et al., 2017] (Figure 12).

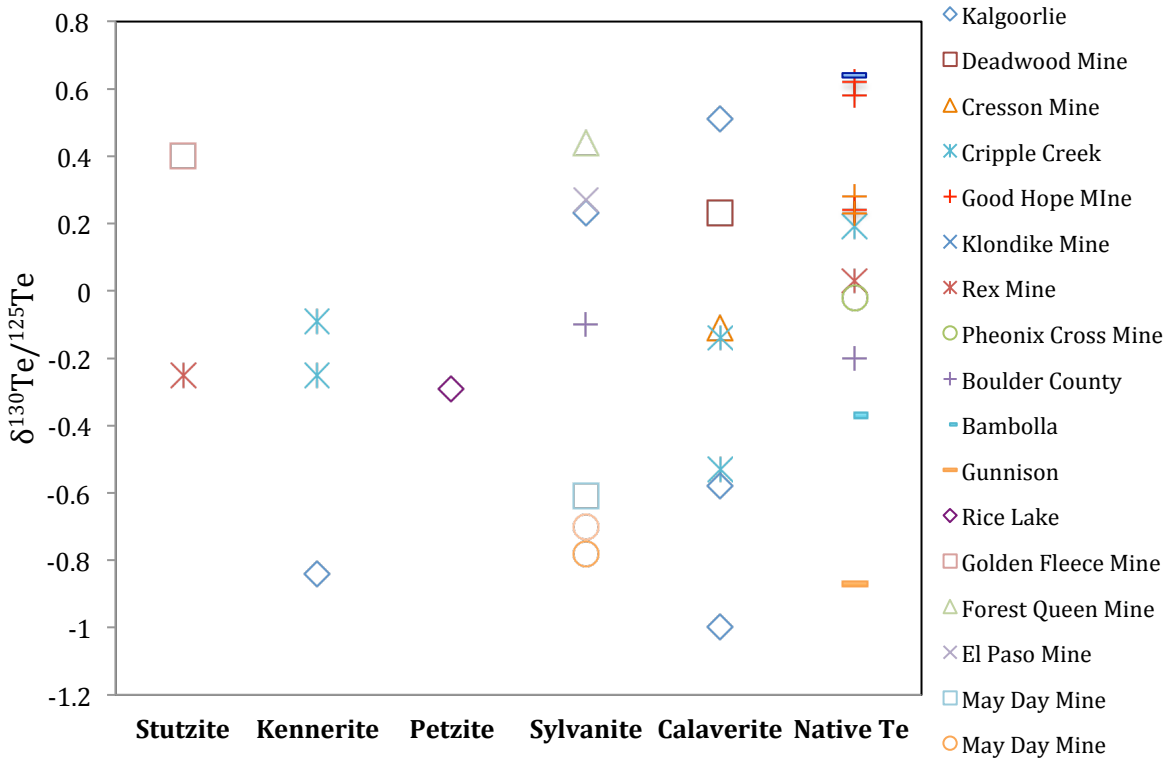

Figure 12- $\delta^{130}Te/^{125}Te$ values measured by MC-ICP-MS in tellurides and native Te range from -1.00 to 0.64 ‰ [Fornadel et al., 2014].

Although various samples of naturally occurring tellurides and native Te from multiple sites were analyzed, there are only a few instances where more than one mineral was analyzed from the same location, and even in these instances the paragenetic relationships between minerals is not clear. Therefore, the observed range in Te fractionations may have to do with locality-specific and/or temporal variations, at least in part.

The measurements of Fornadel et al. [2014] suggest a fractionation in the range of −0.72‰ to −0.33‰ for $^{130}Te/^{125}Te$ in calaverite compared to native Te (both collected from Cripple Creek), while our results using cluster models predict an enrichment of 0.4‰ in calaverite at equilibrium with native Te at ~227°C (the likely fluid temperature [Fornadel et al., 2017; Grundler et al., 2013]). Also, calculations based on the PBC method predict an enrichment of 0.07‰ in calaverite at the same temperature. For the case of sylvanite compared to native Te (both sampled from Boulder County), the experimental $^{130}Te/^{125}Te$ fractionation is +0.10 ‰, close to our prediction of +0.13 ‰ based on the PBC model at 227°C (Figure 13).

Cripple Creek is the only location where $\delta^{130}Te/^{125}Te$ was measured for both calaverite and native Te. Deposits in the Cripple Creek and Boulder County areas are epithermal systems related to relatively shallow emplacement of alkaline igneous rocks, and mineralized between 130° to 270°C [Fornadel et al., et al., 2017]. Conversely, orogenic deposits have different suites of tellurides, some of which may have formed at higher temperatures (above 400°C).

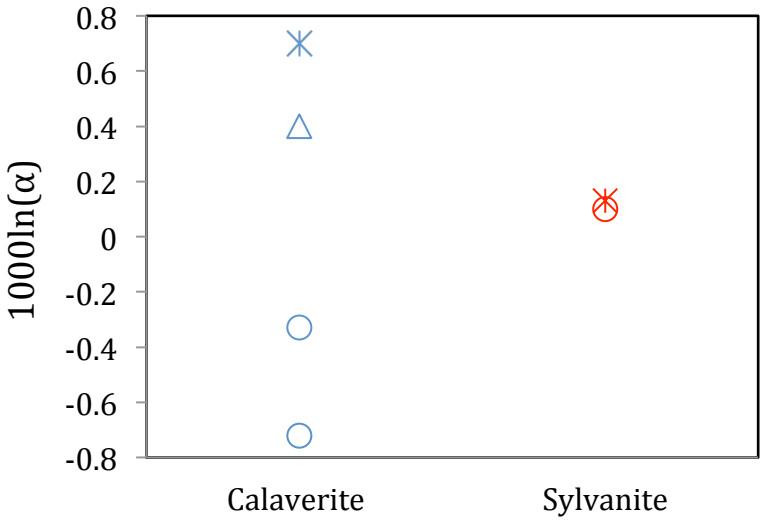

Figure 13- A comparison of observed differences in isotopic composition for calaverite and sylvanite compared to native Te in Cripple Creek and Boulder County (circle) with fractionations estimated with cluster models (triangle), and PBC models (star) at 227°C.

Additionally, isotopic compositions of tellurite and native Te collected from Bambolla were measured, suggesting a tellurite-Te fractionation in the range of −0.84‰ to −0.46‰ for $^{130}Te/^{125}Te$ [Fornadel et al., 2017], while our cluster models predict an enrichment of ~2‰ in tellurite at equilibrium at 227°C.

Measured fractionation values suggest at most a minor effect of reduction-oxidation reactions on isotopic fractionation between Te (0) and Te (-I) or Te (-II). Our calculations however, predict a more profound fractionation for the redox reactions that might happen during Te-transportation and ore-formation if Te (IV) species are important in hydrothermal solutions. Overall, the observed experimental isotopic fractionation of Te is similar to previous studies on magmatic Se [Layton-Matthews et al., 2013], which could suggest a magmatic source of Te for these samples. Fornadel et al. [2017] concluded that phase separation and temperature are unlikely to be the primary control on Te-isotope fractionation. They suggested other factors including the compositions of the

source rocks and the duration of the mineralization process could play a more important role. More measurements, especially co-genetic Te pairs representing various oxidation states, along with controlled laboratory experiments are needed.

Conclusions

Our calculated fractionations for gas-phase species based on hybrid density functional theory (B3LYP) are in good agreement with previously reported estimates [Smithers and Krouse, 1968]. Isotope fractionations calculated with hybrid density functional theory (B3LYP) for gas-phase species and clusters mimicking crystals appear not to depend greatly on the details of basis set choice. Over a range of temperatures, native Te is predicted to have lower $^{130}Te/^{125}Te$ than the coexisting CdTe, hessite, altaite, and calaverite. Calaverite is predicted to have the highest $^{130}Te/^{125}Te$ among the telluride crystals studied with this model. Plane-wave density functional theory models with periodic boundary conditions predict that $^{130}Te/^{125}Te$ is lower for PbTe (altaite) than other crystals. It is predicted to be 0.3-0.5 ‰ lower than in the gold/silver tellurides including hessite, calaverite, and sylvanite at 100°C. Calculated isotope fractionations using the cluster model for native Te are in a good agreement with plane-wave density functional theory models with periodic boundary conditions, and for CdTe show a reasonable agreement. However, for hessite and calaverite the agreement is poor. There is a strong relationship between crystal structure, bond strength and isotopic properties. For instance, calculated isotope fractionation for different telluride crystals using either type of model show a roughly linear correlation with bond length and bond strength.

In addition to oxidation states, structural properties of the molecules including symmetry and polarity also play a role in isotopic fractionation of the gas species. In general, $^{130}Te/^{125}Te$ is higher for more oxidized species, and lower for reduced species. Te (IV) species such as TeO_3^{2-} will have $^{130}Te/^{125}Te$ that is ~3 ‰ greater than Te (-I) in calaverite ($AuTe_2$) and ~3.5 ‰ greater than hessite (Te (-II)) at 100°C. This is consistent with a general expected enrichment in heavier isotopes in oxidized aqueous tellurium species, relative to tellurides in the system Au-Ag-Te. If Te (IV) species are important in hydrothermal tellurium transport, the reduction reaction to form Te (-I) and Te (-II) species should cause a distinct isotopic signature. If reduced species such as Te_2 and H_2Te play the role of Te-transporter then isotope fractionations may be less pronounced. Studies of the isotope fractionation of Te could shed light on the geochemistry and formation process of tellurides in the system Au-Ag-Te, in Te-bearing ore deposits. However, in order to develop a better understanding of tellurium and its roles in the system Au-Ag-Te systematic measurements of carefully located samples with known paragenetic relationships are needed.

References

Alecu, I. M., Zheng, J., Zhao, Y., & Truhlar, D. G., 2010. Computational thermochemistry: Scale factor databases and scale factors for v1 I. M. Alecu, J. Zheng, Y. Zhao and D. G. Truhlar, J. Chem. Theory Comput., 2010, 6, 2872–2887.ibrational frequencies obtained from electronic model chemistries. *Journal of Chemical Theory and Computation*, *6*(9), 2872–2887.

Andrae, D.; Häußermann, U.; Dolg, M.; Stoll, H.; Preuß, H. T., 1990. Energy-adjusted*ab initio* pseudopotentials for the second and third row transition elements. *Theor. Chim. Acta*, *77*(2), 123–141.

Barrow, R.F., & Parcq, R.P., 1972. Rotational analysis of the $A0^{+}_{U}$, BO^{+}_{U} — XO^{+}_{g} systems of gaseous Te_2. *Proc. R. Soc. Lond.*, *287*(A.327), 279–287

Bigeleisen, J., Mayer, M.G., 1947. Calculations of Equilibrium Constants for Isotopic Exchange Reactions. *J. Chem. Phys.* 261, 261–267.

Bradley, A.J., 1924. L . The crystal structures of the rhombohedral forms of selenium and tellurium. *Phylosophical Mag.* 48, 477–496.

Cao, X., Dolg, M., & Stoll, H., 2003. Valence basis sets for relativistic energy-consistent small-core actinide pseudopotentials. *Journal of Chemical Physics*, *118*(2), 487–496.

Caracas, R., and Gonze, X., 2004. Structural, electronic, and dynamical properties of calaverite $AuTe_2$ under pressure. *Phys. Rev. B* 69:144114.

Chasteen, T.G., Fuentes, D.E., Tantaleán, J.C., Vásquez, C.C., 2009. Tellurite: history, oxidative stress, and molecular mechanisms of resistance. *FEMS Microbiol. Rev.* 33, 820–832.

Chivers, T., & Laitinen, R. S., 2015. Tellurium: A maverick among the chalcogens. *Chemical Society Reviews*, *44*(7), 1725–1739.

Ciobanu, C.L., Cook, N.J., Spry, P.G., 2006. Preface - Special issue: Telluride and selenide minerals in gold deposits - How and why? *Mineral. Petrol.* 87, 163–169.

Claassen, H. H., Goodman, G. L., Holloway, J. H., & Selig, H., 1970. Raman Spectra of MoF_6 , TcF_6 , ReF_6 , UF_6 , SF_6 , SeF_6 , and TeF_6 in the Vapor State. *The Journal of Chemical Physics*, *53*(1), 341–348.

Cochran, W., Cowley, R.A., Dolling, G., Elcombe, M.M.,1966. The crystal dynamics of lead telluride. Proceedings of the Royal Society of London. Series A, *Math. and Phys. Sci.293:433-451.*

Cohen, B. L., 1984. Anomalous behavior of tellurium abundances. *Geochimica et*

Cosmochimica Acta, *48*(1), 203–205.

Cooke, D.R., McPhail, D.C., 2001. Epithermal Au-Ag-Te Mineralization, Acupan, Baguio District,Philippines: Numerical Simulations of Mineral Deposition. *Econ. Geol*. 96, 109–131.

Cook N. J., Ciobanu C. L., Spry P. G., Voudouris P., 2009. Understanding gold-(silver)-telluride-(selenide) mineral deposits. *Episodes* 32, no. 4: 249-263

Dal Corso A, 2014. Pseudopotentials periodic table: From H to Pu. *Comput. Mat. Sci.*. 95:337-350

Dunning, T. H., 1989. Gaussian basis sets for use in correlated molecular calculations. I. The atoms boron through neon and hydrogen. *The Journal of Chemical Physics*, *90*(2), 1007–1023.

Dunning Jr, T. H., Hay, P. J., Schaefer III, H. F., 1997. Methods of Electronic Structure Theory, *Plenum Press*, 2.

Elcombe, M. M., & Hulston, J. R., 1975. Calculation on sulphur isotope fractionation between sphalerite and galena using lattice dynamics. *Earth and Planetary Science Letters*, *28*(2), 172–180.

Fehr, M. A., Rehkämper, M., Halliday, A. N., Wiechert, U., Hattendorf, B., Günther, D., Rumble, D., 2005. Tellurium isotopic composition of the early solar system - A search for effects resulting from stellar nucleosynthesis,126Sn decay, and mass-independent fractionation. *Geochimica et Cosmochimica Acta*, *69*(21), 5099–5112.

Fehr, M.A., Hammond, S.J., Parkinson, I.J., 2018. Tellurium stable isotope fractionation in chondritic meteorites and some terrestrial samples. *Geochim. Cosmochim. Acta* 222, 17–33.

Fehr, M.A., Rehkämper, M., Halliday, A.N., 2004. Application of MC-ICPMS to the precise determination of tellurium isotope compositions in chondrites , iron meteorites and sulfides. *Inter. J. of Mass Spectrom.* 232, 83–94.

Fornadel, A.P., Spry, P.G., Haghnegahdar, M.A., Schauble, E.A., Jackson, S.E., Mills, S.J.,2017. Stable Te isotope fractionation in tellurium-bearing minerals from precious metal hydrothermal ore deposits. *Cosmochim. Acta* 202, 215–230.

Fornadel, A.P., Spry, P.G., Jackson, S.E., Mathur, R.D., Chapman, J.B., Girard, I., 2014. Methods for the determination of stable Te isotopes of minerals in the system Au–Ag–Te by MC-ICP-MS. *J. Anal. At. Spectrom.* 29, 623.

Fry, B., Ruf, W., Gest, H., & Hayes, J. M.,1988. Sulfur isotope effects associated with oxidation of sulfide by O_2 in aqueous solution. *Chemical Geology (Isotope*

Geoscience Section), *73*, 205–210.

Gandhi, S. M., & Sarkar, B. C., 2016. Mineral Deposits. *Essentials of Mineral Exploration and Evaluation*, *32*(4), 23–52.

Garrity KF, Bennett JW, Rabe KM and Vanderbilt D, 2014. Pseudopotentials for high-throughput DFT calculations. *Comput. Mat. Sci.* 81:446-452.

Gaussian 09: EM64L-G09RevD.01, Frisch, M. J.; Trucks, G. W.; Schlegel, H. B.; Scuseria, G. E.; Robb, M. A.; Cheeseman, J. R.; Scalmani, G.; Barone, V.; Mennucci, B.; Petersson, G. A.;Nakatsuji, H.; Caricato, M.; Li, X.; Hratchian, H. P.; Izmaylov, A. F.; Bloino, J.; Zheng, G.; Sonnenberg, J. L.; Hada, M.; Ehara, M.; Toyota, K.; Fukuda, R.; Hasegawa, J.; Ishida, M.; Nakajima, T.; Honda, Y.; Kitao, O.; Nakai, H.; Vreven, T.; Montgomery, J. A., Jr.; Peralta, J. E.; Ogliaro, F.; Bearpark, M.; Heyd, J. J.; Brothers, E.; Kudin, K. N.; Staroverov, V. N.; Kobayashi, R.; Normand, J.; Raghavachari, K.; Rendell, A.; Burant, J. C.; Iyengar, S. S.; Tomasi, J.; Cossi, M.; Rega, N.; Millam, M. J.; Klene, M.; Knox, J. E.; Cross, J. B.; Bakken, V.; Adamo, C.;Jaramillo, J.; Gomperts, R.; Stratmann, R. E.; Yazyev, O.; Austin, A. J.; Cammi, R.; Pomelli, C.; Ochterski, . J.; Dapprich, S.; Daniels, A. D.; Farkas, Ö.; Foresman, J. B.; Ortiz, J. V.;Cioslowski, J.; *Fox, D. J. Gaussian, Inc*., Wallingford CT, 2013.

Giannozzi, P., Baroni, S., Bonini, N., Calandra, M., Car, R., Cavazzoni, C., Ceresoli, D., Chiarotti, G.L., Cococcioni, m., Dabo, I., Corso, A.D., Fabris, S., Fratesi, G., de Gironcoli, S., Gebauer, R., Gerstmann, U., Gougoussis, C., Kokalj, A., Lazzeri, M., Martin-Samos, L., Marzari, N., Mauri, F., Mazzarello, R., Paolini, S., Pasquarello, A., Paulatto, L., Sbraccia, C., Scandolo, S., Sclauzero, G., Seitsonen, A.P., Smogunov, A., Umari, P., Wentzcovitch, R.M., 2009. Quantum ESPRESSO: a modular and opensource software project for quantum simulations of materials.

Grundler, P. V., Brugger, J., Etschmann, B.E., Helm, L., Liu, W., Spry, P.G., Tian, Y., Testemale, D., Pring, A., 2013. Speciation of aqueous tellurium(IV) in hydrothermal solutions and vapors, and the role of oxidized tellurium species in Te transport and gold deposition. *Geochim. Cosmochim. Acta* 120, 298–325.

Gumez, P.C., Jensen, P., 1997. A Potential Energy Surface for the Electronic Ground State of H2Te Derived from Experiment. *J. Mol. Spectros.* 185, 282–289.

Han, P., Bester, G., 2017. Force field potentials for the vibrational properties of II-VI semiconductor nanostructures. *Phys. Rev.* B 96:195436.

Hartree, D. R., 1928. The Wave Mechanics of an Atom with a non-Coulomb Central Field.Part I. Theory and Methods. *Mathematical Proceedings of the Cambridge Philosophical Society*, *24*(3), 426.

Hay, P. J., & Wadt, W. R., 1985a. Ab initio effective core potentials for molecular

calculations. Potentials for K to Au including the outermost core orbitale. *The Journal of Chemical Physics*, *82*(1), 299–310.

Hay, P. J., & Wadt, W. R., 1985b. Ab initio effective core potentials for molecular calculations. Potentials for the transition metal atoms Sc to Hg. *The Journal of Chemical Physics*, *82*(1), 270–283.

Hein, J.R., Koschinsky, A., Halliday, A.N., 2003. Global occurrence of tellurium-rich ferromanganese crusts and a model for the enrichment of tellurium. *Geochim. Cosmochim. Acta* 67, 1117–1127.

Johnson, T.M., 2004. A review of mass-dependent fractionation of selenium isotopes and implications for other heavy stable isotopes. *Chem. Geol.* 204, 201–214.

Kaupp, M., Schleyer, P. v. R., Stoll, H., & Preuss, H., 1991. Pseudopotential approaches to Ca, Sr, and Ba hydrides. Why are some alkaline earth MX_2 compounds bent? *The Journal of Chemical Physics*, *94*(2), 1360–1366.

Krutzen, B.C.H., Inglesfield, J.E., 1990. First-principles electronic structure calculations for incommensurately modulated calaverite. *J. Phys.: Condens. Matter* 2:4829-4847.

Krutzen, B. C. H., & Inglesfield, J. E., 1990. First-principles electronic structure calculations for incommensurately modulated calaverite. *Journal of Physics: Condensed Matter*, *2*(22), 4829–4847.

Li, X., Liu, Y., 2011. Equilibrium Se isotope fractionation parameters: A first-principles study. *Earth Planet. Sci. Lett.* 304, 113–120.

Lueth, V. W., 2016. Tellurium minerals of New Mexico. *American Mineralogist*, *38*(1), 17–23.

Martin, J. M. L., & Sundermann, A. , 2001. Correlation consistent valence basis sets for use with the Stuttgart-Dresden-Bonn relativistic effective core potentials: the atoms Ga-Kr and In-Xe. *Journal of Chemical Physics*, *114*(8), 3408–3420.

Méheut, M., Lazzeri, M., Balan, E., Mauri, F., 2007. Equilibrium isotopic fractionation in the kaolinite, quartz, water system: Prediction from first-principles density-functional theory. *Geochim. Cosmochim. Acta* 71, 3170–3181.

Merrick, J. P., Moran, D., & Radom, L., 2007. An evaluation of harmonic vibrational frequency scale factors. *Journal of Physical Chemistry A*, *111*(45), 11683–11700.

Metz, B., Stoll, H., & Dolg, M., 2000. Small-core multiconfiguration-Dirac-Hartree-Fock-adjusted pseudopotentials for post-d main group elements: Application to PbH and PbO. *Journal of Chemical Physics*, *113*(7), 2563–2569.

Møller, C., & Plesset, M. S., 1934. Note on an approximation treatment for many-electron systems. *Physical Review*, *46*(7), 618–622.

Moynier, F., Fujii, T., Albarede, F., 2009. Nuclear field shift effect as a possible cause of Te isotopic anomalies in the early solar system—An alternative explanation of Fehr et al. (2006 and 2009). *Meteoritics & Planetary Science*, *44*(Nr 11), 1735–1742.

Nicklass, A., Dolg, M., Stoll, H., & Preuss, H. ,1995. Ab initio energy-adjusted pseudopotentials for the noble gases Ne through Xe: Calculation of atomic dipole and quadrupole polarizabilities. *The Journal of Chemical Physics*, *102*(22), 8942 8952.

Nikolaev, Y.N., Prokof'ev, V.Y., Apletalin, A. V., Vlasov, E.A., Baksheev, I.A., Kal'ko, I.A., Komarova, Y.S., 2013. Gold-telluride mineralization of the Western Chukchi Peninsula, Russia: Mineralogy, geochemistry, and formation conditions. *Geol. Ore Depos.* 55, 96–124.

Noda, Y., Masumoto, K., Ohba, S., Saito, Y., Toriumi, K., Iwata, Y., Shibuya, I., 1987. Temperature dependence of atomic thermal parameters of lead chalcogenides, PbS, PbSe and PbTe. Acta Crystallogr. Sect. C Cryst. Struct. Commun. 43, 1443–1445.

Perdew, J.P., Burke, K., Ernzerhof, M.,1996. Generalized gradient approximation made simple. *Phys. Rev. Lett.* 77:3865– 3868.

Peterson, K. A., Figgen, D., Soll, H., Dolg, M., 2003. Systematically convergent basis sets with relativistic pseudopotentials. II. Small-core pseudopotentials and correlation consistent basis sets for the post-d group 16–18 elements. *Journal of Chemical Physics*, *119*(21), 11113–11123.

Peterson, K. A., 2003. Systematically convergent basis sets with relativistic pseudopotentials. I. Correlation consistent basis sets for the post-d group 13-15 elements. *Journal of Chemical Physics*, *119*(21), 11099–11112.

Peterson, K. A., and Puzzarini, C., 2005. Systematically convergent basis sets for transition metals. II. Pseudopotential-based correlation consistent basis sets for the group 11 (Cu, Ag, Au) and 12 (Zn, Cd, Hg) elements. *Theoretical Chemistry Accounts*, *114*(4–5), 283–296.

Pople, J. A., Scott, A. P., Wong, M. W., & Radom, L.,1993. Scaling Factors for Obtaining Fundamental Vibrational Frequencies and Zero-Point Energies from HF/6–31G* and MP2/6–31G* Harmonic Frequencies. *Israel Journal of Chemistry*, *33*(3), 345–350.

Powell, B.M., Martel, P., 1975. The lattice dynamics of tellurium. *J. Phys. Chem. Solids* 36:1287-1298.

Rappoport, D., & Furche, F., 2010a. Property-optimized Gaussian basis sets for molecular response calculations. *Journal of Chemical Physics*, *133*(13), 0–11.

Rappoport, D., & Furche, F., 2010b. Property-optimized Gaussian basis sets for molecular response calculations. *Journal of Chemical Physics*, *133*(13), 1–11.

Rowe, J.M., Nicklow, R.M., Price, D.L., Zanio, K., 1974. Lattice dynamics of cadmium telluride. *Phys. Rev.* B 10:671-675.

Rustad, J.R., Casey, W.H., Yin, Q.Z., Bylaska, E.J., Felmy, A.R., Bogatko, S.A., Jackson, V.E., Dixon, D.A., 2010. Isotopic fractionation of Mg^{2+}(aq), Ca^{2+}(aq), and Fe^{2+}(aq) with carbonate minerals. *Geochim. Cosmochim. Acta* 74, 6301–6323.

Schauble, E. A., 2004. Fractionation Theory to New Systems. *Reviews in Mineralogy & Geochemistry*, *55*, 65–111.

Schauble, E.A., 2011. First-principles estimates of equilibrium magnesium isotope fractionation in silicate, oxide, carbonate and hexaaquamagnesium$^{(2+)}$ crystals. *Geochim. Cosmochim. Acta* 75:844–869.

Schauble, E.A., Ghosh, P., Eiler, J.M., 2006. Preferential formation of ^{13}C-^{18}O bonds in carbonate minerals, estimated using first-principles lattice dynamics. *Geochim. Cosmochim. Acta* 70:2510–2529.

Schneider, J., and Schulz, H., 1993. X-ray powder diffraction of Ag_2Te at temperatures up to 1123 K. *Zeitschrift fur Kristallographie* 203:1-15.

Scott, A. P., & Radom, L., 1996. Harmonic vibrational frequencies: An evaluation of Hartree-Fock, Møller-Plesset, quadratic configuration interaction, density functional theory, and semiempirical scale factors. *Journal of Physical Chemistry*, *100*(41), 16502–16513.

Send, R., & Furche, F., 2010. First-order nonadiabatic couplings from time-dependent hybrid density functional response theory: Consistent formalism, implementation, and performance. *Journal of Chemical Physics*, *132*(4).

Shackleton, J.M., Spry, P.G., Bateman, R., 2003. Telluride mineralogy of the Golden Mile deposit, Kalgoorlie, Western Australia. *Can. Mineral.* 41, 1503–1524.

Smithers, R.M., Krouse, H.R., 1968. Tellurium isotope fractionation study. *Can. J. Chem.* 46, 583–591.

Urey H. C., 1947. The thermodynamic properties of isotopic substances. *J. Chem. Soc. (London),* 562-581

Vagelatos, N., Wehe, D., King, J.S., 1974. Phonon dispersion and phonon densities of

states for ZnS and ZnTe. *J. Chem. Phys.* 60:3613-3618.

Vanderbilt F., 1990. Soft self-consistent pseudopotentials in a generalized eigenvalue formalism. *Phys. Rev.* B 41:7892-7895.

Wadt, W. R., & Hay, P. J., 1985. Ab initio effective core potentials for molecular calculations. Potentials for main group elements Na to Bi. *The J. of Chem. Phys*, *82*(1), 284–298.

Weigend, F., & Ahlrichs, R., 2005. Balanced Basis Sets of Split Valence, Triple Zeta Valence and Quadruple Zeta Valence Quality for {H} to {R}n: {D}esign and Assessment of Accuracy. *Phys. Chem. Chem. Phys.*, *7*(18), 3297–3305.

Widanagamage, I.H., Schauble, E.A., Scher, H.D.,Griffith, E.M., 2014. Stable strontium isotope fractionation in synthetic barite. *Geochimica et Cosmochimica Acta* 147:58-75

Woon, D. E., & Dunning, T. H. ,1993. Gaussian basis sets for use in correlated molecular calculations. III. The atoms aluminum through argon. *The J.l of Chem. Phys*, *98*(2), 1358–1371.

Wyckoff, R.W.G., 1963. Crystal Structures, v.1, Second edition. Interscience Publishers, New York, New York.

Zachariasen W., 1926. Crystal structures of the tellurides of Be, Zn, Cd, and Hg Z. *Phys. Chem(Leipzig)* 119:210.

Chapter 3. A Model for $^{12}CH_2D_2$ and $^{13}CH_3D$ as Complementary Tracers for the Budget of Atmospheric CH_4

Abstract

We present a theoretical model to investigate the potential of $^{13}CH_3D$ and $^{12}CH_2D_2$, the doubly substituted mass-18 isotopologues of methane, as tools for tracking atmospheric methane sources and sinks. We use electronic structure methods to estimate kinetic isotope fractionations associated with the major sink reactions of methane in air (reactions with OH and Cl radicals), and combine literature data with reconnaissance measurements of the relative abundances of $^{13}CH_3D$ and $^{12}CH_2D_2$ to estimate the compositions of the largest atmospheric sources. This model atmospheric budget is investigated with a simplified box model in which we explore both steady state and dynamical (non-steady state) conditions triggered by changes in emission or sink fluxes. The steady-state model predicts that sink reactions will generate a marked (>100‰) clumped isotope excess in atmospheric $\Delta^{12}CH_2D_2$ relative to the net source composition. $^{12}CH_2D_2$ measurements may thus be useful for tracing both atmospheric source and sink fluxes. The effect of sinks on $\Delta^{13}CH_3D$ is much less pronounced, indicating that $^{13}CH_3D$ in air will give a more focused picture of the source composition.

1. Introduction

In this study we develop a theoretical model using the relative abundances of $^{13}CH_3D$ and $^{12}CH_2D_2$, the doubly substituted mass-18 isotopologues of methane, to quantitatively track the sources and the sinks of atmospheric methane. The ultimate goal is to develop new tracers for atmospheric methane.

Atmospheric methane is the second most important long-lived greenhouse gas in Earth's atmosphere; it contributes 0.5 Wm^{-2} to total radiative forcing [*Dlugokencky et al.,* 2011; *IPCC Report,* 2013]. Moreover, as the result of reactions with radicals in the atmosphere it plays an important role in producing tropospheric ozone and stratospheric water vapor. This indirectly adds around 0.2 Wm^{-2} to its forcing [*Dlugokencky et al.,* 2011; *IPCC Report,* 2013]. Natural sources of methane include wetlands, oceans, termites, and the breakdown of clathrates, whereas major anthropogenic sources include fossil fuel exploitation, ruminant livestock, rice agriculture, waste management, and biomass burning. Biogenic and thermogenic generation of methane are both significant [*Wuebbles and Hayhoe,* 2002].

The methane concentration in the atmosphere increased through much of the twentieth century, reaching 1.7ppmv in 1990 [*Breas et al.,* 2001], then leveled off from 1999 until 2007 [*Rigby et al.,* 2008]. The rise has now resumed. Since 2007, the global average growth of methane concentration has been ~6 ppb/year [*Kirschke et al.,* 2013]. However, the mechanism and origin of this new upward trend are not fully understood [*Rigby et al.,* 2008; *Dlugokencky et al.,* 2011; *Montzka et al.,* 2011; *Bousquet et al.,* 2011; *Kirschke et al.,* 2013]. Possibilities include enhanced wetland CH_4 emission, anthropogenic CH_4 emissions, wild fires, less intense OH photochemistry, and inter-annual wind changes. More generally, there is a lack of understanding regarding the

factors that have driven the rise in methane concentrations during the past few decades [*IPCC Report,* 2013], highlighting uncertainties in the methane atmospheric budget [*Bousquet et al.,* 2011; *Dlugokencky et al.,* 2011; *Kirschke et al.,* 2013; *IPCC Report,* 2013]. Inverse (top-down) models of the methane budget are not consistent with process-based (bottom-up) models and inventories. Identifying the role of sinks as well as sources should improve our overall understanding of the atmospheric methane budget.

Isotopic measurements have been a valuable tool for distinguishing among various sources of CH_4 to the atmosphere [*Cicerone and Oremland,* 1988; *Dlugokencky et al.,* 2011]. $\delta^{13}C$ and (less commonly) δD measurements of atmospheric methane have been reported in numerous studies [*King et al.,* 1989; *Fung et al.,* 1991; *Levin et al.,* 1993; *Hein and Crutzen,* 1997; *Lowe et al.,* 1999; *Quay et al.,* 1999; *Bréas et al.,* 2001; *Saueressig et al.,* 1995, 2001; *Fletcher et al.,* 2004; *Whiticar and Schaefer,* 2007]. Different methane sources have different $^{13}C/^{12}C$ and D/H ratios, depending on the methane formation process and the carbon and hydrogen isotope compositions of precursor materials [*Cicerone and Oremland,* 1988]. In general, methane produced at high temperatures, including methane released from biomass burning or natural gas, is enriched in both ^{13}C and D [*Cicerone and Oremland,* 1988] relative to low temperature methane sources (Figure 1). However, $^{13}C/^{12}C$ and D/H do not always uniquely resolve methane originating from microbial, thermogenic, and abiotic sources. [*Sherwood Lollar et al.,* 2006; *Ono et al.,* 2014; *Stolper et al.,* 2014a]. Precise analyses of doubly substituted methane isotopologues (clumped isotopes) may offer additional constraints on methane sources [*Ma et al.,* 2008; *Stolper et al.,* 2014a; *Wang et al.,* 2015; *Young et al.,* 2016; *Young et al.*, 2017].

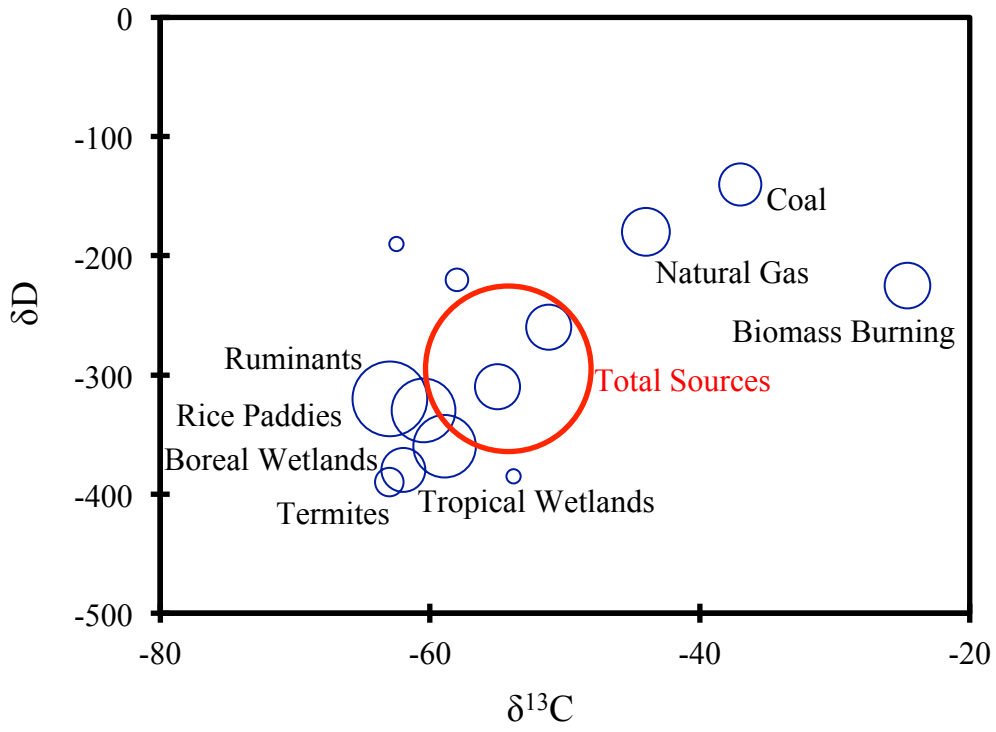

Figure 1- Estimated fluxes, δD and $\delta^{13}C$ for methane sources to the atmosphere (data from: Whiticar & Schaefer, 2007)

Atmospheric sink reactions are slower for D-substituted methane isotopologues [*Alei et al.,* 1987; *Cicerone and Oremland,* 1988; *Mroz et al.,* 1989], resulting in higher D/H in air compared to most sources. Methane containing multiple deuterium atoms (e.g., $^{12}CD_4$) has been analyzed in the atmosphere and found in much higher concentrations than would be expected from likely sources, suggesting a strong signature of sink reaction kinetics [*Mroz et al.,* 1989; *Kaye and Jackman,* 1990]. More recently, precise measurements of $^{13}CH_3D$ have been tested as potential tools for determining the generation temperature and mechanism for different sources of methane [*Stolper et al.,* 2014a, 2014b; *Wang et al.,* 2015]. *Douglas et al.* [2016] used Δ_{18} methane (departures in the relative abundances of both mass-18 isotopologues from the stochastic distribution) as a tool to determine the source of natural methane emissions from Arctic and Subarctic.

Tsuji et al. [2012] performed spectroscopic isotope measurements on $^{13}CH_3D$ to determine the isotope ratios of $^{13}CH_3D/^{12}CH_3D$ and $^{13}CH_3D/^{12}CH_4$ in natural methane. *Young et al.,* [2017] obtained both $^{13}CH_3D/^{12}CH_4$ and $^{12}CH_2D_2/^{12}CH_4$ signatures of abiotic and biotic methane formation in natural settings and in the laboratory. Theoretical studies of the equilibrium distribution of $^{13}CH_3D$ [*Cao and Liu,* 2012; *Webb and Miller,* 2014] and $^{12}CH_2D_2$ [*Stolper et al.,* 2015; *Young et al.,* 2016; *Young et al.,* 2017; *Piasecki et al.,* 2016] have also appeared. The $^{13}CH_3D/^{12}CH_4$ kinetic isotope effect in the sink reaction with Cl and OH radicals were determined for the first time by *Joelsson et al.* [2014, 2016] using Fourier transform infrared (FTIR) spectroscopy. Kinetic isotope effects for $^{12}CH_2D_2$ in reactions with OH and Cl radicals have also been measured [*Gierczak et al.,* 1997; *Sauer et al.*, 2015; *Feilberg et al.,* 2005; *Boone et al.*, 2001; *Matsumi et al.*, 1997; *Wallington and Hurley*, 1992].

In the present study, we investigate the potential for using two doubly substituted methane isotopologues, $^{13}CH_3D$ and $^{12}CH_2D_2$, as tracers of atmospheric methane cycling. There are no existing models, to our knowledge, that consider $^{13}CH_3D$ and $^{12}CH_2D_2$ in concert as distinct species for atmospheric studies. In the present work, we use electronic structure methods to estimate kinetic and equilibrium isotope signatures for methane sink reactions, including both mass-18 doubly substituted isotopologues of methane. We use our results to model the relative abundances of singly and doubly substituted methane species in the atmosphere in different relevant scenarios in order to assess the utility of the multiply-substituted species as tracers.

2. Methods

2.1 First-principles Calculations of Isotope Partitioning

We use first-principles electronic structure calculations to estimate kinetic and equilibrium isotope effects. All electronic structure calculations are made with the Gaussian 09 software package (EM64L-G09RevD.01; [*Frisch et al.,* 2013]). The main results reported in this study are based on 2nd-order Møller-Plesset theory (MP2; [*Møller and Plesset,* 1934]) and the medium-sized Gaussian basis sets cc-pVTZ [*Dunning,* 1989].

We also tried 6-311G** [*Krishnan et al.,* 1980] basis sets to test for consistency. These model chemistries do well at reproducing previous measurements and high-precision theoretical calculations of structural and vibrational properties of methane. No frequency scale factor or correction for anharmonicity has been used for our calculations and comparisons. Table 1 presents the comparison between our calculated harmonic frequencies of methane (cm^{-1}) and those of previous studies [*Gray et al.,* 1979; *Lee et al.,* 1995; *Liu and Liu,* 2016]. Harmonic frequencies for all isotopologues are in supplementary information (Table S1). Kinetic Isotope Effects ($KIE = \frac{k_{CH4}}{k_i}$) for sink reactions with OH and Cl radicals are modeled using transition state theory, with a one-dimensional Wigner tunneling correction for hydrogen and deuterium [*Gupta et al.,* 1997]. Test calculations indicate that tunneling of H-atoms is significant for absolute rate constants and KIEs in both sink reactions (Table S2 in supplementary information). In both reactions, corrected KIEs for $^{12}CH_3D$ and $^{12}CH_2D_2$ are about 0.1 larger than non-corrected values. We use Harmonic vibrational frequencies in transition state calculations. Saddle-point and reactant geometries are fully (energy) optimized at each

level of theory. *Lasaga and Gibbs* [1991], *Gupta et al.* [1997], *Troung and Truhlar* [1990], *Tanaka et al.* [1996], and *Roberto-Neto and Coitin.* [1998] used similar approaches to estimate KIEs of the reaction of singly-substituted CH_4 isotopologues with •OH and Cl•, yielding results similar to those of the present study. The optimized geometries for both reactions are given in Table 2. Figure 2 shows the transition state of methane in reaction with •OH and Cl•. Harmonic frequencies for both transition states are in Table S3 (supplementary information).

Table 1- Comparison of harmonic frequencies (cm^{-1}) for $^{12}CH_4$ between the present study and previous works [a]

Table 1. Comparison of Harmonic Frequencies (cm^{-1}) for $^{12}CH_4$ Between the Present Study and Previous Works[a]

	Present Work	*Liu and Liu* [2016]	*Lee et al.* [1995]	*Gray et al.* [1979]	*Bottinga* [1969]	*Jones and McDowell* [1959] (Recalculated)
Mode	MP2/cc-pVTZ	CCSD/aug-cc-pVTZ	CCSD(T)/cc-pVQZ	Expt./FF	Expt./FF	Expt./FF
A_1	3076	3045	3036	3026	3143	3143
E	1586	1584	1570	1583	1573	1573
F_2 stretch	3212	3162	3157	3157	3154	3154
F_2 bend	1350	1363	1345	1367	1357	1358
RMS error versus G&R 1979	38	10	14	–	59	59
Mean error versus G&R 1979	23	5	−6	–	24	24
$10^3 \ln[K_{eq}(^{13}CH_3D)]$	5.78	5.73	5.71[b]	5.73[b]	5.82[c]	5.69[b]
(8/3) $10^3 \ln[K_{eq}(^{12}CH_2D_2)]$	19.49	–	19.06[c], 19.20[b]	20.49[c], 19.72[b]	20.42[c]	19.67[b]

[a] (*G&R*, 1979 refers to *Gray et al.* [1979])
[b] K_{eq} determined using frequencies recalculated with tabulated force field.
[c] K_{eq} calculated from tabulated vibrational frequencies (correcting for an apparent data entry error in the original *Gray et al.* [1979], tabulation)

Table 2- The optimized geometries of transition state structures of methane reactions with OH and Cl radicals. Bonds directly participating in the reaction are indicated by dotted lines.

OH

C——H 1.832 Å C------H 1.889 Å O------H 1.317 Å O——H 0.9677 Å

Cl

C——H 1.080 Å C------H 1. 359 Å Cl------H 1.451 Å

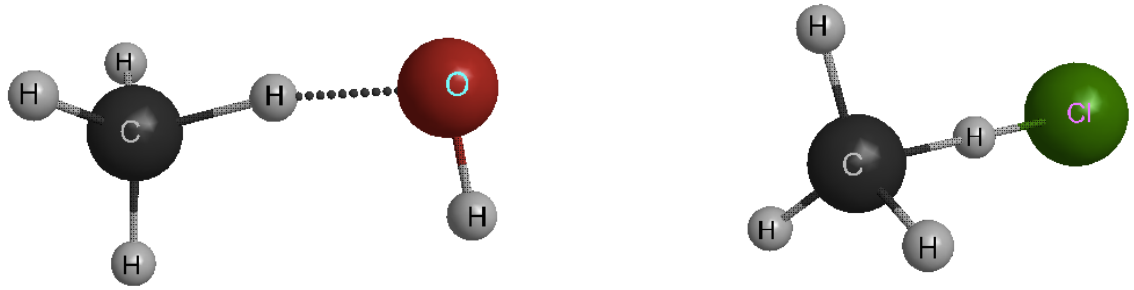

a) b)

Figure 2- Transition state structures for (a) CH_4---•OH, and (b) CH_4---Cl• sink reactions determined by electronic structure calculations at the MP2/cc-pVTZ level.

Equilibrium abundances of isotopologues are calculated using harmonic vibrational frequencies, based on the following exchange reactions and associated equilibrium constants:

$$^{13}CH_4 + {}^{12}CH_3D \rightleftharpoons {}^{12}CH_4 + {}^{13}CH_3D \quad (1)$$

$$K_{eq} = \frac{[{}^{13}CH_3D][{}^{12}CH_4]}{[{}^{13}CH_4][{}^{12}CH_3D]} \quad (2)$$

and

$$2\ {}^{12}CH_3D \rightleftharpoons {}^{12}CH_4 + {}^{12}CH_2D_2 \quad (3)$$

$$K_{eq} = \frac{[{}^{12}CH_2D_2][{}^{12}CH_4]}{[{}^{12}CH_3D]^2} \quad (4)$$

These equilibrium constants are sensitive to temperature, with $K_{eq}(^{13}CH_3D) \approx 1.007$ and $K_{eq}(^{12}CH_2D_2) \approx 1.02 \times (3/8)$ at ambient conditions ~300K, where $K_{eq}(^{12}CH_2D_2) = 3/8$ represents the stochastic distribution of isotopologues.

Isotopic distributions for clumped isotope species are expressed in delta notation:

$$\delta^i = \left(\frac{{}^iR_{sample}}{{}^iR_{standard}} - 1\right)(1000‰) \quad (5)$$

$$\Delta_j = \left(\frac{{}^jR_{sample}}{{}^jR_{stochastic}} - 1\right)(1000‰) \quad (6)$$

where *R* represents abundance ratios $^{13}CH_3D/^{12}CH_4$ or $^{12}CH_2D_2/^{12}CH_4$ for a sample, standard, or stochastic equivalent. D/H and $^{13}C/^{12}C$ ratios for the stochastic reference for each gas are calculated solely from the abundance ratios $^{12}CH_3D/^{12}CH_4$ and $^{13}CH_4/^{12}CH_4$, i.e. $D/H=1/4(^{12}CH_3D/^{12}CH_4)$ and $^{13}C/^{12}C=^{13}CH_4/^{12}CH_4$. This treatment neglects the effects of non-stochastic isotopologue partitioning on the abundances of singly-substituted species; however, numerical tests show no significant loss in accuracy in using this approach to determine bulk isotope ratios for gases, within the likely natural range of isotopologue distributions.

2.2 Atmospheric Methane Budget

We construct a model for steady-state $^{13}CH_3D$ and $^{12}CH_2D_2$ abundances in the atmosphere by considering the isotope and isotopologue compositions of major methane sources and isotope fractionations associated with the major sink reactions; the reactions of methane with OH and Cl radicals are the main sinks for atmospheric methane and are assumed to be the only fractionating sinks in our model. The model considers $\Delta^{13}CH_3D$ and $\Delta^{12}CH_2D_2$ of atmospheric methane in a homogenous "troposphere" reservoir, controlled by a balance between the emission flux of different sources to the atmosphere and the rates of CH_4 destruction by reaction with •OH and Cl• reactions. We also designed a box model to investigate non-steady state scenarios by inducing imbalances and changes in emissions and sinks.

2.2.1. Atmospheric sources and isotopologue abundances

There are significant uncertainties in the estimated fluxes of individual methane sources as well as the overall global budget. Here we use a "bottom-up" budget proposed by *Whiticar and Schaefer* [2007]. In this model, the total methane flux into the

atmosphere is 540 Tg/yr. The leading methane emission sources are biogenic, including wetlands, rice paddies, ruminants, landfills, Aerobic Methane Production (AMP), termites, oceans, and fresh water (Table 3). Wetlands, with a flux of 115 Tg/yr, are the most important source category. Abiogenic methane sources include natural gas, biomass burning, coal, gas hydrates, and geological. Among these sources, biomass burning and coal have the highest fluxes with 41 Tg/yr and 35 Tg/yr respectively (Table 3) [*Whiticar and Schaefer,* 2007]. In this group, AMP is perhaps the most controversial component -- it is not included in some other recent source budgets and estimates of the size of this source vary widely [*Kirschke et al.,* 2013; *Saunois et al.,* 2016]. However, AMP makes up a minor part of the total assumed biogenic methane source, and we assume that it has isotope signatures similar to microbial methane sources. The inclusion of AMP in our model budget does not substantially affect our overall conclusions. Aside from AMP, wetland emissions show the largest uncertainties, especially in the direction of higher emission, with more recent top-down estimates (based on inverse modeling of observations, measurements, atmospheric models, and statistical tools) ranging from 142 to 208 Tg/yr and bottom-up estimates (based on emission inventories) ranging from 177 to 284 Tg/yr [*Kirschke et al.,* 2013]. For biomass burning, top-down source estimates are ranging from 24 to 45 Tg/yr while bottom up calculations suggest a range of 32 to 39 Tg/yr [*Kirschke et al.,* 2013]. For fossil fuels (including coal) top-down estimates range from 77 to 123 Tg/yr and bottom-up estimates from 85 to 105 tg/yr [*Kirschke et al.,* 2013].

The $\delta^{13}CH_3D$, $\delta^{12}CH_2D_2$, $\Delta^{13}CH_3D$, and $\Delta^{12}CH_2D_2$ values for each major atmospheric methane source are estimated by combining the *Whiticar and Schaefer*

[2007] results for total fluxes and bulk isotopic compositions with the $^{13}CH_3D$ measurements of *Young et al.,* [2017], *Stolper et al.,* [2014], *Wang et al.,* [2015], our own theoretical calibration of the $^{12}CH_2D_2$ equilibrium, and initial $^{12}CH_2D_2$ measurements at UCLA [*Young et al.,* 2017]. The $\delta^{13}C$ and δD values for the source terms combined are calculated according to

$$\delta = \frac{\sum_i E_i \delta_i}{\sum_i E_i} \tag{7}$$

where δ_i is either $\delta^{13}C$ or δD for source i in ‰ and E_i is the flux of the source i in Tg/yr.

The abundances of doubly-substituted isotopologues in major atmospheric methane sources are not well known, though some individual sample measurements that may be representative of source components are now available [*Stolper et al.,* 2015; *Wang et al.,* 2015; *Young et al.,* 2017]. It is therefore necessary to make assumptions about some components to assemble a complete budget. Our basic approach is to assume that non-microbial source components form in internal isotopic equilibrium at temperatures characteristic of the methane formation process; this assumption is consistent with initial measurements of $^{13}CH_3D$ by *Stolper et al.,* [2014b] and *Wang et al.,* [2015]. However, measurements of $\Delta^{13}CH_3D$ in biogenic methane indicate that these sources tend not to show low-T equilibrium (i.e., $\Delta^{13}CH_3D \geq 5‰$), but are instead closer to stochastic ($\Delta^{13}CH_3D < 5‰$; [*Wang et al.,* 2015]). Furthermore, initial measurements at UCLA of $\Delta^{13}CH_3D$ and $\Delta^{12}CH_2D_2$ in microbially produced methane in the laboratory yield significant deficits in $\Delta^{12}CH_2D_2$ relative to equilibrium. We therefore use these microbial $\Delta^{13}CH_3D$ and $\Delta^{12}CH_2D_2$ measurements to represent biogenic atmospheric sources in our primary budget. Whether these reconnaissance measurements accurately represent natural systems remains to be seen, however, and it appears that microbial

communities can cycle or produce methane with either equilibrium or disequilibrium isotopologue abundances depending upon rates of processing (e.g., *Wang et al.,* 2015; *Young et al.,* 2017). To investigate this possibility, we have constructed an alternative budget by assuming an effective equilibrium at a "temperature" of 300ºC for $\Delta^{13}CH_3D$ and $\Delta^{12}CH_2D_2$ for biogenic methane, roughly matching the $\Delta^{13}CH_3D$ measurements of *Wang et al.* [2015]. Finally, we have constructed a third possible budget using the biogenic sample $\Delta^{13}CH_3D$ measurements of *Stolper et al.* [2015], along with model biogenic source $\Delta^{12}CH_2D_2$ compositions predicted by that study. These three alternative source budgets will be referred to as DM (Disequilibrium Model), pEM (pseudo-Equilibrium Microbial), and SMC-15 (*Stolper et al.* [2015] measurements and model). By considering these alternatives we are able to get a sense of how important biogenic source compositions are for the total atmospheric source isotopologue budget (Table 3). Reference bulk isotope ratios are taken to be $(^{13}C/_{12}C)_{V-PDB} = 0.0112372$ [*Assonov and Brennikmeijer,* 2003] and $(D/H)_{VSMOW} = 1.5576 \times 10^{-4}$ [*Schimmelmann et al.,* 2006].

In the discussion that follows, it will be useful to remember that δ values for $^{13}CH_3D$ or $^{12}CH_2D_2$ of air can be calculated applying equation (7) for each isotopologue, i.e., that δ-values mix in a nearly linear fashion. In contrast, Δ values are not conserved and do not necessarily follow linear mixing trends because the stochastic reference frame changes with the isotopic composition of the gas. $\Delta^{13}CH_3D$ and $\Delta^{12}CH_2D_2$ in the aggregate atmospheric source are not weighted averages of the $\Delta^{13}CH_3D$ and $\Delta^{12}CH_2D_2$ in individual sources. This property of Δ in isotopologues has been pointed out in previous studies [*Eiler and Schauble,* 2004; *Eiler,* 2007; *Stolper et al.,* 2014; *Young et al.,* 2017]. In the current study it will become particularly important when comparing closed-

system Rayleigh evolution to open-system steady state models of the atmosphere, in which $\Delta^{12}CH_2D_2$ trends in opposite directions from the source composition. The distinct behavior of $\Delta^{13}CH_3D$ in closed systems vs. open systems is also reported by *Whitehill et al.* [2017].

Table 3 – Atmospheric source models, including calculated $\Delta^{13}CH_3D$ and $\Delta^{12}CH_2D_2$ values, for atmospheric methane sources and air, based on the pseudo-Equilibrium Model (pEM), the *Stolper et al.* [2015] model predictions (SMC-15), and a Disequilibrium Model based on reconnaissance $\Delta^{12}CH_2D_2$ measurements (DM) ($\delta^{13}C$ and δD values from *Whiticar and Schaefer* [2007]; *Quay et al.,* 1999]).

Source	Flux (Tg/yr)	$\delta^{13}CH_4$ (‰)	$\delta D\text{-}CH_4$ (‰)	$\delta^{12}CH_2D_2$ (‰)	$\delta^{13}CH_3D$ (‰)	T (K)	$\Delta^{13}CH_3D$ pEM & SMC-15 (‰)	$\Delta^{12}CH_2D_2$ pEM (‰)	$\Delta^{12}CH_2D_2$ Stolper SMC-15 (‰)	$\Delta^{12}CH_2D_2$ Young DM (‰)	$\Delta^{13}CH_3D$ Young DM (‰)
Rice paddies	110	-63	-320	-528.8	-359.2	302	5.65	19.14	19.14	19.14	
Ruminants	80	-60.5	-330	-549.7	-369.5	585	1.59	3.04	20	-31.4	-0.64
Natural gas	45	-44	-180	-322.5	-213.7	433	2.98	7.57	7.57	7.57	
Coal	35	-37	-140	-254.8	-169.4	433	2.98	7.57	7.57	7.57	
Biomass burning	41	-24.6	-225	-394.83	-241.8	433	2.98	7.57	7.57	7.57	
Boreal wetlands	38	-62	-380	-607.2	-414.87	285	6.22	21.87	21.87	21.87	
Tropical wetlands	77	-58.9	-360	-582	-394.1	293	5.94	20.49	20.49	20.49	
Termites	16	-63	-390	-620.3	-425	293	5.94	20.49	20.49	20.49	
Landfills	40	-55	-310	-522.5	-346.9	585	1.59	3.04	20	-31.4	-0.64
Ocean	10	-58	-220	-379.1	-260.9	293	5.94	20.49	20.49	20.49	
Fresh water	4	-53.8	-385	-614.5	-414.8	302	5.65	19.14	19.14	19.14	
Gas hydrates	4	-62.5	-190	-338.9	-238.4	433	2.98	7.57	7.57	7.57	
Geological	0	-41.8	-200	-355.2	-231.2	433					
AMP	40	-51.2	-260	-450.7	-296.8	585	1.59	3.04	20	-31.4	-0.64
Calculated total source	540	-54.2	-295	-492.8	-330.4	253	4.76	21.7	26.57	11.83	4.11
Measured CH_4 in air	540	-47.1	-86	?	?		?	?			

2.2.2. Atmospheric sinks and kinetic isotope effects

The primary sink of atmospheric methane is •OH (90%), reactions with Cl• in the stratosphere and the marine boundary are responsible for an additional ~6% [Lelieveld et al., 1998; *Kirschke et al.,* 2013] (about 3.3% happening in MBL (Marine Boundary Layer) [*Platt et al.,* 2004]). The remaining sinks include soil reactions [*Kirschke et al.,*

2013]. There is also a small loss due to reaction with $O(^1D)$, mostly occurring in the stratosphere [*Sauer et al.*, 2015].

Kinetic isotope effects of singly substituted methane isotopologues in the •OH and Cl• reactions are known to lead to large (~200‰) D/H and minor (~5‰) $^{13}C/^{12}C$ enrichments in air [e.g., *Lasaga and Gibbs,* 1991; *Saueressig et al.,* 1995; *Roberto-Neto et al.,* 1998; *Gola et al.,* 2005; *Sellevåg et al.,* 2006; Michelsen, 2001]. The actual fractionations depend to some degree on temperature and on the radical reactant. To simplify the atmospheric steady state model, we have assumed that tropospheric radical reactions determine the atmospheric isotopologue abundances. We assume that ~96.6% of the total methane sink is due to reaction with •OH and the remaining ~3.4% by reaction with Cl•, closely matching the tropospheric •OH/Cl• sink reaction rate of *Kirschke et al.* [2013] while ignoring other minor sink processes. We calculated kinetic isotope effects for both the •OH and Cl• reactions for $^{13}CH_4$, $^{12}CH_3D$, $^{13}CH_3D$, and $^{12}CH_2D_2$.

In order to evaluate possible changes in rare isotopologues of methane during recent changes in atmospheric methane concentration, we constructed a one-box model that allows us to evaluate different scenarios, for instance by imposing sudden or gradual changes in source and sink rates. We use the rate constants of methane reactions with •OH and Cl• from *Sander* [2006] and apply our estimated kinetic isotope effects to scale the rate constants for each isotopologue. Atmospheric concentrations of •OH and Cl• were also held constant for all scenarios except where we investigated changes in •OH concentration. We use the •OH concentration estimates suggested by *Singh et al.* [1996], *IPCC Report* [2001], and *Bousquet et al.* [2005]. For Cl•, we obtained our value using the

mean concentration suggested by *Allan et al*. [2007] for MBL atomic Cl, scaled to an average tropospheric concentration [*Singh et al.,* 1996]. This yields •OH and Cl• concentrations of 10^6 molecule cm^{-3} and 1500 molecule cm^{-3}, respectively. In general, for each radical we picked a concentration within the suggested range [*Prather,* 1990; *Singh et al.,* 1996; *Bousquet et al.,* 2005] such that the destruction ratio was in reasonable agreement with *Kirschke et al.* [2013]. In our box models the •OH sink reaction is considered to be occurring at 262K, the reported effective temperature for this reaction in the troposphere [*Prather,* 1990]. For Cl• reaction with methane the temperature is considered to be 273K, since the reaction is thought to be most vigorous in the MBL (Marine Boundary Layer).

The basic mass-balance equation in all cases is

$$\frac{dn}{dt} = E - kn \quad , \tag{8}$$

where n refers to the moles of the species of interest, E refers to $\sum E_i$ where E_i are fluxes of all the sources, and $k = k_{OH}[OH] + k_{Cl}[Cl]$. The solution to (8) is

$$n(t) = n_0 e^{-kt} + \frac{E}{k}(1 - e^{-kt}) \, . \tag{9}$$

Steady-state solutions can also be obtained from Equation (9) in the limit of infinite time (effectively reached on a time scale of hundreds of years).

A gradual (exponential) increase in the overall source term leads to the differential equation:

$$\frac{dn}{dt} = E_0 e^{rt} - kn \tag{10}$$

with the solution

$$n(t) = (n_0 - \frac{E_0}{k+r})e^{-kt} + \frac{E_0}{k+r}e^{rt} \quad (11)$$

where r is the rate constant for the changing the source term. For the case of gradual changes in a specific emission source component, the equation becomes

$$\frac{dn}{dt} = E_p + E_s e^{rt} - kn \quad (12)$$

where E_s is the changing source component and E_p represents the unchanging source components. The solution to this equation is

$$n(t) = \frac{E_p}{k} + \frac{E_s}{k+r}e^{rt} + (n_0 - \frac{E_p}{k} - \frac{E_s}{k+r})e^{-kt} \quad (13)$$

.

We also consider seasonal cycles where the mass balance equation becomes periodic,

$$\frac{dn}{dt} = E_p + E_s \sin 2\pi t - kn \quad , \quad (14)$$

resulting in the time-dependent expression

$$n(t) = \frac{E_p}{k} + e^{-kt}(n_0 - \frac{E_p}{k} - \frac{E_s(-2\pi)}{k^2 + 4\pi^2}) + \frac{E_s[-2\pi\cos(2\pi t) + k\sin(2\pi t)]}{k^2 + 4\pi^2} \quad . \quad (15)$$

In Equation (15) the seasonal cycles are represented by the sinusoidal term $\sin(2\pi t)$, with a period of one year. In our calculations the initial steady-state residence time for methane in the atmosphere is 10.9 years. This is consistent with recent reported values of 11.2±1.3 years, with respect to reaction with tropospheric hydroxyl radicals [*IPCC Report,* 2013]. Applying our estimated KIE values, lifetimes for $^{13}CH_4$, $^{12}CH_3D$, $^{13}CH_3D$, and $^{12}CH_2D_2$ in the atmosphere are 11.0, 14.6, 14.7, and 21.5 years respectively. The wide variation in mean lifetime among different isotopologues leads to complex patterns of variation in isotopologue abundance ratios in non-steady state models, including the simple box model results presented below.

3. Results and Discussion

3.1 Isotope exchange equilibrium and kinetic isotope effects

Calculated equilibrium constants for exchange reactions involving singly- and doubly-substituted isotopologues are shown in Figure 3. The present results for $^{13}CH_3D$ formation agree well with previous studies, including *Webb and Miller* [2014], *Stolper et al.* [2015], and *Liu and Liu* [2016]. They also agree with a recent empirical calibration [*Wang et al.,* 2015] within measurement uncertainties. Our calculated $1000\ln(K_{eq})$ at 300K is 5.78. *Webb and Miller* [2014], using Path Integral Monte Carlo and Urey-HO methods based on high-accuracy electronic structure methods, report values of 5.73 and 5.71, respectively. These same equilibrium constants calculated by Liu and Liu [2016], using harmonic and anharmonic methods, are 5.76 and 5.81, respectively.

The calculated $1000\ln(K_{eq})$ for $^{12}CH_2D_2$ formation is considerably larger, 19.49 at 300K. Estimated equilibrium constants for $^{13}CH_3D$ and $^{12}CH_2D_2$ at the same temperature (5.72 and 19.21, respectively) were reported by *Young et al.* [2016] based on hybrid density functional theory. *Piasecki et al.* [2016] reported estimates of 5.68 and 20.17, respectively, using similar modeling methods. *Stolper et al.* [2014] estimated a $1000\ln(K_{eq})$ value of 20.42 for this exchange using harmonic vibrational frequencies tabulated by *Bottinga* [1969] based on empirical force field model calculations. A simple comparison of harmonic frequencies from our model, *Bottinga* [1969], and other *ab initio* and empirical results from the literature does not obviously point to large systematic differences in frequencies (Table 1). One possible reason for the different calculated K_{eq} values is that the frequencies tabulated by *Bottinga* [1969] are rounded to the nearest 0.1 cm^{-1}. Test calculations using that data set indicate that rounding errors of up to ±0.05

cm^{-1} are likely to induce artifacts of several tenths per mil (at ~300 K) in calculated K_{eq} values for both $^{12}CH_2D_2$ and $^{13}CH_3D$. As a further test, we determined K_{eq}'s using harmonic frequencies calculated to many decimal points of precision directly from published empirical and *ab initio* force fields [*Jones and McDowell,* 1959 -- on which the *Bottinga*, 1969 calculation are based; *Gray et al,* 1979; *Lee et al.,* 1995] and compared these with K_{eq}'s based on tabulated, rounded frequencies from the same studies (Table 1).

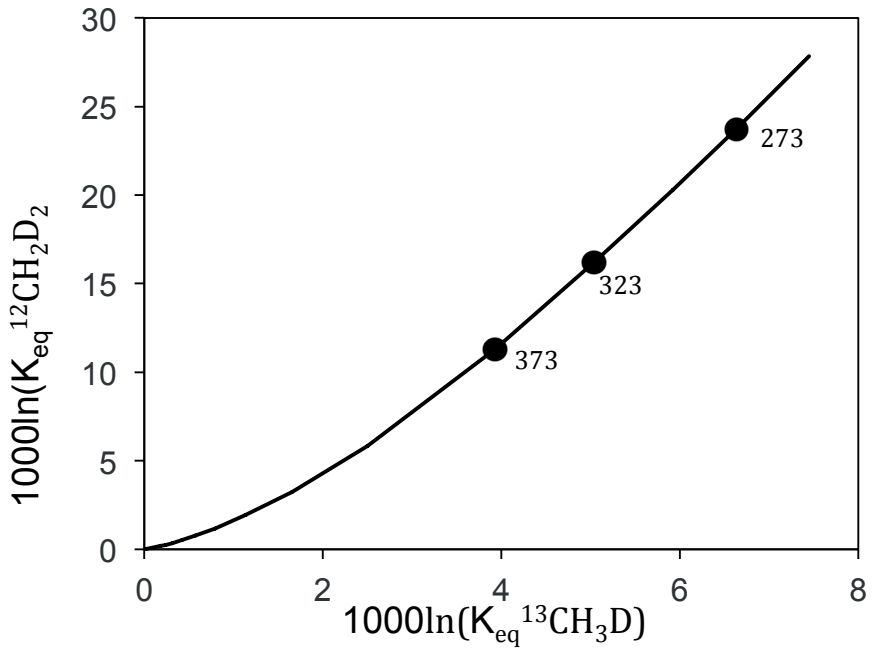

Figure 3- Equilibrium relationship between clumping equilibria for $^{12}CH_2D_2$ and $^{13}CH_3D$, determined at the MP2/cc-pVTZ level.

Discrepancies of up to 0.7‰ are apparent. The $1000\ln(K_{eq})$ values for $^{12}CH_2D_2$ based on unrounded frequencies (including our *ab initio* model) span a reasonably narrow range (19.2 - 19.7) at 300 K, whereas $1000\ln(K_{eq})$ values based on rounded, tabulated frequencies are more scattered (19.1 - 20.5).

For the sink reactions, test calculations suggest that the choice of basis sets has little effect on predicted KIEs, as long as the basis set is sufficiently large (i.e., triple-zeta or larger). The choice of model chemistry (i.e., MP2 vs. hybrid density functional theory) is more significant. Figures S1 to S4 in supplementary information present these tests. For the reaction with Cl•, the MP2/6-311++G(2d,2p) molecular structures for reactants and products are no more than 0.007 Å different from experimental values [*Boone et al.,* 2001]. For comparison, results of higher-accuracy quadratic configuration interaction with singles and doubles (QCISD) electronic structure models differ from experiment by no more than 0.004 Å [*Boone et al.,* 2001]. KIE results from MP2 model agree well with the models based on the M06 functional [*Zhao and Truhlar,* 2008], which was designed to do well predicting transition state structures and energies. Agreement with B3LYP models [*Becke,*1993] is poorer. B3LYP is known to perform rather poorly in the prediction of transition states [*Zhao and Truhlar,* 2008]. The most notable difference in the geometry of the transition state structure obtained by MP2 versus B3LYP is in the length of the reacting C---H bond. In the reaction with •OH, the C---H bond oriented towards •OH is 0.034 Å longer with B3LYP models than with MP2 models. Most critically, the imaginary frequency corresponding to the reaction coordinate is > 700 cm^{-1} higher for MP2 models with H in the reactive C--H bond, and > 500 cm^{-1} higher with D in the reactive bond. These tests indicate that the MP2 method is well suited for theoretical estimates of KIEs and equilibrium partitioning; in contrast, the B3LYP method may introduce significant additional uncertainty. Therefore, all the reported KIE values in our work are determined using MP2 in combination with the cc-pVTZ basis sets (MP2/cc-pVTZ).

We find systematic differences between theoretical and measured KIE values for singly-substituted isotopologues, as has been previously noted [*Gupta et al.,* 1997]. The differences are most noticeable for the Cl• reaction. *Gupta et al.* [1997] reported a 32‰ difference at 300K between the measured and theoretical $^{13}C/^{12}C$ KIE in the Cl• reaction, and a 5‰ difference in the reaction with •OH. The greater isotope sensitivity and theory/experiment disagreement in the Cl• reaction may reflect a transition state that is more product-like, with a longer C---H bond length to the reacting hydrogen atom, compared to a more reactant-like transition state with shorter C--H bonds in the •OH reaction. This means that in the case of Cl•, the reaction coordinate approximates a vibration of a fairly rigid H_3C group against the forming HCl molecule, with significant motion of the carbon atom, whereas the •OH reaction coordinate is mainly translation of the reacting hydrogen atom, with little motion of the carbon atom and thus little carbon isotope sensitivity.

Our model results for doubly substituted isotopologues are in a reasonably good agreement with previous measurements and theoretical studies (Table 4), including KIE values for $^{13}CH_3D$ reactions with •OH and Cl• measured and calculated by *Joelsson et al.* [2016 and 2014] (experimental values of 1.34±0.03 and 1.60±0.04 and theoretical values of 1.35 and 1.48 vs. our values of 1.33 and 1.46 at 298K, respectively). The *Joelsson et al.* measurements used Fourier transform infrared (FTIR) spectroscopy, and the authors suggest that uncertainties stemming from spectral analysis were an important source of uncertainty in their measured KIEs. However, the ultimate cause of the difference between measured and theoretical isotope effects in the reaction with Cl• does not appear to be definitively known (e.g., *Joelsson et al.,* 2014). The KIE for $^{12}CH_2D_2$, in reactions

with •OH and Cl• have also been measured at room temperature in several previous studies. The measured value for the •OH reaction is 1.81±0.28 [*Gierczak et al.*,1997]. For Cl•, measured values are 2.17±0.2, 2.45±0.05, 2.27±0.27, 1.4±0.2, and 2.19±0.02, respectively by *Sauer et al.* [2014], *Feilberg et al.* [2005], *Boone et al.* [2001], *Matsumi et al.* [1997], and *Wallington and Hurley* [1992]. The measurement by *Mastumi et al.* [1997] based on an absolute rate determination is in poor agreement with the other studies using relative rate techniques. Impurity in the chemicals and the occurrence of secondary reactions in experimental apparatus could be responsible for some of the scatter in measured KIEs [*Boone et al.*, 2001; *Sauer et al.*, 2014], however there is no definite explanation for these differences. Our calculated values for •OH and Cl• are 1.92 and 2.20, respectively, within the range of experimental determinations. In addition, *Feilberg et al.* [2005] list theoretically determined KIE values for $^{12}CH_2D_2$ reacting with Cl• as 2.16, 2.24, 2.40 [*Boone et al.*, 2001], and 2.93 [*Corchado et al.,* 2000]. The lowest theoretical KIE, 2.16, was calculated without considering tunneling effects, however, which are important for this reaction [*Boone et al.*, 2001]. The largest value, 2.93, was determined using a fundamentally different theoretical description of reaction kinetics than transition state theory, which may partly explain the discrepancy relative to the other model results [*Corchado et al.,* 2000]. *Corchado et al.* [2000] acknowledge that their method could result in overestimation of calculated KIE values compare to other experimental and theoretical values, especially at low temperatures. The much smaller difference between the remaining two theoretical results (2.24 vs. 2.40) reflects the application of two different tunneling correction factors (Eckhart vs. Wigner) [*Boone et al.*, 2001], and may give a reasonable estimate of the intrinsic theoretical uncertainty

associated with the use of simplified tunneling corrections for the methane sink reactions. Overall, as seen in Table 4 there is a significant uncertainty and scatter in both measured and theoretically determined KIEs. Even though our theoretical values lie well within the range of previous studies that observation is difficult to convert to a meaningful confidence interval. However, this uncertainty does not appear to be large enough to qualitatively affect model estimates of the impact that sink reactions on methane isotopologue species in the atmosphere, as we will show below.

Table 4 – Calculated KIEs compared with previous experimental determinations.

Table 4. Calculated KIEs Compared With Previous Experimental Determinations

	KIE (kCH_4/ki)	Present Study	Calculated Values	Experimental Values
OH	$^{13}CH_4$	1.0063	1.0030 to 1.0094[c]	1.0039 to 1.0059[a,b]
	$^{12}CH_3D$	1.32	1.26 to 1.40[a,c]	1.25[c],1.30[a]
	$^{13}CH_3D$	1.33	1.35[c]	1.34[c]
	$^{12}CH_2D_2$	1.92		1.81[d]
Cl	$^{13}CH_4$	1.028	1.021 to 1.066[e]	1.058[e]
	$^{12}CH_3D$	1.41	1.43 to 1.51[e]	1.46[e]
	$^{13}CH_3D$	1.46	1.48[f]	1.60[f]
	$^{12}CH_2D_2$	2.20	2.16 to 2.93[e]	1.40 to 2.43[g]

[a] *Gola et al.* [2005].
[b] *Cantrell et al.* [1990].
[c] *Joelsson et al.* [2016].
[d] *Gierczak et al.* [1997].
[e] *Feilberg et al.* [2005].
[f] *Joelsson et al.* [2014].
[g] *Sauer et al.* [2015].

Our calculated absolute rate constants are also in reasonable agreement with previous published measured and theoretical values by other groups [*Lassaga et al.,* 1991; *Tanaka et al.,* 1994]. For example, the *Sander et al.* [2001] experimental rate constant value for CH_4 reacting with •OH at 298K is 6.3×10^{-15}, whereas our *ab initio*

value is 9.8×10^{-15}. It is perhaps worth mentioning here that *Sauer et al.* [2014] used measured KIEs to make vertical profiles for deuterated methane isotopologues in reaction with Cl•, an exercise bearing some similarity to the atmospheric model we will present in the proceeding sections.

3.2 Steady-state model of air

Estimated abundances of singly and doubly-substituted isotopologues, including $\delta^{13}CH_3D$, $\delta^{12}CH_2D_2$, $\Delta^{13}CH_3D$, and $\Delta^{12}CH_2D_2$, in methane sources to air are shown in Table 3 and in Figures 4 and 5.

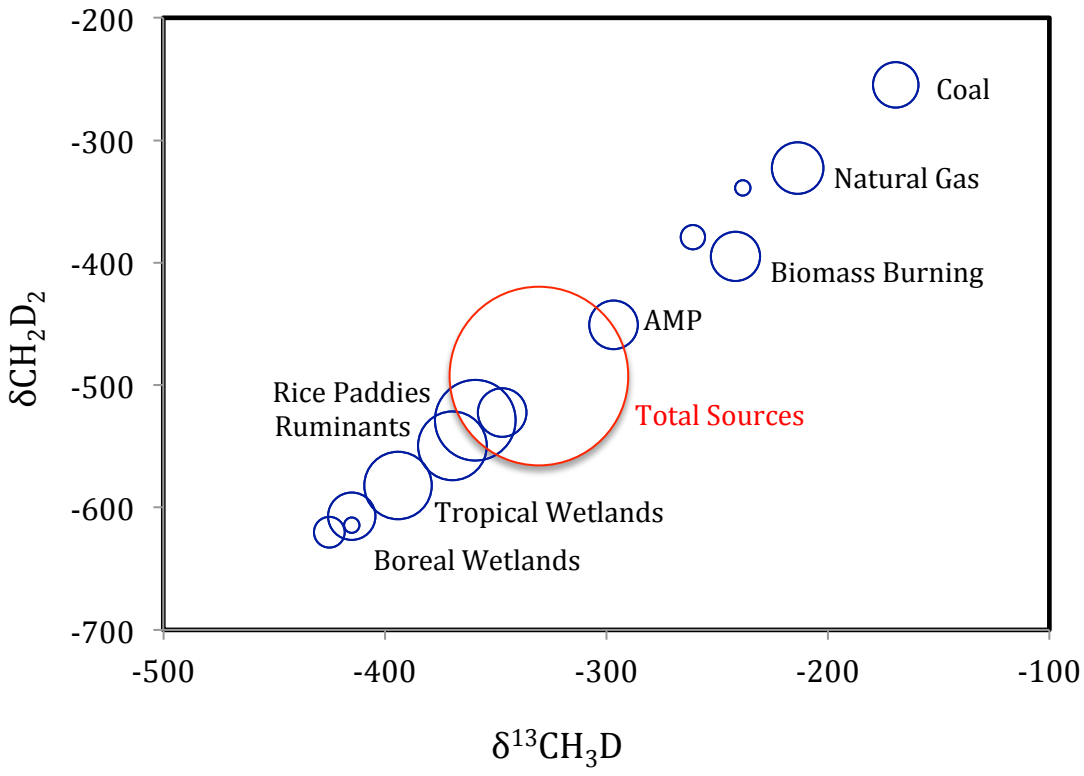

Figure 4- Estimated fluxes, $\delta^{12}CH_2D_2$ and $\delta^{13}CH_3D$ for methane sources to the atmosphere, based on the disequilibrium model (DM). The area of each circle is scaled in proportion to the flux it represents.

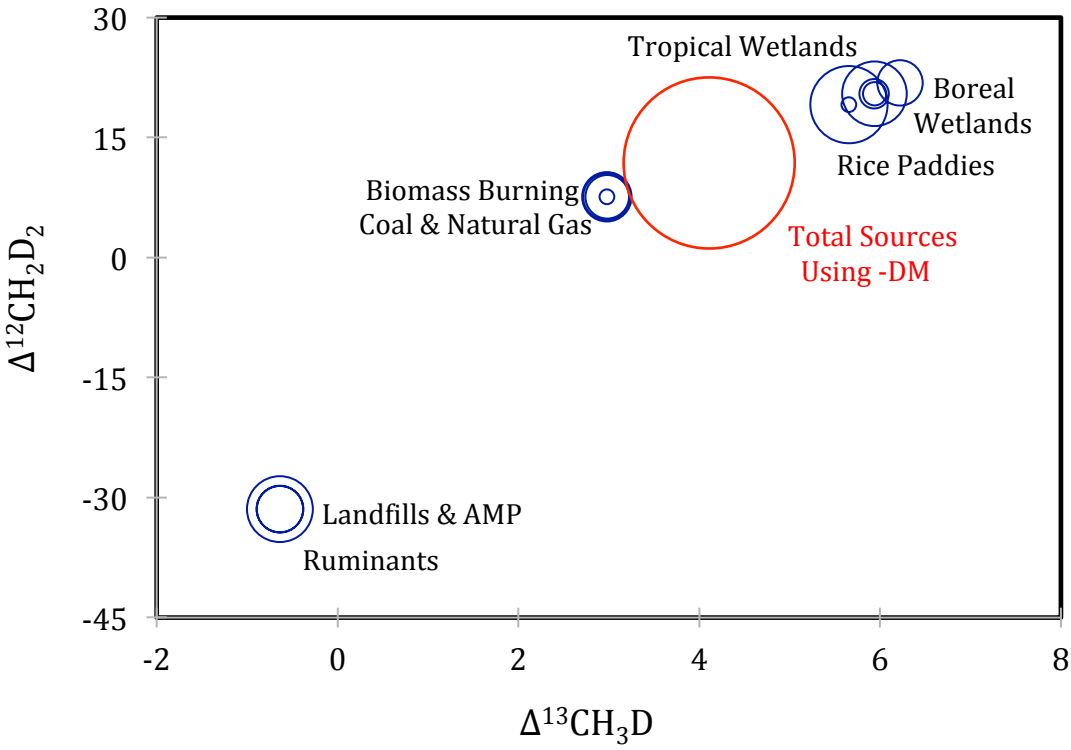

Figure 5- Estimated $\Delta^{12}CH_2D_2$ and $\Delta^{13}CH_3D$ in methane sources to air, based on the disequilibrium model (DM). The area of each circle is scaled in proportion to the flux it represents.

Using the disequilibrium microbial source budget (DM), $\delta^{13}CH_3D$ and $\delta^{12}CH_2D_2$ for the total atmospheric sources are predicted to be –330‰ and –493‰ (Figure 4) and $\Delta^{13}CH_3D$, and $\Delta^{12}CH_2D_2$ are predicted to be +4.1‰ and +11.8‰, respectively (Figure 5). Both mass-18 isotopologues are enriched relative to the stochastic distribution, mainly due to equilibrium clumping in abiogenic sources, with a small additional enrichment due to mixing. In contrast, $\Delta^{13}CH_3D$ and $\Delta^{12}CH_2D_2$ values for sources using the pseudo-equilibrium microbial assumption (pEM) are +4.7‰ and +21.7‰ respectively. Finally, $\Delta^{12}CH_2D_2$ is +26.6‰ using the predicted values by *Stolper et al.* [2015] (SMC-15). Figure 6 presents a comparison of the effects of the various assumptions for the biogenic methane composition.

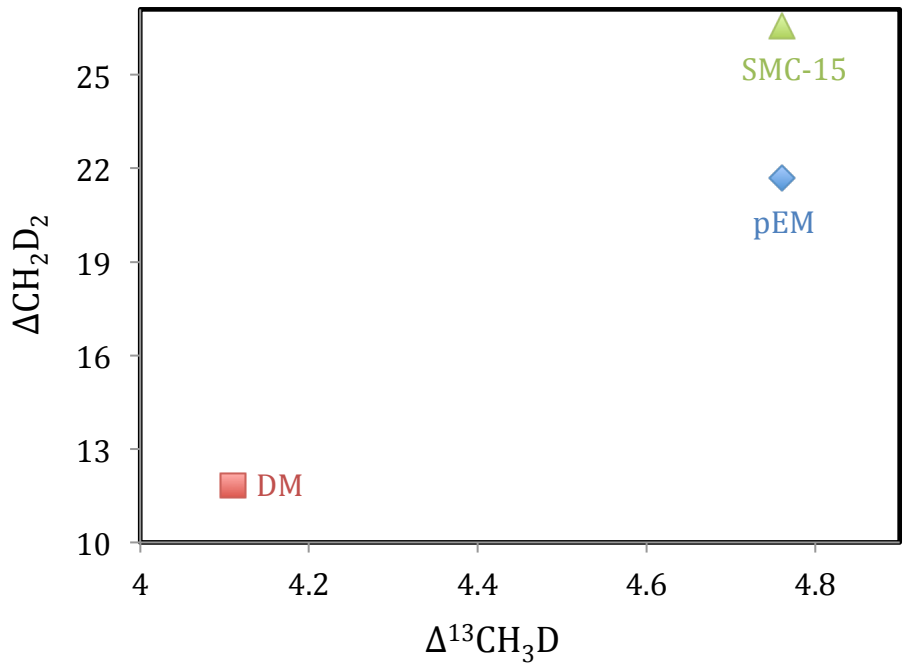

Figure 6- A comparison of the effects of different source model assumptions for isotopologue abundances in biogenic methane (Disequilibrium Model -- DM, pseudo-Equilibrium model -- pEM, and *Stolper et al.* [2015] model -- SMC-15) on the calculated $\Delta^{13}CH_3D$, and $\Delta^{12}CH_2D_2$ of the total atmospheric methane source.

A source mixing effect slightly increases $\Delta^{13}CH_3D$ because D/H and $^{13}C/^{12}C$ are positively correlated in the major methane source components ($R^2 \approx 0.37$ for all the sources, weighted equally, and $R^2 \approx 0.60$ for the 8 largest source components), and simple mixtures along a positively correlated D/H and $^{13}C/^{12}C$ gradient will have higher $\Delta^{13}CH_3D$ than the weighted average of the end members, in much the same way that $\Delta^{47}CO_2$ is higher in mixtures between high-$\delta^{18}O$, high-$\delta^{13}C$ and low-$\delta^{18}O$, low-$\delta^{13}C$ end members [*Eiler and Schauble,* 2004]. $\Delta^{12}CH_2D_2$ is similarly expected to increase when sources of varying D/H mix, as shown in the laboratory [*Young et al.,* 2016]. The total source composition is thus not at the precise position one would expect from taking a simple weighted average of Δ values in Figure 5.

Having developed an estimate of the source composition, it is interesting to consider the effects of the two major sink reactions on a closed reservoir with an initial composition set equal to the net atmospheric source, as an example of closed-system evolution. We calculated a Rayleigh distillation model at an assumed reaction temperature of –20C, i.e., ($R=R^0 f^{\alpha-1}$) where f *is* the fraction remaining of atmospheric methane in reactions with •OH and Cl• (Figure 7, 8) using the standard relation $\delta^i = (\frac{^iR_{sample}}{^iR_{standard}} - 1)(1000‰)$. As the reaction proceeds, δ values increase and Δ values decrease for both mass-18 isotopologues in the remaining methane. This signature is much more pronounced for $^{12}CH_2D_2$ (Figure 7).

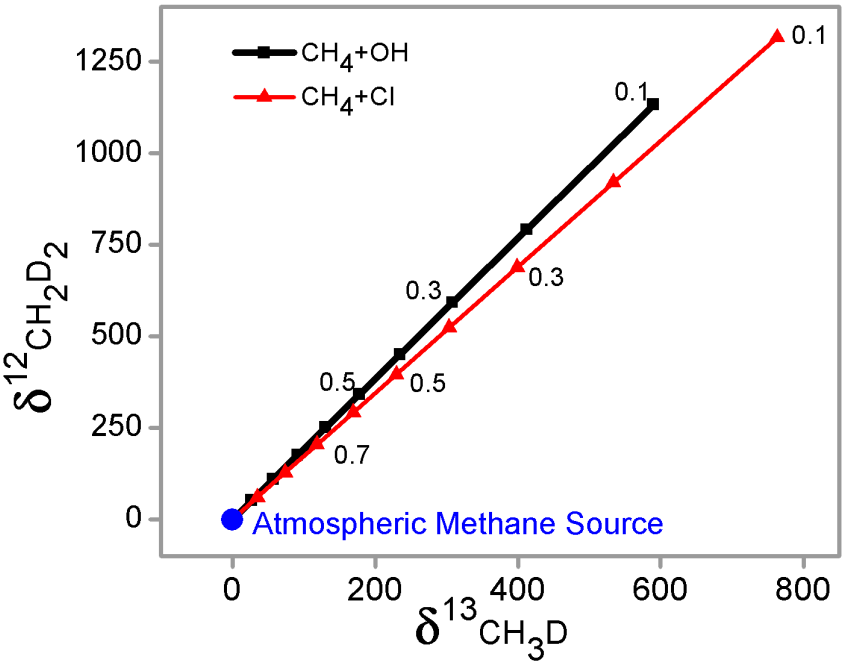

Figure 7- Estimated $\delta^{13}CH_3D$ and $\delta^{12}CH_2D_2$ in the residual gas in a Rayleigh distillation model. The initial reservoir is assumed have the atmospheric source composition predicted by the Disequilibrium Model (DM). -20C (253K) KIEs for the •OH (black thick line) and Cl• (red thin line) sink reactions are used. Tickmarks and labels indicate the fraction of gas remaining.

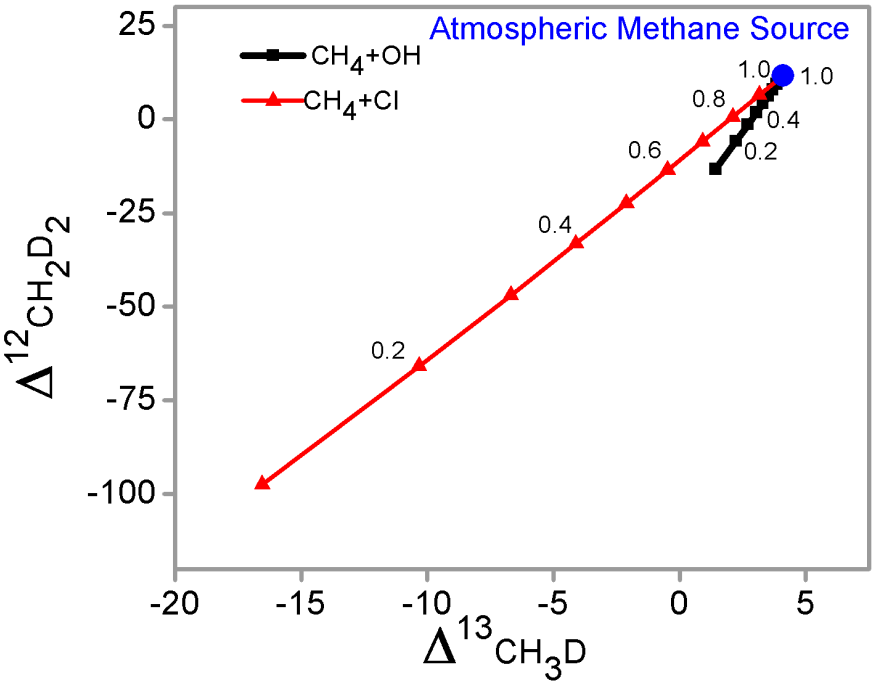

Figure 8- Estimated $\Delta^{13}CH_3D$ and $\Delta^{12}CH_2D_2$ in the residual gas in a Rayleigh distillation model. The initial reservoir is assumed have the atmospheric source composition predicted by the Disequilibrium Model (DM). -20C (253K) KIEs for the •OH (black thick line) and Cl• (red thin line) sink reactions are used. Tickmarks and labels indicate the fraction of gas remaining.

For example in reaction with •OH, when f=0.5 (50% of methane remaining) $\Delta^{13}CH_3D$ has changed from 4.1‰ to 3.3‰, but ΔCH_2D_2 changed from 11.8‰ to 4.2‰. Analogous shifts in the Cl• reaction at f=0.5 are –2.1‰ and –22.4‰ respectively.

The much larger effects on $\Delta^{12}CH_2D_2$ suggest that $^{12}CH_2D_2$ measurements are likely to be particularly well suited for investigating the overall atmospheric methane budget, especially secular changes in source and sink fluxes, while $^{13}CH_3D$ may give a more focused picture of source components.

In contrast to the closed-system Rayleigh model, a steady-state model for atmospheric CH_4 with the DM source assumption predicts $\Delta^{13}CH_3D$ and $\Delta^{12}CH_2D_2$

values of +4.5‰ and +113.5‰, respectively, with a large enrichment of $^{12}CH_2D_2$ above the stochastic reference. $\delta^{13}CH_3D$ and $\delta^{12}CH_2D_2$ values are –98.7‰ and –11.7‰, respectively in this model. Steady state values for $\delta^{13}C$ and δD are ~ –48‰ and ~ –58‰, which are reasonably close to the composition of the modern troposphere (–47‰ and –86‰ [*Quay et al.,* 1999]) (Figure 9). The alternative pseudo-equilibrium microbial (pEM) source composition yields steady-state air values for $\Delta^{13}CH_3D$ of ~5‰ and $\Delta^{12}CH_2D_2$ of ~+124‰, while $\Delta^{12}CH_2D_2$ (steady state) is ~+130‰ using the *Stolper et al.* [2015] source composition (SCM-15) (Figure 10). Overall, steady state models with various source assumptions predict that the main sink reactions in the atmosphere generate a distinct signature of higher $\Delta^{12}CH_2D_2$ relative to the source composition, also increasing $\delta^{13}CH_3D$ and $\delta^{12}CH_2D_2$. These predictions illustrate the importance of the sink reactions in controlling the relative abundance of $^{12}CH_2D_2$ in atmosphere, as well as the distinct signature of an open system with sinks and sources, relative to either process acting in isolation. They also suggest that $\Delta^{13}CH_3D$ will mainly be sensitive to source compositions, in agreement with another recent theoretical and experimental study of $\Delta^{13}CH_3D$, which predicts only a ~0.3‰ impact of the sink reactions on tropospheric methane [*Whitehill et al.,* 2017].

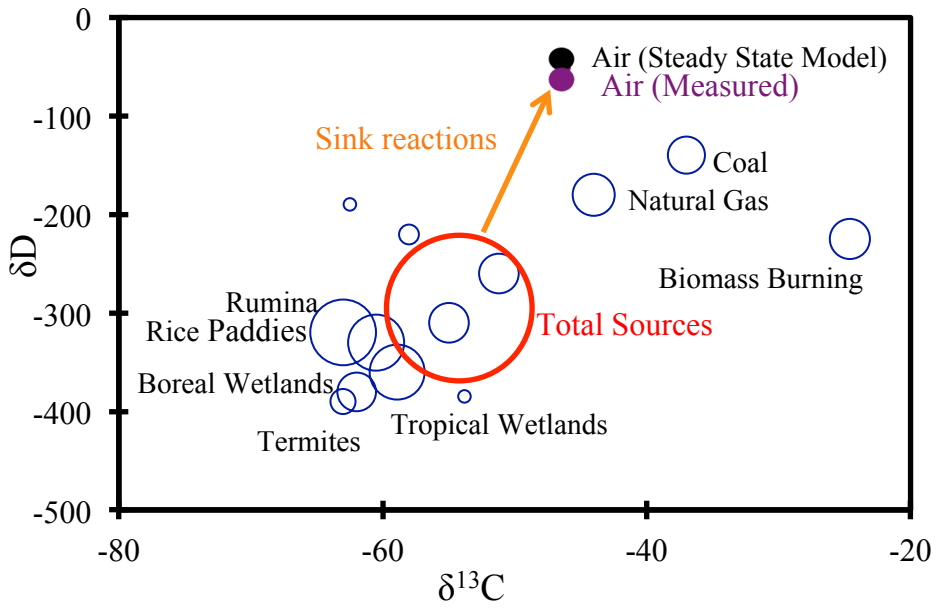

Figure 9- Singly substituted isotopologue signatures (δD and $\delta^{13}C$) of methane sources to air in the Disequilibrium Model (DM) compared to the steady-state composition using calculated KIEs for sink reactions with •OH and Cl•. The measured atmospheric composition is also shown [*Quay et al.,* 1999].

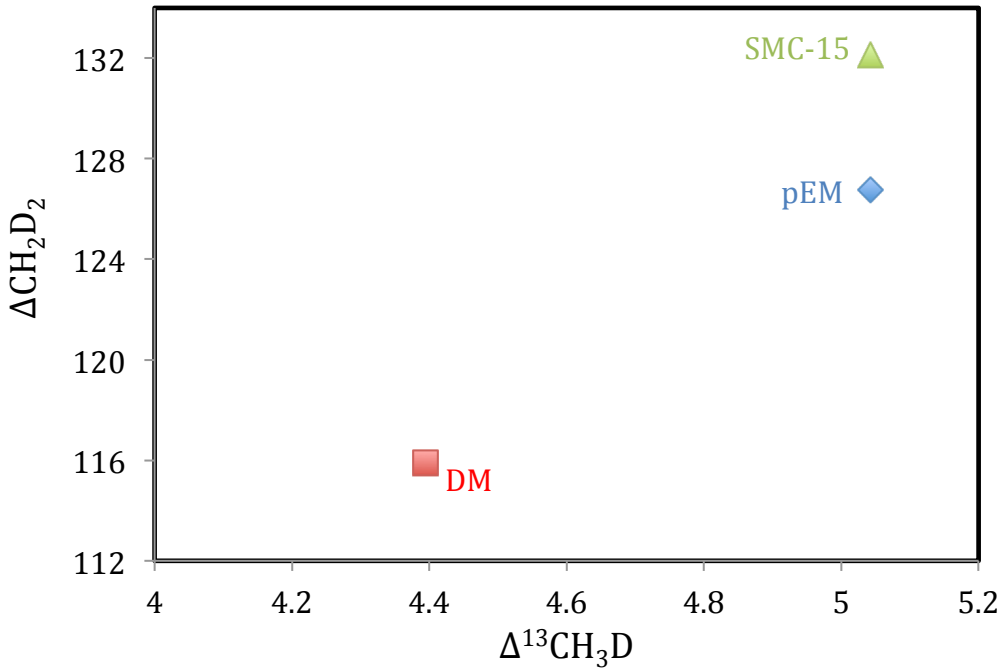

Figure 10- Doubly substituted isotopologue signatures ($\Delta^{13}CH_3D$ and $\Delta^{12}CH_2D_2$) in air at steady-state composition using the Disquilibrium Model (DM), pseudo-Equilibrium Model (pEM) and *Stolper et al.* [2015] measurements and model (SCM-15) source compositions, and calculated KIEs for reaction with •OH (96.6%) at 262K and Cl• (3.4%) at 273.

As mentioned earlier, it is well known that Δ values can show behavior distinct from δ as the result of mixing, diffusion or kinetic isotope effects [*Eiler and Schauble,* 2004; *Eiler* 2007]. This occurs because the stochastic reference frame changes with the isotopic composition of the gas. $\Delta^{12}CH_2D_2$ in our steady state model shows analogous behavior, which might be rationalized as an ongoing, mixing-like process between fresh source gas with low D/H and fractionated sink residue with roughly 210‰ higher D/H.

3.3 Isotopologue signatures of unbalanced sources and/or sinks

The recent rise in atmospheric methane could be the result of an increase in emission rate, a decrease in sink activity (via reduction in the concentration of the hydroxyl radical), or a combination of both [*Rigby et al.,* 2008; *Bosquet et al.,* 2006]. The roles of the individual emission sources in affecting the recent change of global atmospheric methane are uncertain. Therefore, in our dynamic model, we examined a number of different possibilities. After imposing changes in sources and/or sinks we monitored the evolution $\delta^{13}C$ ($\delta^{13}CH_4$), δD ($\delta^{12}CH_3D$), $\Delta^{13}CH_3D$ and $\Delta^{12}CH_2D_2$ of methane in the atmospheric air over time (Figures 11 to 14).

3.3.1 Instantaneous doubling of source components

For the first set of tests we assumed no change in the sink reaction rates and changed global emission sources to force the model out of balance. In each case, an impulse (sudden change in rate) was imposed by doubling the flux of one of the major sources (e.g., Figure 11). In the case of doubling wetland rates of methane emission, the initial $\Delta^{12}CH_2D_2$ response is a transient starting with a sudden increase to 3.0‰ above the steady-state value of 113.5‰ lasting 2 years, followed by a 7.8‰ decrease over a ~30

year period and then a gradual 8.0‰ increase, settling to a new steady-state value of 116.7‰ after ~150 years. Instantaneous doubling of wetland output therefore has a net effect of approximately 3 per mil in $\Delta^{12}CH_2D_2$ over a period of a century and a half.

Doubling both biomass burning and coal emission yields results similar to that for wetlands. The doubling of these sources causes an initial 11.0‰ decrease over approximately 25 years followed by an 13.4‰ increase to the new steady state value of 116.0‰ after roughly 120 years. For the case of doubling rice paddies, there is a sudden initial increase of 0.7‰ lasting for 2 years to a maximum value of 114.2‰, then a decrease of 9.2‰ to a minimum of 105‰ and finally attainment of a new steady state of 115.0‰ over a total period of around 120 years (Figure 11b).

The effects of emission impulses on $\Delta^{13}CH_3D$ are much smaller (figures 11c). For example, doubling wetland emission causes an initial 0.3‰ increase from the steady state value of 4.5‰, then a 0.05‰ decrease lasting for ~20 years and again a 0.1‰ increase to a new steady state of 4.9‰, a net increase of 0.4‰. In the case of doubling methane production from rice paddies, an initial increase in $\Delta^{13}CH_3D$ of 0.3‰ lasting for 5 years is followed by a 0.1‰ decrease and then a final 0.1‰ increase to reach the new steady state value of ~4.8‰, or a net increase of 0.3‰. Doubling biomass and coal burning produces a 12 year period of decrease of 0.3‰ followed by a 0.5‰ increase, reaching the new steady state value of 4.7‰ after ~70 years.

Considering these perturbation scenarios in concert, it appears that the KIEs associated with sink reactions lead to distinct lifetimes for different methane isotopologues and large contrasts between the isotopic compositions of the source flux and the atmosphere. The effects combine to cause rather complex annual to decadal

patterns of variation in isotopologue abundance ratios in non-steady state box models. The complexity reflects the residence times of $^{12}CH_4$, $^{13}CH_4$, $^{12}CH_3D$, $^{13}CH_3D$, and $^{12}CH_2D_2$ in the atmosphere with respect to reaction with •OH and Cl• of 10.9, 11.0, 14.6, 14.7, and 21.5 years, respectively. Broadly speaking, increases in source flux lead to a temporary (< 10 years) decrease in the D/H of atmospheric methane and variation in the $^{12}CH_2D_2$ excess as the reservoir mixes towards the source composition, but the reservoir moves towards a new steady state on longer timescales that roughly restores the original source/atmosphere offset in D/H (with a characteristic time scale of ~15 years) and $^{12}CH_2D_2$ excess (~22 years). Intermediate high-frequency variations may come from the distinct time scales for the evolution of the normal, singly, and doubly substituted isotopologues. We also observe, for both $\Delta^{12}CH_2D_2$ and $\Delta^{13}CH_3D$, that short and (especially) long-term responses to variations in individual source component fluxes scale to some extent with their effects on the net $\Delta^{12}CH_2D_2$ and $\Delta^{13}CH_3D$ of the total source. However, it should be emphasized that changes in the total source flux also have short-term (years to decades) effects even in the absence of any change in the isotopic composition of the total source.

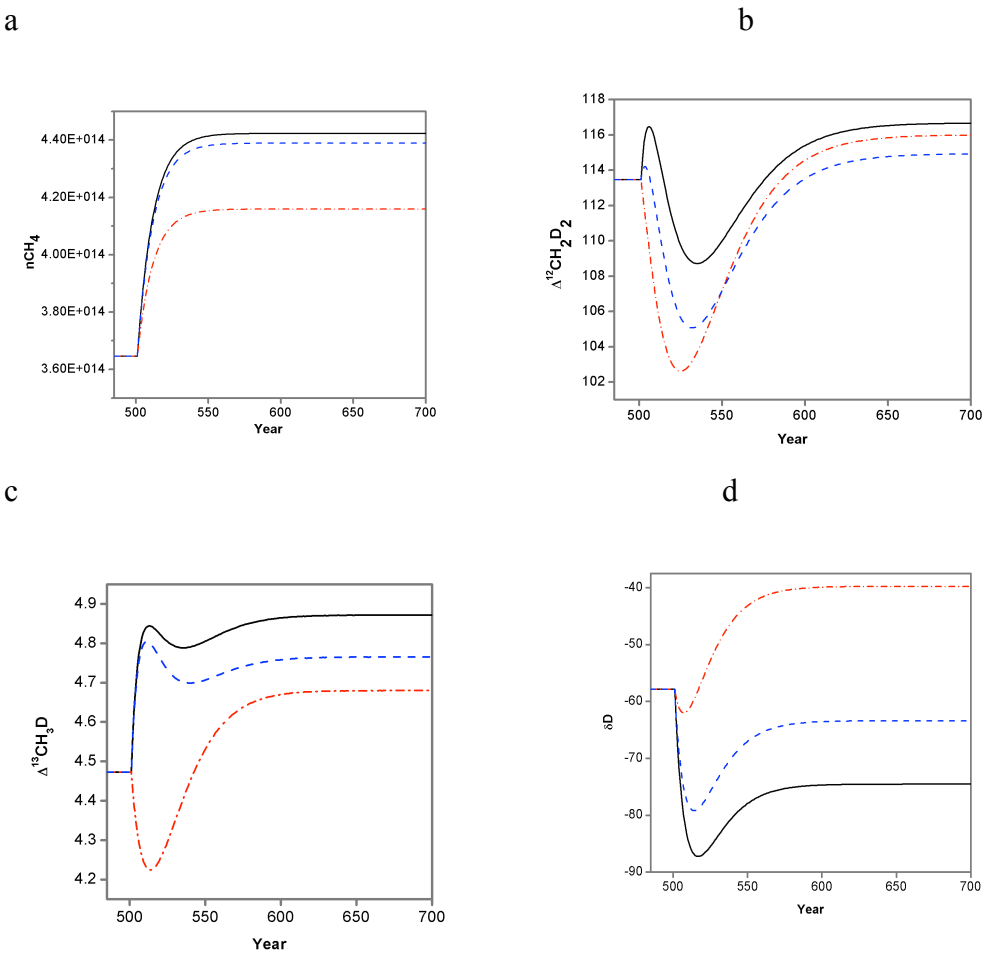

Figure 11- Dynamic box model results for a sudden, permanent doubling of wetland emissions (black line), rice paddy emissions (blue dashed line), and biomass and fossil fuel emissions (red dashed-dot line) to the atmosphere, starting from steady state: (a) number of moles of CH_4 in the atmosphere, (b) $\Delta^{12}CH_2D_2$ in air, (c) $\Delta^{13}CH_3D$ in air, (d) δD in air, and (e) $\delta^{13}C$ in air.

3.3.2 Change in •OH concentration

In order to examine the effects of changing sink rates we imposed an instantaneous change in the concentration of •OH in the atmosphere (Figures 12). The atmospheric methane budget is very sensitive to •OH concentration changes. *Dlugokencky et al.* [1996] suggested that in 1991/1992 the reduction of •OH as the result of the Mount Pinatubo volcanic eruption could be the reason behind the rise of atmospheric methane in that year. •OH concentrations in the atmosphere could also be affected by changes in the levels of atmospheric carbon monoxide (CO), the main •OH sink [*Rigby et al.,* 2008]. Reported year-to-year changes in •OH concentration vary from 2% [*Montzka et al.,* 2011] to 25% with a reported mean interannual variability (IAV) of ~7 to 9% [*Bousquet et al.,* 2005; *Prinn et al.,* 2005]. We therefore examined changes in •OH concentrations of +/- 5% as a plausible short-term step.

A 5% increase in [•OH] results in an initial $\Delta^{12}CH_2D_2$ transient consisting of an increase of 3‰ to a value of 116.5‰. The excursion requires over a decade to reach its maximum amplitude. This is much longer than the time scale of interest for small interannual variations. In contrast, the induced variation in the first year after the perturbation is less than 1‰. In the model scenario, $\Delta^{12}CH_2D_2$ reverts gradually back to a steady state of 113.6‰ over the next century or two (Figure 12b black line), ending up very close to the initial steady state composition. For $\Delta^{13}CH_3D$ the same change in [•OH] causes a sudden but much more modest decrease of less than 0.1‰ from the initial +4.5‰ lasting ~3 years followed by a 0.05‰ increase over a ~30 year period and then a 0.03‰ decrease to a new steady-state value of 4.6‰ over the next century (Figure 12c black line), reflecting the slightly changed balance of sink reactions with Cl• vs. •OH. A

5% decrease in [•OH] results in nearly the opposite response to a 5% increase (Figure 12b dashed red line, and Figure 12c dashed red line), and a 10% decrease or increase results in almost exactly twice the amplitude of variation with similar time scales, consistent with the scaling observed for source variations.

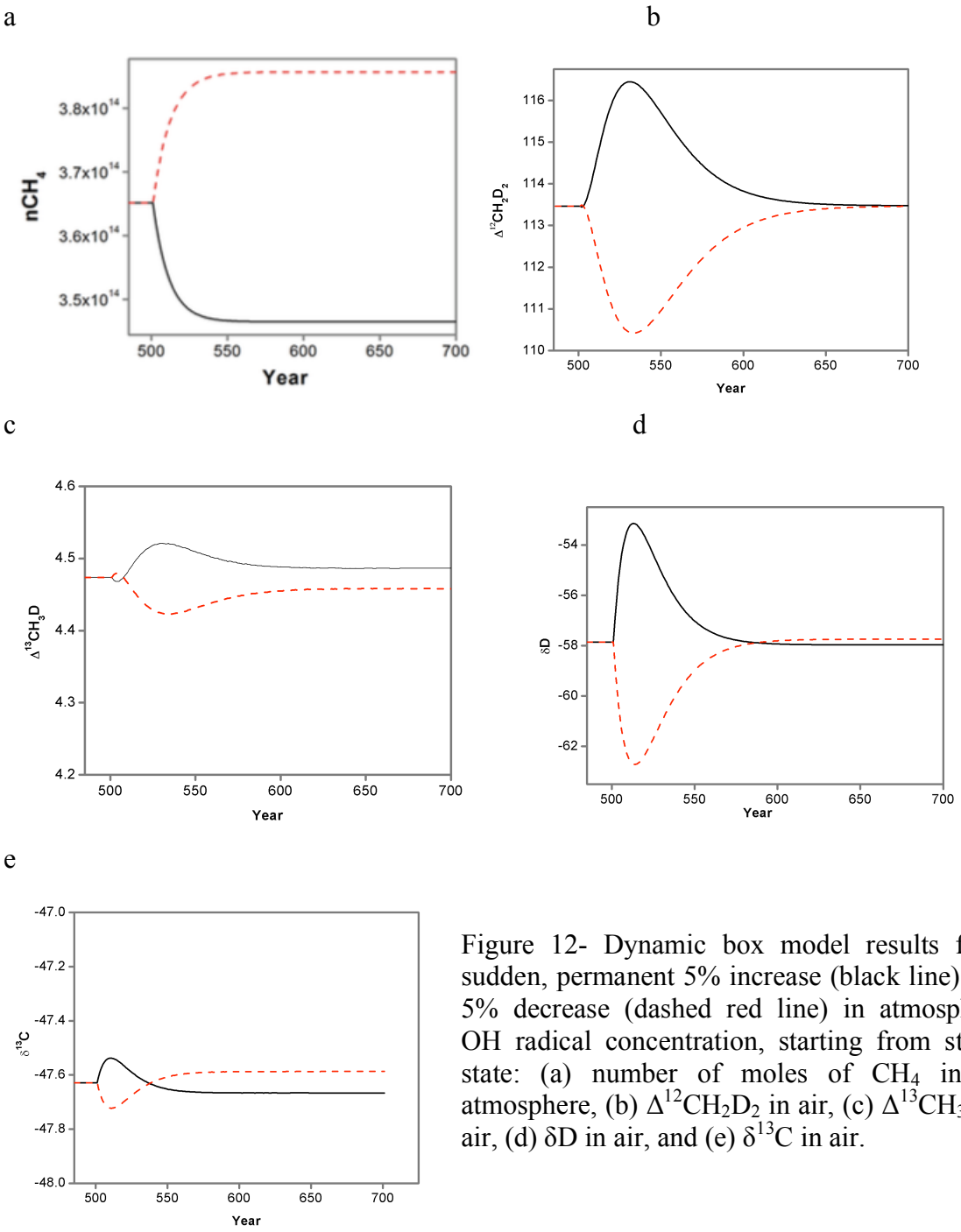

Figure 12- Dynamic box model results for a sudden, permanent 5% increase (black line), and 5% decrease (dashed red line) in atmospheric OH radical concentration, starting from steady state: (a) number of moles of CH_4 in the atmosphere, (b) $\Delta^{12}CH_2D_2$ in air, (c) $\Delta^{13}CH_3D$ in air, (d) δD in air, and (e) $\delta^{13}C$ in air.

3.3.3 Exponential increase in emission

Changes in atmospheric methane concentrations may also result from more gradual changes in sources. For instance, according to *Bousquet et al.* [2006], variations in wetland emissions were the main control of interannual variability in total source emissions (±12 Tg of CH_4/year) during the 20-year period between 1984 and 2004. Such wetland-dominated variability could explain 70% of global emission anomalies in this period. In order to approximate such a change we investigated the effects of exponentially changing source terms, extending the exponential increase out to a duration of 200 years to see how long-term, modest rates of increase compare to faster, shorter-lived scenarios (Figure 13). We examined exponential growth rates of 1%/year in the emission from all sources, and a 5%/year exponential increase in wetland source emissions with no change in other sources.

For the first case where all sources increase, $\Delta^{12}CH_2D_2$ declines from 113.5‰ to 85.0‰ over a time interval of 150 years (Figure 13d black line) during which overall emissions increased by more than 600%. $\Delta^{13}CH_3D$ increases from 4.5‰ to 4.6‰ and then decreases to 4.2‰ in this scenario (Figure 13c black line). In the case of a more rapidly increasing wetland source we first see an increase in $\Delta^{12}CH_2D_2$ of 2.0‰ from the steady state value of 113.5‰, and then a protracted reduction to a new steady state of ~49.0‰ over the next ~160 years (Figure 13d dashed red line). In this scenario, $\Delta^{13}CH_3D$ increases from the steady state value of 4.5‰ to a new steady state of 5.8‰ over this same time interval (Figure 13c dashed red line). Such a large exponential increase in wetland emission over 200 years is obviously unrealistic, but it does illustrate the asymptotic effects of long-term trends in source budgets.

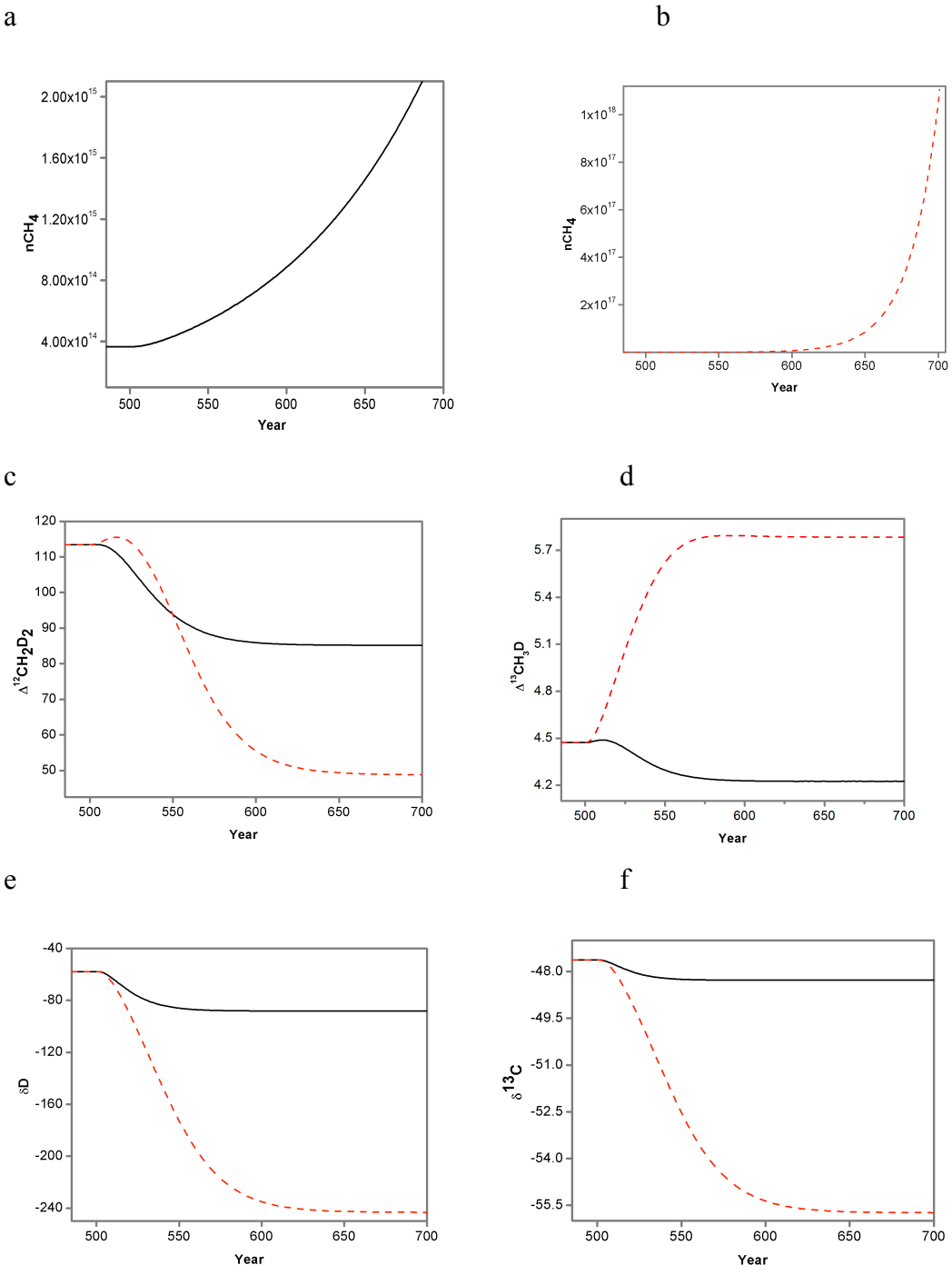

Figure 13- Dynamic box model results for exponentially increasing total CH_4 emissions (+1%/yr) (black line), and wetland emissions (+5%/yr) (dashed red line), starting from steady state: (a and b) number of moles of CH_4 in the atmosphere; (c) $\Delta^{12}CH_2D_2$ in air; (d) $\Delta^{13}CH_3D$ in air; (e) δD in air and (f) $\delta^{13}C$ in air.

In the scenario with a 5%/year exponential increase in wetland source emissions, the total wetland emissions have doubled after 14 years, and at this stage the perturbation from steady state $\Delta^{12}CH_2D_2$ and $\Delta^{13}CH_3D$ are rather similar to those found roughly 2-3 years after an instantaneous doubling wetland emissions.

3.3.4 Seasonal cycling in wetland emission

Finally, we developed a model with seasonal variations in wetland emission sources, simulating changes in surface temperature, precipitation, and other seasonal parameters, but also to serve more broadly as an analogue scenario for various proposed and observed intra- annual and short-term inter-annual variations in other source and sink components of the overall budget. We left the total integrated annual wetland emission unchanged, assuming an oscillation with a period of one year, ranging from no wetland emissions in month zero to twice the average annual wetland flux rate in month six.

We observe in the model that variations in the atmospheric reservoir caused by rapid seasonal oscillations are strongly damped by the much longer residence time of methane, resulting in only a small seasonal variation in $\Delta^{12}CH_2D_2$ (Figure 14b) of order ~0.5 ‰. Similarly, $\Delta^{13}CH_3D$ varies by less than 0.1‰ (Figure 14c) in this scenario. Overall it seems that seasonal cycling of wetland sources will only induce minor isotopic variations in the atmospheric reservoir as a whole. This is true not only for clumping signals but also for the bulk δD, which varies by only 1.9‰; $\delta^{13}C$ varies by only 0.1‰ (Figure 14d and e). By comparison, the amplitude of the seasonal cycle in $\delta^{13}C$ observed by *Quay et al.* [1999] ranges from ~0.1‰ to 0.4‰, depending on latitude.

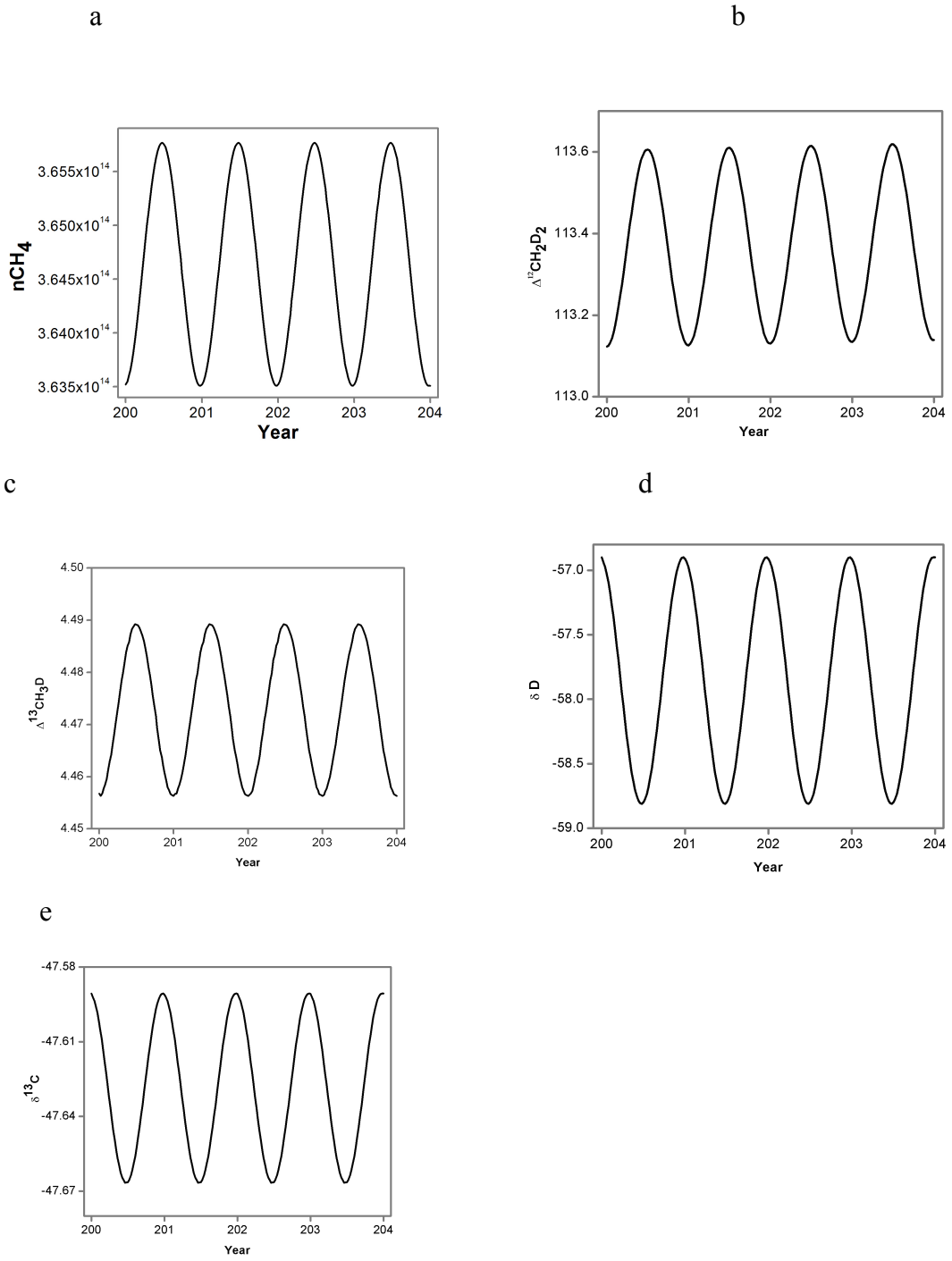

Figure 14- Dynamic box model results for seasonally variable wetland emissions (from zero in month zero to the twice the average annual wetland flux value in month six), starting from steady state: (a) number of moles of CH_4 in the atmosphere, (b) $\Delta^{12}CH_2D_2$ in air, (c) $\Delta^{13}CH_3D$ in air, (d) δD in air, and (e) $\delta^{13}C$ in air.

$\Delta^{12}CH_2D_2$ and $\Delta^{13}CH_3D$ seem to have the potential to reveal more information about the global atmosphere CH_4 budget, particularly on multi-year time scales. However, it should be noted that the potential for significant short-term perturbation signatures has not been examined at smaller spatial scales (e.g., vs. latitude or altitude) where source/sink balances may vary more dramatically, and short-term isotopic and isotopologue abundance variations may be larger.

3.4 Sensitivity Testing

3.4.1. Alternative source budgets

Global atmospheric methane budgets have previously been estimated using two basic approaches. So far we have followed a bottom-up estimated budget, as reported by *Whiticar and Schaefer* [2007] that is consistent with a total source flux of 540 Tg/yr. Coincidentally, this total flux value is the same as the *IPCC* [2013] reported value, even though that estimate is based on a top-down approach. The contributions from individual source components do differ between the two compilations.

In order to get a more extreme test of the sensitivity of the box model results to the source compositions, we altered our initial source budget to match the IPCC alternative "bottom-up" budget, which yields a total source flux of 678 Tg/yr, without changing the isotope and isotopologue compositions of each source component. Despite the change in overall flux, the altered budget yields a change of only +0.1‰ in the predicted $\Delta^{13}CH_3D$ and +3.0‰ in $\Delta^{12}CH_2D_2$ for the total estimated source composition, and similar changes in the steady state atmospheric composition. Applying the steady state model using these source flux estimates, $\Delta^{13}CH_3D$ in air will be +4.6‰ and $\Delta^{12}CH_2D_2$ +116.8‰.

Similar to the calculations described in section 3.3.1., for example, doubling emission from wetland sources (holding all source component isotopic compositions fixed) caused source $\Delta^{13}CH_3D$, and $\Delta^{12}CH_2D_2$ signatures to increase by 0.4‰ and 3‰ to values of +4.5‰ and +14.8‰, respectively. Doubling the flux from rice paddies led to a change of +0.3‰ in $\Delta^{13}CH_3D$ and +1.4‰ in $\Delta^{12}CH_2D_2$. Doubling the emission of coal and biomass burning leads to changes of +0.2‰ and +2.30‰ in $\Delta^{13}CH_3D$ and $\Delta^{12}CH_2D_2$, respectively (Figure 15). More details are in the supplementary information. Overall these tests suggest that uncertainties in the rate of emissions from various major sources will likely contribute uncertainties of ca. 1‰ and several ‰ to the net source $\Delta^{13}CH_3D$ and $\Delta^{12}CH_2D_2$, respectively.

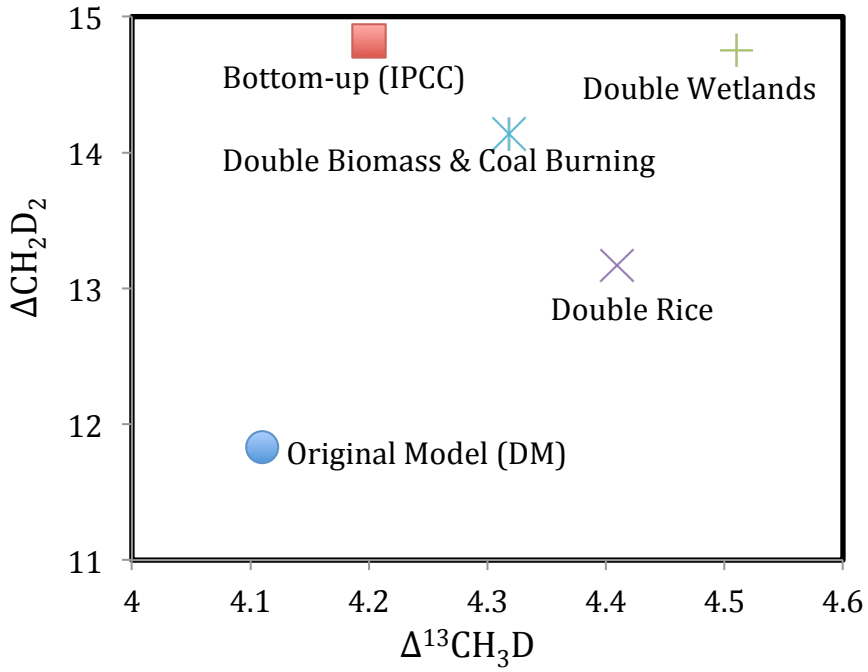

Figure 15- Sensitivity of the total atmospheric source model composition to changes in fluxes from various source components. A comparison between estimated $\Delta^{13}CH_3D$, and $\Delta^{12}CH_2D_2$ values of total atmospheric sources when doubling: wetland sources, biomass and coal sources, and rice paddies individually along with using bottom up total source emissions.

3.4.2. KIEs and sinks

As an initial test of the sensitivity of our atmospheric budgets to uncertainties or changes in kinetic isotope effects in the sink reactions, we constructed a simple heuristic KIE model in which we assumed that D cannot be abstracted from methane into the water vapor or HCl product in the reaction between CH_4 and •OH or Cl•; i.e., we assume that $k_{CH3D}=3/4k_{CH4}$ and $k_{CH2D2}=1/2k_{CH4}$, consistent with the rule of the geometric mean [*Bigeleisen,* 1955], and for simplicity further assumed that carbon isotope effects are absent in both sink reactions. The resulting atmospheric steady-state compositions are qualitatively similar to results using ab initio KIEs for all three deuterated isotopologues studied ($^{12}CH_3D$, $^{13}CH_3D$, and $^{12}CH_2D_2$). For $\Delta^{12}CH_2D_2$, the resulting steady-state atmospheric value is still notably enriched relative to the source composition at +138‰, which is about 24‰ higher than the steady state composition reached results using *ab initio* KIEs. At steady state the atmospheric $\Delta^{13}CH_3D$ retains the source value in the heuristic model, because it is assumed that there in no ^{13}C-related KIE.

As a second test, we used experimentally determined KIEs of sink reactions [*Gola. et al.,* 2005; *Joelsson et al.,* 2016; *Gierczak et al.,* 1997; *Feilberg et al.,* 2005; *Joelsson et al.,* 2014] to determine $\Delta^{13}CH_3D$ and $\Delta^{12}CH_2D_2$ of air rather than our *ab initio* model. The steady-state $\Delta^{13}CH_3D$ and $\Delta^{12}CH_2D_2$ values we obtain are +33.80 ± 26.00‰ and +101.20 ± 51.40‰ respectively. These compositions overlap with our model steady-state values using ab initio KIEs, albeit with a large range of scatter. In all cases, however, the steady-state $\Delta^{12}CH_2D_2$ is strongly enriched by the open system interaction between sources and sinks.

4. Conclusions

For the first time, expected signatures in the abundances of doubly substituted mass-18 methane isotopologues ($^{13}CH_3D$, and $^{12}CH_2D_2$) have been incorporated into a box model for the atmospheric methane budget. $^{13}CH_3D$ and $^{12}CH_2D_2$ show promise as complementary tracers of atmospheric methane sources and sinks under some circumstances, with $^{12}CH_2D_2$ in particular being sensitive to sink reactions. However, in order to make the best use of mass-18 isotopologue measurements in air, it will be important to accurately characterize the major sources and sinks of atmospheric methane in terms of flux, isotopic composition, and isotopologue signatures.

We have demonstrated that the reactions of methane with •OH and Cl• generate a distinct signature of higher $\Delta^{12}CH_2D_2$ (by ~102‰ using our ab initio KIEs) relative to the source composition. We predict high $\Delta^{12}CH_2D_2$ values of ~114‰ relative to stochastic in air at approximate steady state, in contrast to $\Delta^{13}CH_3D$ values of ~5‰ that are little different from the estimated source composition. The largest sensitivities in mass-18 isotopologue abundances come from changes in the wetland source term in our model. The effects of changing sink rates due to changing •OH concentrations are more modest but may still be measurable. Although the precision of measurements of $^{13}CH_3D$ is better compared to $^{12}CH_2D_2$ (*Young et al.,* 2017), the range of variation in composition is so much larger for $^{12}CH_2D_2$ that the doubly-deuterated isotopologue is still likely to be a more sensitive probe for investigating these types of variation in the atmospheric methane budget. Our predictions may be useful for constraining the origin and fate of methane in the atmosphere. The characteristic relationship between $\Delta^{13}CH_3D$ vs. $\Delta^{12}CH_2D_2$ may

make it possible to back-project from the composition of methane in air to constrain contributions from individual sources and sinks.

References

Alei, M., Cappis, J.H., Fowler, M.M., Frank, D.J., Goldblatt, M., Guthals, P.R., Mason, A.S., Mills, T.R., Mroz, E.J., Norris, T.L., Perrin, R.E., Poths, J., Rokop, D.J., Shields, W.R., 1987. Determination of deuterated methanes for use as atmospheric tracers. Atmos. Environ

Allan, W., Struthers, H., & Lowe, D. C. (2007). Methane carbon isotope effects caused by atomic chlorine in the marine boundary layer: Global model results compared with Southern Hemisphere measurements. *Journal of Geophysical Research Atmospheres*, *112*(4), 1–10.

Assonov, S. S., & Brenninkmeijer, C. A. M. (2003). On the ^{17}O correction for CO_2 mass spectrometric isotopic analysis. *Rapid Communications in Mass Spectrometry*, *17*(10), 1007–1016.

Becke, A. D. (1993). Density-functional thermochemistry. III. The role of exact exchange. *The Journal of Chemical Physics*, *98*(7), 5648.

Bigeleisen, J. (1955). Statistical Mechanics of Isotopic Systems with Small Quantum Corrections. I. General Considerations and the Rule of the Geometric Mean. *The Journal of Chemical Physics*, *23*(1955), 2264–2267.

Boone, G. D., Agyin, F., Robichaud, D. J., Tao, F., & Hewitt, S. A. (2001). Rate Constants for the Reactions of Chlorine Atoms with Deuterated Methanes: Experiment and Theory †. *Reactions*, 1456–1464.

Bottinga, Y., 1969. Calculated fractionation factors for carbon and hydrogen isotope exchange in the system. Geochim. Cosmochim. Acta 33, 49–64. doi:10.1016/0016-7037(69)90092-1

Bousquet, P., Ciais, P., Miller, J.B., Dlugokencky, E.J., Hauglustaine, D.A., Prigent, C., Van der Werf, G.R., Peylin, P., Brunke, E.-G., Carouge, C., Langenfelds, R.L., Lathière, J., Papa, F., Ramonet, M., Schmidt, M., Steele, L.P., Tyler, S.C., White, J., 2006. Contribution of anthropogenic and natural sources to atmospheric methane variability. Nature 443, 439–43. doi:10.1038/nature05132

Bousquet, P., Hauglustaine, D. a., Peylin, P., Carouge, C., & Ciais, P. (2005). Two decades of OH variability as inferred by an inversion of atmospheric transport and chemistry of methyl chloroform. *Atmospheric Chemistry and Physics Discussions*, *5*(2), 1679–1731.

Bousquet, P., Ringeval, B., Pison, I., Dlugokencky, E.J., Brunke, E.G., Carouge, C., Chevallier, F., Fortems-Cheiney, A., Frankenberg, C., Hauglustaine, D.A., Krummel, P.B., Langenfelds, R.L., Ramonet, M., Schmidt, M., Steele, L.P., Szopa, S., Yver, C., Viovy, N., Ciais, P., 2011. Source attribution of the changes in

atmospheric methane for 2006-2008. Atmos. Chem. Phys. 11, 3689–3700. doi:10.5194/acp-11-3689-2011

Bréas, O., Guillou, C., Reniero, F., & Wada, E. (2001). The global methane cycle: isotopes and mixing ratios, sources and sinks. *Isotopes in Environmental and Health Studies*, *37*(4), 257–379.

Cantrell, C. A., Shetter, R. E., McDaniel, A. H., Calvert, J. G., Davidson, J. A., Lowe, D. C., Greenberg, J. P. (1990). Carbon kinetic isotope effect in the oxidation of methane by the hydroxyl radical. *Journal of Geophysical Research*, *95*(D13), 22455–22462.

Cao, X., & Liu, Y. (2012). Theoretical estimation of the equilibrium distribution of clumped isotopes in nature. *Geochimica et Cosmochimica Acta*, *77*, 292–303.

Cicerone, R.J., Oremland, R. S. (1988). GLOBAL BIOGEOCHEMICAL Methane (CH_4) is the most abundant organic gas in measurement data has been reviewed by Ehhalt [1974] and Wofsy [1976] and will not be repeated here . Since the Earth ' s energy balance (see The quasi-steady state (defined in, *2*(4), 299–327.

Corchado, J.C., Truhlar, D.G., Espinosa-García, J., 2000. Potential Energy Surface, Thermal, and State-Selected Rate Coefficients, and Kinetic Isotope Effects for $Cl+CH_4 \rightarrow HCl+CH_3$. *J. Chem. Phys.* 112, 9375.

Dlugokencky, E. J., Nisbet, E. G., Fisher, R., & Lowry, D. (2011). Global atmospheric methane: budget, changes and dangers. *Philosophical Transactions. Series A, Mathematical, Physical, and Engineering Sciences*, *369*(1943), 2058–2072.

Dlugokencky, E. J., Steele, L. P., Lang, P. M., & Masarie, K. A. (1994). The growth rate and distribution of atmospheric methane. *J. Geophys. Res.*, *99*(94), 17021–17043.

Dlugokencky, E.J., Dutton, E.G., Novelli, P.C., Tans, P.P., 1996. Changes in CH_4 and CO growth rates after the eruption of Mt. Pinatubo and their link with changes in tropical tropospheric UV flux 23, 2761–2764.

Douglas, P.M.J., Stolper, D.A., Smith, D.A., Walter Anthony, K.M., Paull, C.K., Dallimore, S., Wik, M., Crill, P.M., Winterdahl, M., Eiler, J.M., Sessions, A.L., 2016. Diverse origins of Arctic and Subarctic methane point source emissions identified with multiply-substituted isotopologues. Geochim. Cosmochim. Acta 188, 163–188.

Dunning Jr, T. H. (1989). Gaussian basis sets for use in correlated molecular calculations. I. The atoms boron through neon and hydrogen. *J. Chem. Phys.*, *90*(1989), 1007.

Eiler, J. M., & Schauble, E. (2004). $^{18}O^{13}C^{16}O$ in Earth's atmosphere. *Geochimica et Cosmochimica Acta*, *68*(23), 4767–4777.

Eiler, J.M., 2007. “Clumped-isotope” geochemistry-The study of naturally-occurring, multiply-substituted isotopologues. *Earth Planet. Sci. Lett.* 262, 309–327.

Feilberg, K. L., Griffith, D. W. T., Johnson, M. S., & Nielsen, C. J. (2005). The ^{13}C and D kinetic isotope effects in the reaction of CH_4 with Cl. *International Journal of Chemical Kinetics*, *37*(2), 110–118.

Fletcher, S.E.M., Tans, P.P., Bruhwiler, L.M., Miller, J.B., Heimann, M., 2004. CH_4 sources estimated from atmospheric observations of CH_4 and its $^{13}C/^{12}C$ isotopic ratios : 1.Inverse modeling of source processes. *Global Biogeochem. Cycles* 18, 1–17.

Fung, I., John, J., Lerner, J., Matfhews, E., Prather, M., Steele, L.P., Fraser, P.J., 1991. Three-Dimensional Model Synthesis of the Global Methane Cycle. *J. Geophys. Res*. 96.

Gaussian 09: EM64L-G09RevD.01, Frisch, M. J.; Trucks, G. W.; Schlegel, H. B.; Scuseria, G. E.; Robb, M. A.; Cheeseman, J. R.; Scalmani, G.; Barone, V.; Mennucci, B.; Petersson, G. A.;Nakatsuji, H.; Caricato, M.; Li, X.; Hratchian, H. P.; Izmaylov, A. F.; Bloino, J.; Zheng, G.; Sonnenberg, J. L.; Hada, M.; Ehara, M.; Toyota, K.; Fukuda, R.; Hasegawa, J.; Ishida, M.; Nakajima, T.; Honda, Y.; Kitao, O.; Nakai, H.; Vreven, T.; Montgomery, J. A., Jr.; Peralta, J. E.; Ogliaro, F.; Bearpark, M.; Heyd, J. J.; Brothers, E.; Kudin, K. N.; Staroverov, V. N.; Kobayashi, R.; Normand, J.; Raghavachari, K.; Rendell, A.; Burant, J. C.; Iyengar, S. S.; Tomasi, J.; Cossi, M.; Rega, N.; Millam, M. J.; Klene, M.; Knox, J. E.; Cross, J. B.; Bakken, V.; Adamo, C.; Jaramillo, J.; Gomperts, R.; Stratmann, R. E.; Yazyev, O.; Austin, A. J.; Cammi, R.; Pomelli, C.; Ochterski, . J.; Dapprich, S.; Daniels, A. D.; Farkas, Ö.; Foresman, J. B.; Ortiz, J. V.;Cioslowski, J.; *Fox, D. J. Gaussian, Inc*., Wallingford CT, 2013.

Gierczak, T., Talukdar, R. K., Herndon, S. C., Vaghjiani, G. L., & Ravishankara, A. R. (1997). Rate Coefficients for the Reactions of Hydroxyl Radicals with Methane and Deuterated Methanes. *The Journal of Physical Chemistry A*, *101*(17), 3125–3134.

Gola, A.A., D’Anna, B., Feilberg, K.L., Sellevåg, S.R., Bache-Andreassen, L., Nielsen, C.J., 2005. Kinetic isotope effects in the gas phase reactions of OH and Cl with CH_3Cl, CD_3Cl, and $^{13}CH_3Cl$. Atmos. Chem. Phys. 5, 2395–2402.

Gray, D. L., Robiette, A. G., & Pine, A. S. (1979). Extended measurement and analysis of the ν3 infrared band of methane. *Journal of Molecular Spectroscopy*, *77*(3), 440–456.

Gupta, M.L., Mcgrath, M.P., Cicerone, R.J., Rowland, F.S., Wolfsberg, M., 1997. $^{12}C/^{13}C$ Kinetic Isotope Effects in the Reactions of CH4 with OH and CI 24, 2761–2764.

.Hein, R., Crutzen, P.J., 1997. An inverse modeling approach to investigate the global atmospheric methane cycle. *Global Biogeochem. Cycles* 11, 43–76.

IPCC, Climate Change 2001 IPCC Third Assessment Report, Intergovernmental Panel on Climate Change, WMO/UNEP, Wembley, UK

IPCC, Climate Change 2013 IPCC Fifth Assessment Report, Intergovernmental Panel on Climate Change, WMO/UNEP, Stockholm

Joelsson, L. M. T., Forecast, R., Schmidt, J. A., Meusinger, C., Nilsson, E. J. K., Ono, S., & Johnson, M. S. (2014). Relative rate study of the kinetic isotope effect in the $^{13}CH_3D$ + Cl reaction. *Chemical Physics Letters*, *605-606*, 152–157.

Joelsson, L. M. T., Schmidt, J. A., Nilsson, E. J. K., Blunier, T., Griffith, D. W. T., Ono, S., & Johnson, M. S. (2016). Kinetic isotope effects of $^{12}CH_3D$ + OH and $^{13}CH_3D$ + OH from 278 to 313 K. *Atmospheric Chemistry and Physics*, *16*(7), 4439–4449.

Kaye, J. A., & Jackman, C. H. (1990). Comment on "detection of multiply deuterated methane, *17*(5), 659–660.

King, S. L., Quay, P. D., Lansdown, J., M., 1989. The ^{13}C /^{12}C Kinetic Isotope Effect for Soil Oxidation of Methane increase. *J. Geophys. Res.* 94, 273–277.

Kirschke, Stefanie Kirschke, S., Bousquet, P., Ciais, P., Saunois, M., Canadell, J. G., Dlugokencky, E. J., Bergamaschi, P., Bergmann, D., Blake, D. R., Bruhwiler, L., Cameron Smith, P., Castaldi, S., Chevallier, F., Feng, L., Fraser, A., Heimann, M., Hod, G. 2013. "Three Decades of Global Methane Sources and Sinks." *Nature Geoscience* 6: 813–23.

Krishnan, R., Binkley, J. S., Seeger, R., & Pople, J. A. (1980). Self-consistent molecular orbital methods. XX. A basis set for correlated wave functions. *The Journal of Chemical Physics*, *72*(1), 650–654.

Lee, T.J.Martin, J.M.L.Taylor, P.R., 1995. An Accurate ab Initio Quartic Force Field for Formaldehyde and Its Isotopomers. J. Mol. Spectrosc. 160, 105–116.

Lelieveld, J., Crutzen, P. J., & Dentener, F. J. (1998). Changing concentration, lifetime and climate forcing of atmospheric methane. *Tellus, Series B: Chemical and Physical Meteorology*, *50*(2), 128–150.

Levin, I., Bergamaschi, P., Dorr, H., Trapp, D., 1993. Stable isotopic signature of methane from major sources in Germany. *Chemosphere* 26, 161–177.

Liu, Q., & Liu, Y. (2016). Clumped-isotope signatures at equilibrium of CH_4, NH_3, H_2O, H_2S and SO_2. *Geochimica et Cosmochimica Acta*, *175*, 252–270.

Lowe, D.C., Allan, W., Manning, M.R., Bromley, T., Ferretti, D., Gomez, A., Knobben, R., Martin, R., Mei, Z., 1999. Shipboard determinations of the distribution of ^{13}C in atmospheric methane in the Pacific. *J. Geophys. Res*. 104.

Ma, Q., Wu, S., & Tang, Y. (2008). Formation and abundance of doubly-substituted methane isotopologues ($^{13}CH_3D$) in natural gas systems. *Geochimica et Cosmochimica Acta*, *72*(22), 5446–5456.

Matsumi, Y., Izumi, K., Skorokhodov, V., Kawasaki, M., Tanaka, N., 1997. Reaction and Quenching of Cl (^2P_j) Atoms in Collisions with Methane and Deuterated Methanes. *J. Phys. Chem. A* 101, 1216–1221.

Michelsen, H. A. (2001). Carbon and hydrogen kinetic isotope effects for the reaction of Cl with \chem{CH_4}: Consolidating chemical kinetics and molecular dynamics measurements. *J. Geophys. Res.*, *106*(Dll), 12267–12274.

Møller, C., & Plesset, M. S. (1934). Note on an approximation treatment for many-electron systems. *Physical Review*, *46*(7), 618–622.

Montzka, S. a, Krol, M., Dlugokencky, E., Hall, B., Jöckel, P., & Lelieveld, J. (2011). Small interannual variability of global atmospheric hydroxyl. *Science (New York, N.Y.)*, *331*(6013), 67–69.

Mroz, E. J., Alei, M., Cappis, J. H., Guthals, P. R., Mason, A. S., & Rokop, D. J. (1989). *16*(7), 677–678.

Ono, S., Wang, D. T., Gruen, D. S., Sherwood Lollar, B., Zahniser, M. S., McManus, B. J., & Nelson, D. D. (2014). Measurement of a doubly substituted methane isotopologue, $^{13}CH_3D$, by tunable infrared laser direct absorption spectroscopy. *Analytical Chemistry*, *86*(13), 6487–6494.

Piasecki, A., Sessions, A., Peterson, B., Eiler, J., 2016. Prediction of equilibrium distributions of isotopologues for methane, ethane and propane using density functional theory. Geochim. Cosmochim. Acta. doi:10.1016/j.gca.2016.06.003

Platt, U., Allan, W., & Lowe, D. (2004). Hemispheric average Cl atom concentration from $^{13}C/^{12}C$ ratios in atmospheric methane. *Atmospheric Chemistry and Physics*, *4*, 2283–2300.

Prather J. 1990. "Tropospheric Hydroxyl Concentrations and the Lifetimes of Hydrochlorofluorocarbons (HCFCs). UNEP/WMO Scientific Assessment of Stratospheric Ozone." *WMO* 2.

Prinn, R.G., Huang, J., Weiss, R.F., Cunnold, D.M., Fraser, P.J., Simmonds, P.G., McCulloch, A., Harth, C., Reimann, S., Salameh, P., O'Doherty, S., Wang, R.H.J., Porter, L.W., Miller, B.R., Krummel, P.B., 2005. Evidence for variability of atmospheric hydroxyl radicals over the past quarter century. Geophys. Res. Lett. 32, 1–4.

Quay, P., Dlugokencky, E., 1999. The isotopic composition of atmospheric methane composition of atmospheric measurements represent the first global data are mean increased southward from of the seasonal ranged cycle in tropical in the versus a

result transport measured between content 13, 445–461.

Rigby, M., Prinn, R.G., Fraser, P.J., Simmonds, P.G., Langenfelds, R.L., Huang, J., Cunnold, D.M., Steele, L.P., Krummel, P.B., Weiss, R.F., O'Doherty, S., Salameh, P.K., Wang, H.J., Harth, C.M., M??hle, J., Porter, L.W., 2008. Renewed growth of atmospheric methane. Geophys. Res. Lett. 35, 2–7.

Roberto-neto, O., & Coitin, E. L. (1998). Dual-Level Direct Dynamics Calculations of Deuterium and Carbon-13 Kinetic Isotope Effects for the Reaction Cl+CH_4, *5639*(98), 4568–4578.

Sander, S.P., 2006. Chemical kinetics and photochemical data for use in atmospheric studies Evaluation 15. JPL Publ. 6–2, 523 pp.

Sauer, F., Portmann, R.W., Ravishankara, A.R., Burkholder, J.B., 2015. Temperature dependence of the Cl atom reaction with deuterated methanes. *J. Phys. Chem. A* 119, 4396–4407.

Saueressig, G., Bergamaschi, P., Crowley, J.N., Fischer, H., Harris, G.W., 1995. Carbon kinetic isotope effect in the reaction of CH_4 with Cl atoms. Geophys. Res. Lett. 22, 1225–1228.

Saueressig, G., Crowley, J.N., Bergamaschi, P., Brenninkmeijer, C.A.M., Fischer, H., 2001. Carbon 13 and D kinetic isotope effects in the reactions of CH_4 with $O(^1D)$ and OH: New laboratory measurements and their implications for the isotopic composition of stratospheric methane. *J. Geophys. Res*. 106.

Saunois, M., Bousquet, P., Poulter, B., Peregon, A., Ciais, P., Canadell, J.G., Dlugokencky, E.J., Etiope, G., Bastviken, D., Houweling, S., Janssens-Maenhout, G., Tubiello, F.N., Castaldi, S., Jackson, R.B., Alexe, M., Arora, V.K., Beerling, D.J., Bergamaschi, P., Blake, D.R., Brailsford, G., Brovkin, V., Bruhwiler, L., Crevoisier, C., Crill, P., Covey, K., Curry, C., Frankenberg, C., Gedney, N., Höglund-Isaksson, L., Ishizawa, M., Ito, A., Joos, F., Kim, H.S., Kleinen, T., Krummel, P., Lamarque, J.F., Langenfelds, R., Locatelli, R., Machida, T., Maksyutov, S., McDonald, K.C., Marshall, J., Melton, J.R., Morino, I., Naik, V., O'Doherty, S., Parmentier, F.J.W., Patra, P.K., Peng, C., Peng, S., Peters, G.P., Pison, I., Prigent, C., Prinn, R., Ramonet, M., Riley, W.J., Saito, M., Santini, M., Schroeder, R., Simpson, I.J., Spahni, R., Steele, P., Takizawa, A., Thornton, B.F., Tian, H., Tohjima, Y., Viovy, N., Voulgarakis, A., Van Weele, M., Van Der Werf, G.R., Weiss, R., Wiedinmyer, C., Wilton, D.J., Wiltshire, A., Worthy, D., Wunch, D., Xu, X., Yoshida, Y., Zhang, B., Zhang, Z., Zhu, Q., 2016. The global methane budget 2000-2012. Earth Syst. Sci. Data 8, 697–751.

Schimmelmann, A., Sessions, A. L., & Mastalerz, M. (2006). Hydrogen Isotopic (D/H) Composition of Organic Matter During Diagenesis and Thermal Maturation. *Annual Review of Earth and Planetary Sciences*, *34*(1), 501–533.

Sellevåg, S.R., Nyman, G., Nielsen, C.J., 2006. Study of the Carbon-13 Kinetic Isotope Effects in the Cl and OH Reactions of CH_4 and CH_3Cl. J. Phys. Chem. A 110, 141–152.

Sherwood Lollar, B., Lacrampe-Couloume, G., Slater, G.F., Ward, J., Moser, D.P., Gihring, T.M., Lin, L.H., Onstott, T.C., 2006. Unravelling abiogenic and biogenic sources of methane in the Earth's deep subsurface. Chem. Geol. 226, 328–339.

Singh, H.B., Thakur, A.N., Chen, Y.E., Kanakidou, M., 1996. Tetrachloroethylene as an indicator of low Cl atom concentrations in the troposphere. Geophys. Res. Lett. 23, 1529–1532.

Stolper, D.A., Lawson, M., Davis, C.L., Ferreira, A.A., Santos Neto, E. V, Ellis, G.S., Lewan, M.D., Martini, A.M., Tang, Y., Schoell, M., Sessions, A.L., Eiler, J.M., 2014. Formation temperatures of thermogenic and biogenic methane. Science 344, 1500–3.

Stolper, D.A., Martini, A.M., Clog, M., Douglas, P.M., Shusta, S.S., Valentine, D.L., Sessions, A.L., Eiler, J.M., 2015. Distinguishing and understanding thermogenic and biogenic sources of methane using multiply substituted isotopologues. Geochim. Cosmochim. Acta 161, 219–247.

Stolper, D.A., Sessions, A.L., Ferreira, A.A., Santos Neto, E. V., Schimmelmann, A., Shusta, S.S., Valentine, D.L., Eiler, J.M., 2014. Combined ^{13}C-D and D-D clumping in methane: Methods and preliminary results. Geochim. Cosmochim. Acta 126, 169–191.

Tanaka, N., Xiao, Y. T., & Lasaga, A. C. (1996). Ab initio study on carbon Kinetic Isotope Effect (KIE) in the reaction of CH_4 + Cl center dot. *Journal of Atmospheric Chemistry*, *23*(1), 37–49. Retrieved from <Go to ISI>://A1996TU21300003

Truong, T. N., & Truhlar, D. G. (1990). Ab initio transition state theory calculations of the reaction rate for $OH+CH_4 \rightarrow H_2O+CH_3$. *The Journal of Chemical Physics*, *93*(3), 1761.

Tsuji, K., Teshima, H., Sasada, H., & Yoshida, N. (2012). Spectroscopic isotope ratio measurement of doubly-substituted methane. *Spectrochimica Acta - Part A: Molecular and Biomolecular Spectroscopy*, *98*, 43–46.

Wang, D.T., Gruen, D.S., Lollar, B.S., Hinrichs, K.-U., Stewart, L.C., Holden, J.F., Hristov, A.N., Pohlman, J.W., Morrill, P.L., Könneke, M., Delwiche, K.B., Reeves, E.P., Sutcliffe, C.N., Ritter, D.J., Seewald, J.S., McIntosh, J.C., Hemond, H.F., Kubo, M.D., Cardace, D., Hoehler, T.M., Ono, S., 2015a. Methane cycling. Nonequilibrium clumped isotope signals in microbial methane. Science 348, 428–31.

Webb, M. A., & Miller, T. F. (2014). Position-specific and clumped stable isotope

studies: Comparison of the urey and path-integral approaches for carbon dioxide, nitrous oxide, methane, and propane. *Journal of Physical Chemistry A*, *118*(2), 467–474.

Whiticar, M., & Schaefer, H. (2007). Constraining past global tropospheric methane budgets with carbon and hydrogen isotope ratios in ice. *Philosophical Transactions, Series A*, *365*(1856), 1793–1828.

Wallington, T.J., Hurley, M.D., 1992. A kinetic study of the reaction of chlorine atoms with CF_3CHC1_2,. *Chem. Phys. Lett.* 189, 437–442.

Whitehill, A.R., Joelsson, L.M.T., Schmidt, J.A., Wang, D.T., Johnson, M.S., Ono, S., 2017. Clumped isotope effects during OH and Cl oxidation of methane. *Geochim. Cosmochim*. *Acta* 196, 307–325.

Wilmshurst, J. K., & Bernstein, H. J. (1957). the Infrared Spectra of CH_4 , CH_3D, CH_2D_2 , CD_3H, and CD_4. *Canadian Journal of Chemistry*, *35*(3), 226–235.

Wuebbles, D. J., & Hayhoe, K. (2002). Atmospheric methane and global change. *Earth-Science Reviews*, *57*(3-4), 177–210.

Young, E.D., Rumble, D., Freedman, P., Mills, M., 2016. A large-radius high-mass-resolution multiple-collector isotope ratio mass spectrometer for analysis of rare isotopologues of O_2, N_2, CH_4 and other gases. *Int. J. Mass Spectrom*. 401, 1–10.

Young, E.D., Kohl, I.E., Sherwood Lollar, B., Etiope, G., Rumble III, D., Li, S., Haghnegahdar, M. a., Schauble, E. a., Mccain, K. a, Foustoukos, D.I., Sutclife, C., Warr, O., Onstott, T.C., Hosgormez, H., Neubeck, a, Marques, J.M., Rowe, R., Larowe, D.E., Bryndzia, T., 2017. The relative abundances of resolved $^{12}CH_2D_2$ and $^{13}CH_3D$ and mechanisms controlling isotopic bond ordering in abiotic and biotic methane gases. *Geochim. Cosmochim. Acta* 203, 235–264.

Zhao, Y., Truhlar, D.G., 2008. The M06 suite of density functionals for main group thermochemistry, thermochemical kinetics, noncovalent interactions, excited states, and transition elements: Two new functionals and systematic testing of four M06-class functionals and 12 other function. Theor. Chem. Acc. 120, 215–241.

Supporting Material

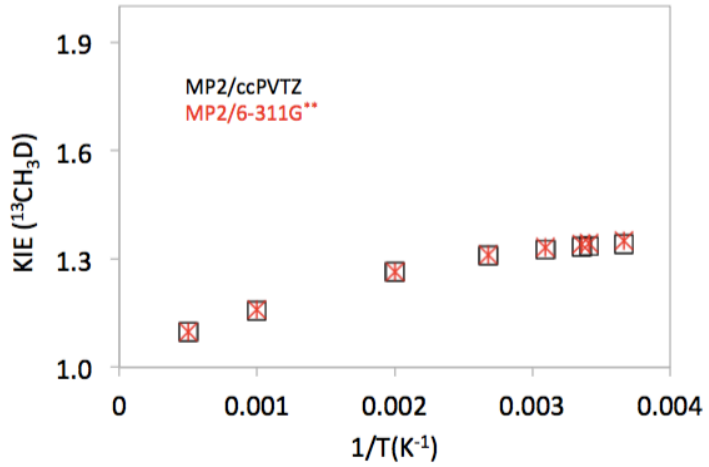

Figure S1. Testing effects of basis sets (cc-pVTZ (square) vs. 6-311G** (star)) on calculated kinetic isotope effects on $^{13}CH_3D/^{12}CH_4$ in the CH_4 - OH sink reaction. All calculations are at the MP2 level.

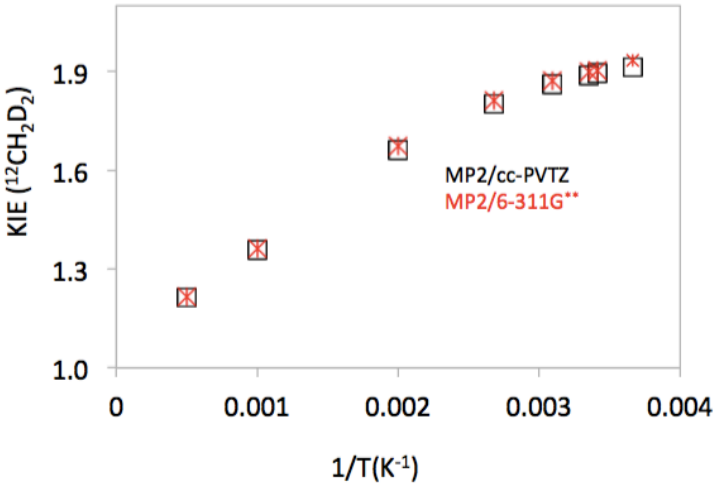

Figure S2. Testing effects of basis sets (cc-pVTZ (square) vs. 6-311G** (star)) on calculated kinetic isotope effects on $^{12}CH_2D_2/^{12}CH_4$ in the CH_4 - OH sink reaction. All calculations are at the MP2 level.

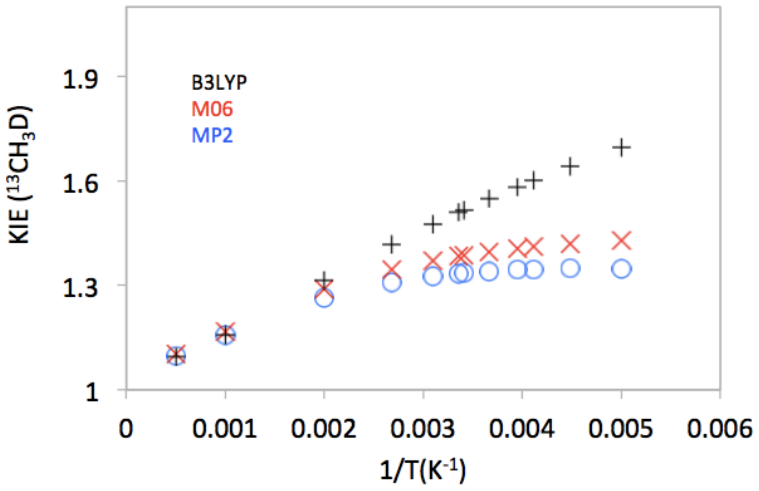

Figure S3. Testing different effects of different model chemistries (MP2 (o), B3LYP (+), and M06(×)) on calculated kinetic isotope effects on $^{13}CH_3D/^{12}CH_4$ in the CH_4 - OH sink reaction. All calculations use the cc-pVTZ basis set.

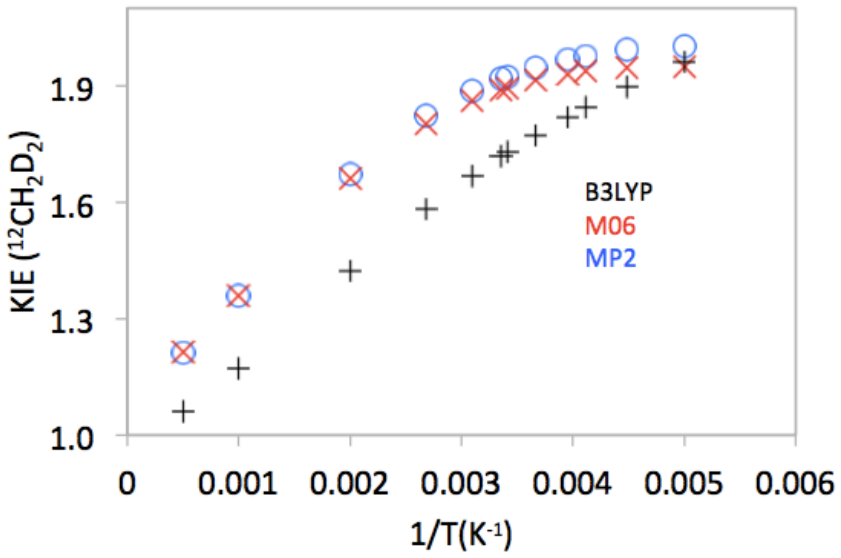

Figure S4. Testing different effects of different model chemistries (MP2 (o), B3LYP (+), and M06(×)) on calculated kinetic isotope effects on $^{12}CH_2D_2/^{12}CH_4$ in the CH_4 - OH sink reaction. All calculations use the cc-pVTZ basis set.

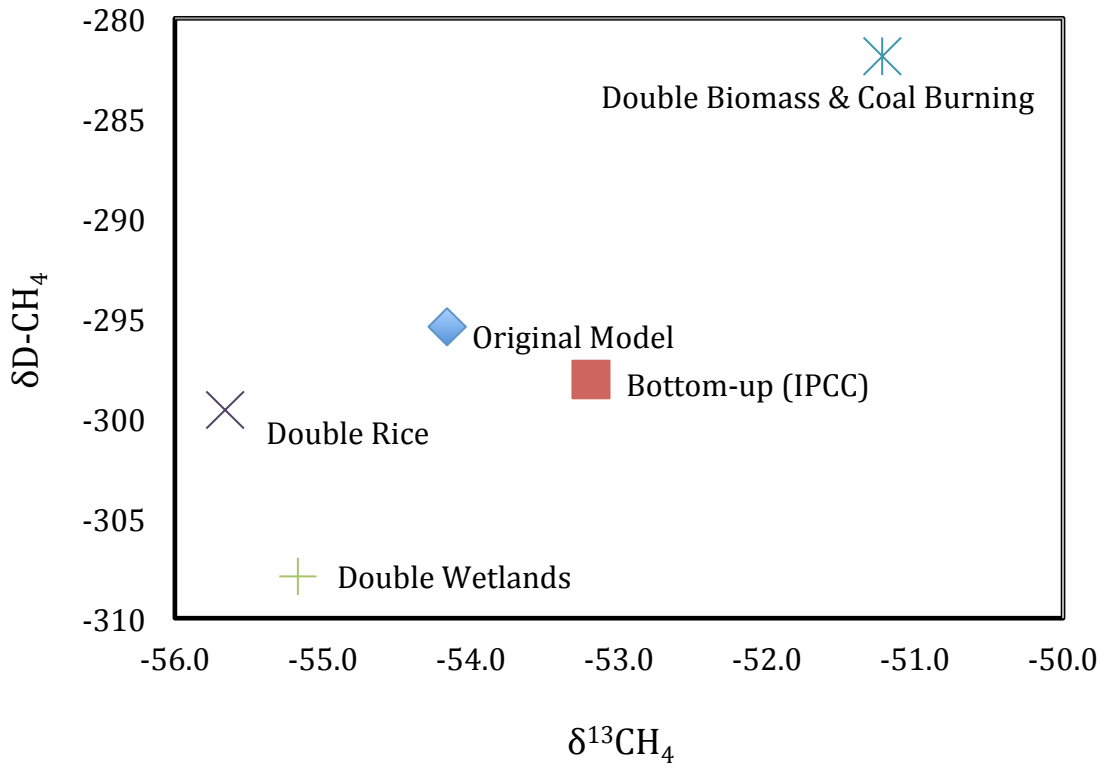

Figure S5. Sensitivity of the total atmospheric source model composition to changes in various source components. A comparison between estimated δD and $\delta^{13}C$ values of total atmospheric sources when doubling: wetland sources, biomass and coal sources, and rice paddies individually along with using bottom up total source emissions.

Table S1 – Harmonic frequencies for methane isotopologues calculated using MP2/ccpVTZ

Mode Symmetry in $^{12}CH_4$	$^{12}CH_4$	$^{13}CH_4$	$^{12}CH_3D$	$^{13}CH_3D$	$^{12}CH_2D_2$
A1	3075.9944	3075.9944	2322.0379	2310.6724	2270.4211
E	1586.2445	1586.2445	1521.9977	1521.0517	1482.7725
E	1586.2445	1586.2445	1521.9977	1521.0517	1373.9051
T2 stretch	3211.8457	3200.3597	3211.6006	3200.0822	3211.3523
T2	3211.8457	3200.3597	3211.6006	3200.0822	3150.9921
T2	3211.8457	3200.3597	3115.9725	3112.0965	2378.1067
T2 bend	1349.8133	1341.4509	1344.0747	1336.8521	1119.8727
T2	1349.8133	1341.4509	1193.0892	1184.9205	1269.619
T2	1349.8133	1341.4509	1193.0892	1184.9205	1058.6241

Table S2. Testing the effects of the Wigner [*Gupta et al.,* 1997] tunneling correction on calculated kinetic isotope effects. The KIEs this table are calculated at T=25°C.

•OH	$^{13}CH_4$	$^{13}CH_3D$	$^{12}CH_3D$	$^{12}CH_2D_2$	Cl•	$^{13}CH_4$	$^{13}CH_3D$	$^{12}CH_3D$	$^{12}CH_2D_2$
No correction	1.0063	1.3019	1.2932	1.8066	**No correction**	1.0200	1.4231	1.3946	2.1199
Corrected	1.0064	1.3334	1.3245	1.9180	**Corrected**	1.0280	1.4552	1.4154	2.2062

Table S3- Harmonic frequencies for $^{12}CH_4$-OH and $^{12}CH_4$-Cl transition states. Both transition states were optimized without structural symmetry in our MP2/cc-pVTZ models (point group C1). However, the $^{12}CH_4$-Cl transition state approached C_{3v} symmetry very closely, and likely has this symmetry at the true saddle point.

$^{12}CH_4$-OH	$^{12}CH_4$-Cl
-1798.8745	-1219.8981
16.9358	366.9022
313.6989	366.9078
347.9141	513.0943
786.064	964.8982
926.6672	964.8996
1207.8595	1218.7881
1293.6862	1449.7202
1400.8452	1449.7226
1485.1122	3129.9819
1510.0608	3300.086
3116.244	3300.0874
3249.2363	
3253.1676	
3814.4534	

Table S4. Testing the effects of source model uncertainties on the total atmospheric source composition by varying individual emission source fluxes. Isotopic and isotopologue ratios in each source component are held fixed at the Disequilibrium Model composition.

	$\Delta^{13}CH_3D$	$\Delta^{12}CH_2D_2$	$\delta^{13}CH_4$	$\delta D\text{-}CH_4$
Initial Model	4.11	11.83	-54.16	-295.43
Bottom-up (IPCC)	4.2	14.82	-53.19	-298.07
Double Wetland	4.51	14.75	-55.17	-307.92
Double Rice	4.41	13.17	-55.66	-299.58
Double Biomass Burning + Coal	4.32	14.13	-51.22	-281.90

Chapter 4. Effects of Boreal Lake Wetlands on Atmospheric $^{13}CH_3D$ and $^{12}CH_2D_2$

Abstract

Atmospheric methane has strong impacts on atmospheric chemistry and the global climate. Wetlands are among the largest methane sources, and they will need to be characterized as part of the construction of any realistic global budget of $^{13}CH_3D$ and $^{12}CH_2D_2$. In order to begin assessing $\Delta^{13}CH_3D$ and $\Delta^{12}CH_2D_2$ in atmospheric sources and sinks of methane, we analyzed methane emitted from nine boreal lakes located in Alaska, Canada, and Siberia. Measurements were performed using the Panorama high resolution mass spectrometer at UCLA. Our measurements show boreal lake methane $\Delta^{12}CH_2D_2$ and $\Delta^{13}CH_3D$ ranging from −41.6 to +18.7‰, and –1.2 to +5.4‰, respectively. Most of the samples (six of nine lakes) resemble methane from laboratory cultures of microbial methanogens, with isotopic signatures that depart markedly from the equilibrium composition of $\Delta^{12}CH_2D_2 \approx +20$ and $\Delta^{13}CH_3D \approx +6$ at plausible environmental temperatures. Based on our measurements of natural methane samples, two arrays can be defined: the microbial array with low, disequilibrium $\Delta^{12}CH_2D_2$ and $\Delta^{13}CH_3D$ resembling previously observed values for laboratory cultured samples and the methanothroph-affected array closer to the equilibrium isotopologue distribution.

Using these data, and recent predictions of future emissions growth, we modeled the likely impacts of boreal lakes on the future atmospheric CH_4 isotopologue budget up to year 2100. Our model predicts that a gradual rise of 17 Tg/yr (~3%) in boreal wetland methane emission by 2100, in comparison with a fixed methane emission scenario, will result a change of ~2‰ in atmospheric $\Delta^{12}CH_2D_2$ but less than 0.1‰ change in $\Delta^{13}CH_3D$.

δD also shows the similar behavior but in a shorter time scale, reaching a pseudo-steady state in ~50 years. The sensitivity of $\Delta^{12}CH_2D_2$ suggests a potential use for tracking changes in the atmospheric methane budget.

1. Introduction

To begin building a more realistic budget of atmospheric sources and sinks of methane that includes the abundances of multiply-substituted isotopolgues, we analyzed both $\Delta^{13}CH_3D$ and $\Delta^{12}CH_2D_2$ of methane emitted from nine boreal lakes located in Alaska, Canada, and Siberia. We also used $\Delta^{13}CH_3D$ and $\Delta^{12}CH_2D_2$ to explore the origin of methane emitted from these lakes. We modified our previously published model budget and evaluated the potential sensitivity of $\Delta^{13}CH_3D$ and $\Delta^{12}CH_2D_2$ to the likely future atmospheric methane growth causing by increase in the emission of boreal wetlands.

Methane is the most abundant organic compound in the Earth's atmosphere. It is also the second strongest greenhouse gas. Methane emissions to the atmosphere include both anthropogenic and natural sources [Saunois et al., 2016].

Wetlands play a significant role in global methane budget. With estimated emission ranging from 150 to 201 Tg/yr (~25% of total emission from all sources together [Whalen, 2005]), wetlands are the largest natural source of methane to the atmosphere [Saunois et al., 2016]. However, wetland emissions also show the largest uncertainties, especially in the direction of higher emission, with recent top-down estimates ranging from 142 to 208 Tg/yr and bottom-up estimates ranging from 177 to 284 Tg/yr [Kirschke et al., 2013]. There are two types of wetland sources: boreal and

tropical [Riley et al., 2011]. Boreal wetlands, including lakes, contain more than half the wetlands area in the Northern hemisphere [Sepulveda-Jauregui, et al., 2014]. This source is likely dominated by microbial methane ebullition (bubbling) from anoxic lake sediments [Sepulveda-Jauregui et al., 2014]. Methane emission from pan-Arctic wetlands has been increased by 20% from 1948 to 2007 in a fast response to climate change [Chen et al., 2015]. Despite the significance of high latitude wetlands in the atmospheric methane budget, there are still uncertainties. Freshwater lakes release approximately 72 Tg/year methane to the atmosphere [Bastviken et al., 2011]. Methane emissions from northern lakes (>°50 latitude) contribute 16.5±9.2 Tg CH_4/yr to global methane budget [Wik et al., 2016; Walter et al., 2006; Bastviken et al., 2011; Tan and Zhuang, 2015]. Chen et al. [2015] estimated an average flux of 36.1±6.7 Tg CH_4/yr from pan-Arctic wetlands during 1997 to 2006. Also, Olefeldt et al., [2012] offered a range of 25 to 100 Tg/yr emission of methane from boreal and tundra wetlands. There has been a sudden large growth in the extent of permafrost degradation in some regions of Alaska since 1982. This is correlated with the record warm temperatures during 1989 to 1998 – a 2 to 5 °C increase in mean annual ground temperatures relative to 1989 [Jorgenson et al., 2006, Clow and Urban, 2003]. Methane emissions from Arctic wetlands (>67°N) appear to have increased by 30.6 ± 0.9% from 2003 to 2007 [Bloom et al., 2010]. In addition, Chen et al., [2015] anticipated a rise of 42% in methane emission from Pan-Arctic wetlands by the end of 21st century, compared to the flux emitted from 1997 to 2006. Similarly, an escalation of annual emission of boreal lakes by 20 to 54% has been predicted by the end of this century, as new climate studies predict up to 9°C rise in Arctic mean annual air temperature [Wik et al., 2016]. This temperature rise in turn will

increase the destruction of northern permafrost and increase in methane emission from boreal wetlands.

Reaction with OH radical is the main methane sink in the atmosphere [Khalil et al., 2007]. The balance between methane sources and sinks determines the methane budget in the atmosphere. Methane concentration in the atmosphere has more than doubled since 1850 [Turner et al., 2017]. Also, the length of the warm season across the Arctic has increased since 1850s [Wik et al., 2016]. Atmospheric methane concentration grew by ~1%/year for the past three decades of twentieth century [Bartlett and Harriss, 1992]. Interestingly, methane concentrations stabilized in the early 2000s to 2007 and then resumed increasing [Turner et al., 2017]. Different explanations have been proposed for these trends. Turner et al. [2017] proposed that the temporary stabilization of atmospheric methane concentration was the outcome of simultaneous increase in OH radicals (and the resulting sink) and an increase in methane emission. In this model, the subsequent growth is explained by a decrease in OH radical concentration after 2007, somewhat counteracted by a drop in methane emission. In contrast, Nisbet et al. [2016] inferred that the growth in atmospheric methane since 2007 was led by an increase in the emissions from wetland sources (including rice paddies). The actual reasons behind this stabilization and then renewed growth are not fully understood.

Carbon and hydrogen stable isotope measurements ($\delta^{13}C$ and δD) have been important tools for fingerprinting different methane sources in northern lakes [Walter Anthony et al. 2012] and also for differentiating between pathways of microbial methanogenesis [Whiticar and Faber, 1986; Burke, 1993; Valentine et al., 2004; Walter et al., 2008]. Additionally, they have been used in constraining the atmospheric methane

budget [Cicerone and Oremland, 1988; Dlugokencky et al., 2011, Brownlow et al., 2017]. Different methane production and consumption processes can have characteristic isotope signatures ($\delta^{13}C$ and δD) depending on the methane formation pathway and the carbon and hydrogen isotope compositions of precursor materials [Cicerone and Oremland, 1988]. Therefore, isotope signatures measurements have been used to apportion emissions from various sources to the atmosphere in addition to identify fluctuation in the atmospheric methane sources and sinks [Fisher et al., 2017]. Yet, this type of analysis can give ambiguous results due to overlap in the isotope ranges attributed to different methane sources. In addition to pathway effects there are other factors that could influence isotope signatures including substrate limitation, and the kinetics of the reaction, transport, and oxidation. All of these factors complicate interpretation of $^{13}C/^{12}C$ and D/H signatures of methane. These contribute to overlap between bulk isotope composition of microbial, thermogenic and abiotic methane sources [Sherwood Lollar et al., 2006]. There are disagreements regarding the causes of recent anomalies in atmospheric methane concentration [Turner et al., 2017]. Multiple scenarios have been proposed in part using $\delta^{13}C$ measurements. Based on the shift to more negative values for $\delta^{13}C$ since 2007, Nisbet et al. [2016] concluded that methane regrowth was generated by significant increase in biogenic methane emissions, and that fossil fuels were not a dominant factor. Schaefer et al. [2016] developed a one-box model incorporating $\delta^{13}C$ data that also suggested fossil fuels did not contribute in the recent methane rise. In contrast, Rice et al. [2016] inferred an increase in fossil fuel sources since 2000 using $\delta^{13}C$ records. Turner et al. [2017] also described ambiguities involved in using $\delta^{13}C$ in

CH_4 to track recent atmospheric methane anomalies due to the overlap in isotopic signatures, especially among the different sources.

Doubly substituted methane isotopologues signatures are a potential tool for distinguishing between methane sources [Ma et al., 2008; Stolper et al., 2014a; Wang et al., 2015; Young et al., 2016, 2017; Haghnegahdar et al., 2017]. $^{13}CH_3D$ in particular have been proposed as a possible way to identify the formation temperature and mechanism of methane generation [Stolper et al., 2014a, 2014b; Wang et al., 2015, Young et al., 2017]. Additionally, the abundance of mass 18 methane was used to define microbial versus thermogenic sources of natural methane emission form Arctic and sub-Arctic lakes [Douglas et al., 2016]. Isotopic ratios of $^{13}CH_3D/^{12}CH_3D$ and $^{13}CH_3D/^{12}CH_4$ in natural methane have been measured using infrared spectroscopy [Tsuji et al., 2012]. Young et al., [2017] performed the first measurements that resolved both mass 18 isotope signatures of methane, $^{13}CH_3D/^{12}CH_4$ and $^{12}CH_2D_2/^{12}CH_4$, in abiotic and biotic methane collected in natural and laboratory settings. It is expected that atmospheric sink reactions cause a higher concentration of multiply substituted methane isotopes such as $^{12}CD_4$ in the atmosphere [Alei et al., 1987; Cicerone and Oremland, 1988; Mroz et al., 1989; Kaye and Jackman, 1990; Haghnegahdar et al., 2017].

In addition to measurements, there have been several theoretical studies on the equilibrium distribution of $^{13}CH_3D$ [Cao and Liu, 2012; Webb and Miller, 2014] and $^{12}CH_2D_2$ [Stolper et al., 2015; Young et al., 2016, 2017; Piasecki et al., 2016; Haghnegahdar et al., 2017]. Haghnegahdar et al. [2017] developed an initial global atmospheric methane budget including doubly substituted isotopologues of methane to

investigate the potential of $^{13}CH_3D$ and $^{12}CH_2D_2$ as tools for tracking atmospheric methane sources and sinks.

In constructing our original model, we had to make assumptions about the clumped isotope signatures of various methane sources to the atmosphere due to the lack of resolved measurements of doubly substituted isotopologues in most types of methane sources. One goal of the present study is to test and refine these assumptions.

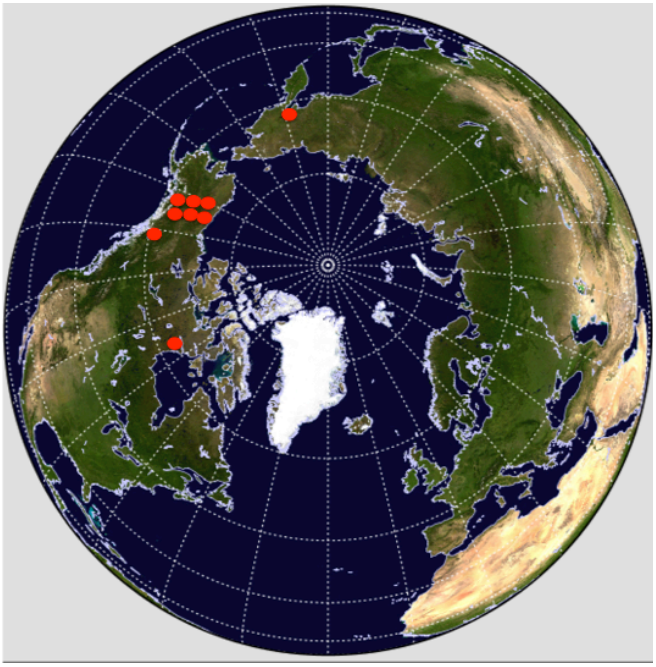

Figure 1- Map showing locations of lake samples (red circles) analyzed in this study.

2. Methods

2.1 Clumped Isotopes Measurements

We analyzed samples collected from nine lakes located at latitudes >°55 N in Siberia, Canada, and Alaska (Figure 1, table 1). The samples were chosen to represent a diverse set of cold lakes in different geographical regions of the world with different geological and ecological features along with different methane fluxes and isotope

signatures. Interior Alaska thermokarst lakes in a Pleistocene-aged yedoma silt-dominated landscape include Cranberry Lake, Vault Lake, Goldstream Lake, Octopus Lake, Doughnut Lake, and Blacksheep Pond. Doughnut Lake is thought to have an open talik, allowing hydrological exchange between the surface water and groundwater beneath permafrost. Blacksheep Pond, a smaller, 2nd generation lake, overlies permafrost consisting of refrozen sediments of a previous lake generation; due to its closed talik, there is no exchange of sub-permafrost groundwater with the surface pond water. In addition to interior Alaskan lakes, we also analyzed ebullition (bubble) samples collected from glacial lakes in eastern (Golf Lake) and western (Pickhandle Lake) Canada and from a northeast Siberian yedoma lake (Shuchi Lake). Methane ebullition samples were collected during natural ebullition (bubbling) events, during the period of 2012 to 2017 using submerged bubble traps deployed over seepage points following methods described in detail by Walter Anthony et al. [2012], except for two samples from Siberia, which were collected in 2004. Another exception are the Blacksheep Pond samples, which were collected not from natural ebullition events, but following disturbance associated with coring of pond sediments (March 2017 sample) and underlying permafrost (April 2017 sub-permfrost gas sample). All samples were stored in the dark under refrigeration until analysis. In these lakes, methane typically is produced in anoxic sediments through microbial methanogenesis. Some of the dissolved methane pool is oxidized by microbes within the sediments and lake water column [Martinez-Cruz, at al., 2017; Martinez-Cruz, at al., 2018], but a significant quantity is released to the atmosphere, mostly through ebullition (bubbling) [Walter et al., 2008; Walter Anthony et al., 2012]

Table 1- Samples information including names and locations along with latitudes and longitudes of the lakes, collected sites and dates, sample numbers, and also additional notes.

Region	Lake	Date	Notes	Latitude	Longitude
Alaska	Blacksheep Pond	3/11/17	Interior Alaska, 2nd generation thaw pond formed in an ancient thermokarst lake basin	64.8885	-147.921
Alaska	Blacksheep Pond	4/3/17	Interior Alaska, deep gas collected beneath refrozen permafrost, which formed after drainage of the ancient thermokarst lake and before formation of the recent small surface pond	64.8885	-147.921
Alaska	Cranberry	11/19/12	Interior Alaska thermokarst lake	64.936	-147.821
Alaska	Doughnut	3/15/16	Interior Alaska lake (uncertain origin)	64.899	-147.909
Alaska	Goldstream	8/7/14	Interior Alaska thermokarst lake	64.916	-147.849
Alaska	Goldstream	3/2/16	Interior Alaska thermokarst lake	64.916	-147.849
Alaska	Octopus	10/15/14	Interior Alaska thermokarst lake	64.908	-147.861
Alaska	Vault	10/30/13	Interior Alaska thermokarst lake	65.029	-147.699
Alaska	Vault	8/17/14	Interior Alaska thermokarst lake	65.029	-147.699
E.Canada	Golf	11/8/13	Eastern Canada glacial lake	58.751	-93.968
W.Canada	Pickhandle	8/30/14	Western Canadian glacial lake	61.920	-140.301
Siberia	Shuchi	5/25/04	Northeast Siberia thermokarst lake	68.746	161.394
Siberia	Shuchi	5/25/04	Northeast Siberia thermokarst lake	68.746	161.394

Prior to measurements, methane was purified from mixed gas samples using a vacuum line and gas chromatography technique similar to the method described previously by Young et al. [2017]. In general, we tried to have enough sample gas to provide at least ~60 μmole of CH_4. After purification, samples were measured using the Panorama high resolution mass spectrometer at UCLA, as described previously in detail by Young et al. [2016 and 2017]. In brief, ion currents of $^{12}CH_4^+$, $^{13}CH_4^+$, $^{12}CH_3D^+$, $^{13}CH_3D^+$, and $^{12}CH_2D_2^+$ of methane gas samples were measured. We operated at mass resolving powers (MRP) of 40,000 for clean separation of $^{12}CH_2D_2$ from $^{13}CH_3D$, corresponding to an approximate entrance slit width of 35 μm. Isotopologue ratios were obtained using two different magnet current settings; one for obtaining $\delta^{13}C$ and $\Delta^{13}CH_3D$, and the other for δD and $\Delta^{12}CH_2D_2$. Mass-16 and 17 ion currents were measured on Faraday cups with 10^{11} Ω. $^{13}CH_3D^+$ and $^{12}CH_2D_2^+$ were measured on a

secondary ion multiplier with ~6000 to 10,000 and ~150 to 250 cps, respectively. Sample aliquots were introduced to the dual inlet of the mass spectrometer using a small-volume cold finger in order to avoid expansion and thermal gradient effects. An internal reference standard with a known composition (UCLA-2) was used during the measurements. The typical measurement external precision for $\delta^{13}C$, δD, $\Delta^{13}CH_3D$, and $\Delta^{12}CH_2D_2$ measurements are respectively <0.1, 0.2, 0.2, and 0.8 ‰ 1 σ. These values are between 2 and 3 times the internal precision for each measurement. δ and Δ for methane isotopologues are:

$$\delta^i = \left(\frac{{}^iR_{sample}}{{}^iR_{standard}} - 1\right)(1000‰) \quad (1)$$

$$\Delta_j = \left(\frac{{}^jR_{sample}}{{}^jR_{stochastic}} - 1\right)(1000‰) \quad (2)$$

where R represents abundance ratios $^{13}CH_3D/^{12}CH_4$ or $^{12}CH_2D_2/^{12}CH_4$ for a sample, standard (Standard Mean Ocean Water (SMOW) and Pee Dee Belemnite (PDB)) , or stochastic equivalent.

The first one third of samples were analyzed during May, and then the rest from mid October to mid November 2017.

2.2 Model Budgets

Having the measured values for $^{13}CH_3D$ and $^{12}CH_2D_2$ of boreal wetlands, we incorporated the results into our theoretical one-box model of atmospheric methane and its isotopologue budget [Haghnegahdar et al., 2017] to make it more realistic.

It is not clear which individual sources and sinks have been responsible for the recent trends in atmospheric methane abundance over the past three decades. Therefore, we performed a historical simulation for global methane abundance from 1890 to the present testing the practicality of using clumped isotopes of methane to constrain various

scenarios. We tested two scenarios suggested by Turner et al. [2017] to simulate renewed growth in atmospheric CH_4 abundance after 2007, including a 20Tg/yr sudden increase in methane emission and 5% decrease in OH radical concentration. We assume that our measured values for doubly substituted isotopologues of methane samples from boreal lakes are typical of both wetland sources and rice paddies and left our other isotopologue assumptions unchanged. Rice paddy sources of methane share the same mechanisms and controls for methane emissions as natural wetlands. Therefore, they have been classified as agricultural wetland sources [Bartlett and Harriss, 1992; Segers, 1997; Conrad 2002]. We modeled trends in singly and doubly substituted isotopologues for the time period. In addition, we modeled the Chen et al., [2015] and also Wik et al. [2016] predictions of increasing emission of methane from boreal wetlands by the end of 21st century. In this scenario there is an exponential increase of 17 Tg/yr in boreal wetlands emission by year 2100.

3. Results and Discussion

3.1. Measurements

3.1.1 Bulk isotopes signatures

Our measured values for $\delta^{13}C$ and δD in boreal lake methane are in the range of −84.0 to −55.5‰ and −452.2 to −312.8‰ respectively (Figure 2).

The bulk isotope signatures of our samples are typical for microbial methane [Whiticar, 1999]. The lowest δD and $\delta^{13}C$ values are from Shuchi Lake, Doughnut Lake has the highest values.

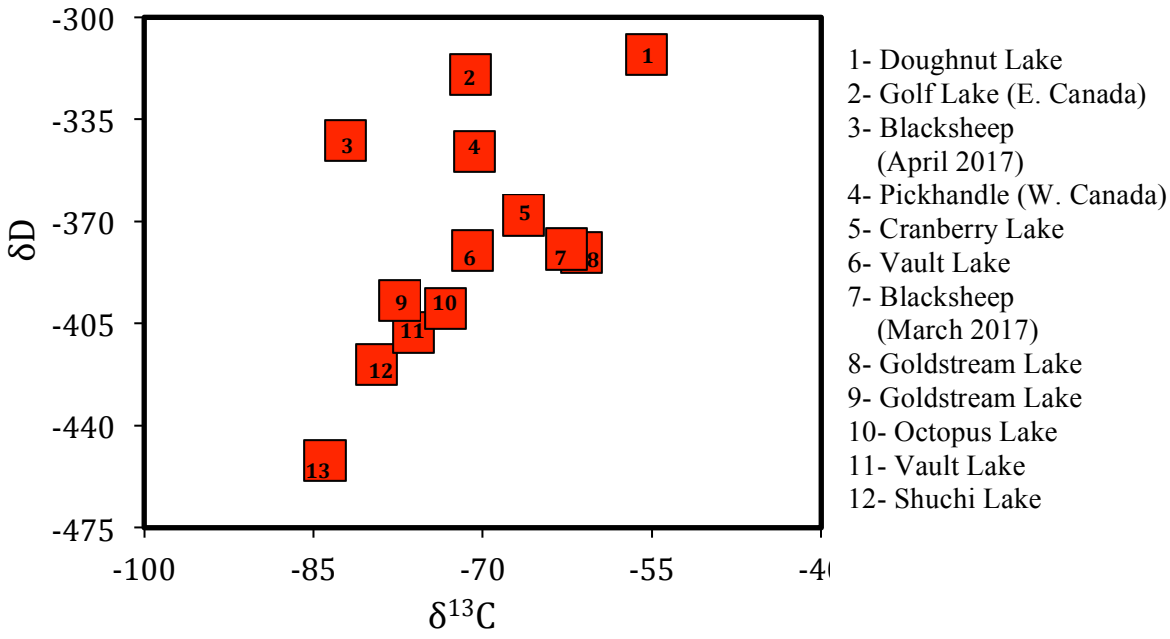

Figure 2- δD vs. $\delta^{13}C$ of natural methane samples collected from boreal lakes. δD ranges from −452.8‰ to −312.8‰, the range of $\delta^{13}C$ is between −84.0‰ and −55.5‰.

3.1.2. Clumped isotope signature

Equilibrium exchange reactions between methane isotopologues have been discussed in previous studies [Young et al., 2017; Haghnegahdar et al., 2017]. In general, if methane forms in isotopic equilibrium, the formation temperature can be indicated by clumped isotope measurements. However, resolved measurements of $\Delta^{12}CH_2D_2$ and $\Delta^{13}CH_3D$ in microbially generated methane show that microbial methanogenesis typically produces disequilibrium signatures [Young et al., 2017]. $\Delta^{12}CH_2D_2$ for methane generated by laboratory microbial samples show anti-clumped isotope signatures [Young et al., 2017; Giunta et al., 2019] (Figure 3- blue diamonds) while $\Delta^{13}CH_3D$ is typically nearly stochastic. These lab cultured samples were grown through different pathways, including with methanol and carbon dioxide sources.

$\Delta^{13}CH_3D$ for all the samples, excepting Octopus and Vault (2013-sample); show clumped signatures ($\Delta>0$). For $\Delta^{12}CH_2D_2$, all the samples except Doughnut Lake and Pickhandle have anti-clumped signatures ($\Delta<0$). All samples are far out of equilibrium. Analyzing both $\Delta^{12}CH_2D_2$ and $\Delta^{13}CH_3D$ clearly provides improved resolution of non-equilibrium signatures relative to Δ_{18} or $\Delta^{13}CH_3D$ alone. Douglas et al. [2016] measured Δ_{18} of Arctic and Subarctic lakes, including samples from Goldstream and Doughnut lakes. However, the sampling dates and ebullition events of our samples are different. For the purpose of comparison we re-calculated Δ_{18} for our samples from these lakes from resolved isotopologue measurement data using the following procedure:

$$\Delta_{18} = \left(\frac{^{18}R}{^{18}R^*} - 1\right) \quad (3)$$

, where $^{2}R = \frac{D}{H}$, $^{13}R = \frac{^{13}C}{^{12}C}$

$$^{18}R = \frac{([^{13}CH_3D]+[^{12}CH_2D_2])}{[^{12}CH_4]} \quad (4)$$

$$^{18}R^* = (6\times[^{2}R]^2) + (4\times^{2}R\times^{13}R). \quad (5)$$

Even though our samples are not replicates, overall the isotopic signatures of methane are similar (table 2).

Table 2- A comparison between our measured values for Doughnut and Goldstream lakes with Douglas et al. [2016] (analyzed samples in both studies were collected by Katey Walter Anthony but from different sites and dates).

	Lake	$\delta^{13}C$ (‰)	δD (‰)	Δ_{18} (‰)
Present Study	Doughnut	−55.5	−312.8	+5.3
	Goldstream	−77.4	−397.1	+0.4
	Goldstream	−61.2	−380.5	−0.4
Douglas et al. [2016]	Doughnut	−55.5	−302.4	+6.0
	Goldstream	−77.6	−383.1	+2.0
	Goldstream	−64.3	−369.3	+1.1
	Goldstream	−61.9	−323.8	+0.2

Our measurements of natural methane samples emitted from boreal wetlands indicate that typical compositions fall within an array with low, disequilibrium $\Delta^{12}CH_2D_2$ and $\Delta^{13}CH_3D$. $\Delta^{12}CH_2D_2$ ranges from −41.6 to +18.7‰, while the range of $\Delta^{13}CH_3D$ is between –1.2 to +5.4‰. Laboratory studies on microbial cultured samples show a similar range of values for $\Delta^{12}CH_2D_2$, –55.3 to –19.4‰, and $\Delta^{13}CH_3D$, –3.9 to +2.7‰, [Young et al., 2017; Giunta et al., 2018].

Samples from three lakes (Doughnut, Pickhandle, and Blacksheep–April sample) are distinct from the others. They are closer to the equilibrium curve and farther from the measurements of microbial lab cultured samples (Figure 3).

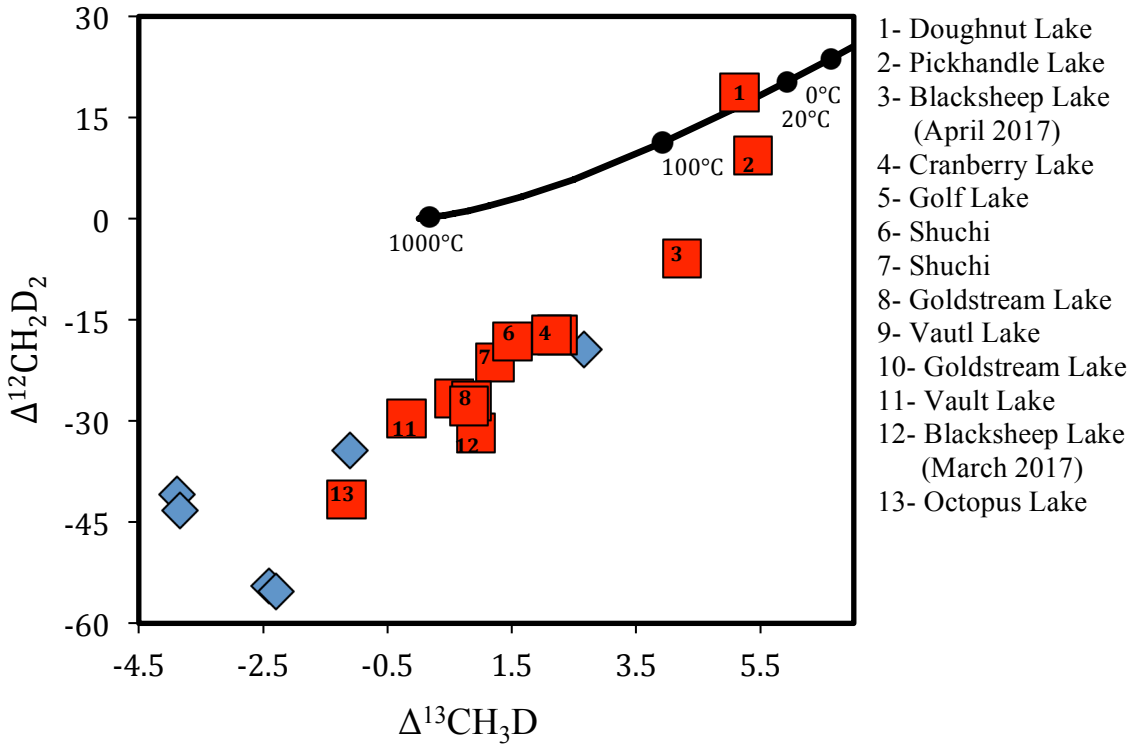

Figure 3- Measured values for boreal lakes (red triangles), along with the equilibrium curve (black). Black points on the curve represent equilibrium temperatures. Laboratory cultures of microbial methanogens are shown in blue diamonds.

Isotopic and contextual evidence suggests that these unusual compositions represent samples originating from deeper subsurface methane sources that were likely to have been affected by AOM (Anaerobic Methane Oxidation by methanotrophs). Martinez-Cruz et al. [2017, 2018] observed AOM in the surface of sediments of interior Alaska lakes, including Doughnut Lake. Winkel et al. (in review) reported microbial communities naturally enriched in CH_4-oxidizing archaea associated with AOM in deep sediments near the base of the talik at Vault Lake. Here, we suggest that AOM leads to

partial equilibration of methane due to the reversibility of the methyl-coenzyme M reductase (MCR) reaction in the first step [Young et al. 2017]. Hence, the observed doubly substituted isotopologue signatures of these three lakes could be the result of mixing between a sample dominated by a methanogenesis signature and gas equilibrated by methanothrophy (Figure 4). For instance, a mixing at 5°C - between a sample from Goldstream Lake (that is apparently dominated by a methanogenesis signature) with δD=−380.5‰ and $\delta^{13}C$=−61.2‰ and gas equilibrated by methanotrophy with a composition of δD=−294.1‰ and $\delta^{13}C$= −53.5‰ (this composition is chosen so that the mixing line passes through the sample at Doughnut Lake), gives the trajectory shown in Figure 4. Similar mixing relationships can constructed to pass through the Pickhandle and Blacksheep–April sample compositions (Figure 5).

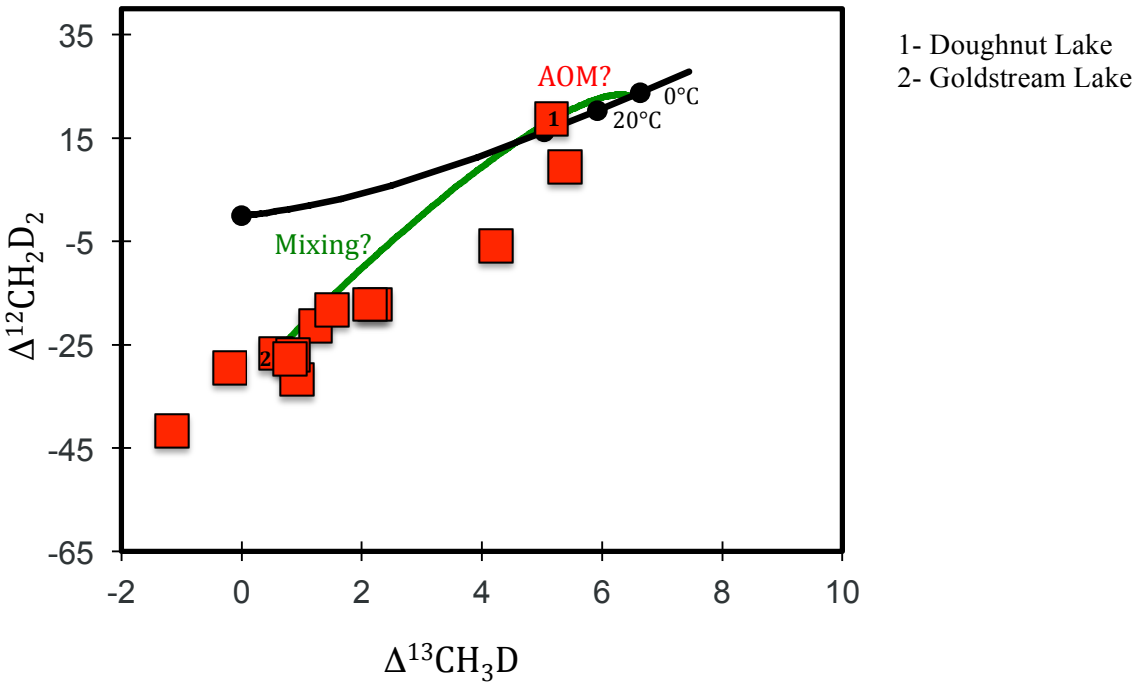

Figure 4- Hypothetical mixing trajectory from the composition of the Goldstream Lake sample through the Doughnut Lake sample composition, calculated such that a gas equilibrated at 5°C is the mixing end member. The microbial and AOM end-member

gases would have δD=−380.5‰, $\delta^{13}C$=−61.2 and δD=−245.0‰, $\delta^{13}C$=−50.0‰ respectively.

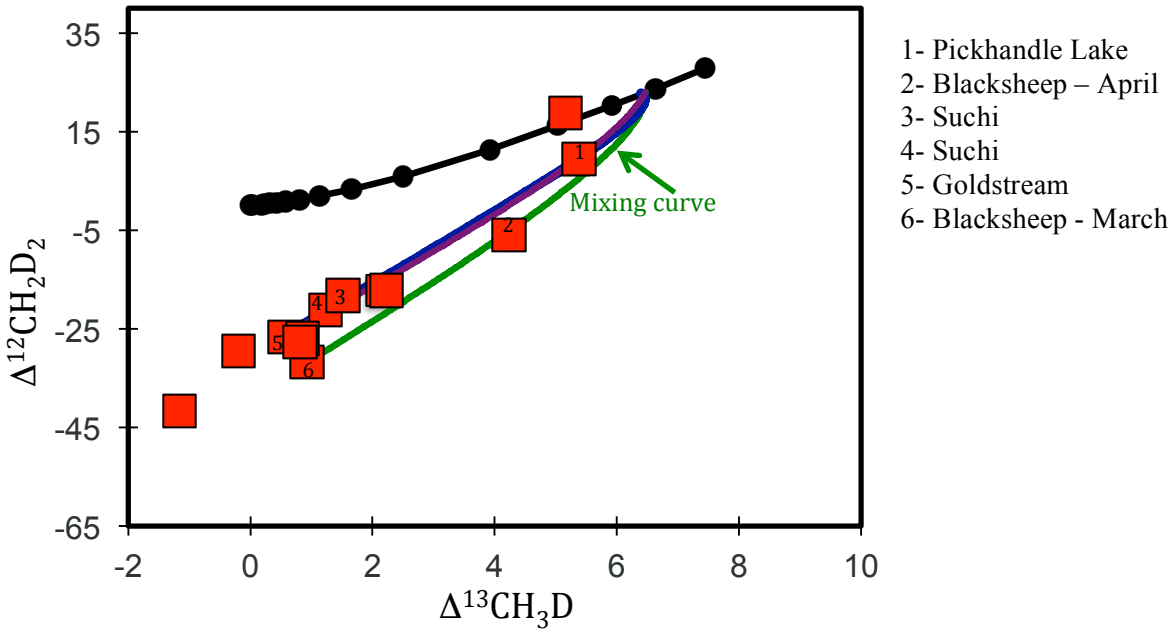

Figure 5- Two hypothetical mixing trajectories: (a) from the composition of the Blacksheep Lake (April, 2017) sample through the Blacksheep Lake (March, 2017) sample composition, (green curve), (b) from the composition of the Pickhandle Lake sample through the Goldstream Lake sample composition (purple or navy curves), calculated such that a gas equilibrated at 5°C is the mixing end member.

The abundances of potential electron acceptors to support AOM have been analyzed in two of the lakes, Blacksheep and Goldstream. Dissolved NO_3^-, SO_4^{2-}, and total Fe concentrations are shown in Figure 6, the concentration of dissolved CH_4 is shown in Figures 7 and 8. Fe (III) seems to be the dominant electron acceptor in Goldstream Lake, showing the highest concentration (Figure 9). However, more studies are needed on the effect of the concentration of electron acceptors on the incidence of AOM, along with the resulting doubly substituted isotopologue signatures of methane.

Goldstream

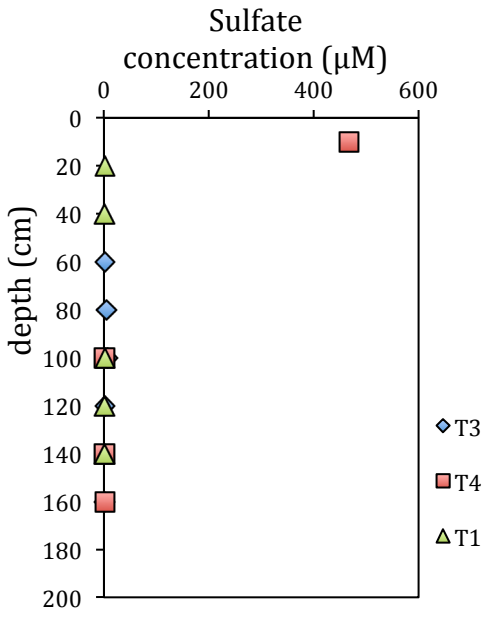

Goldstream

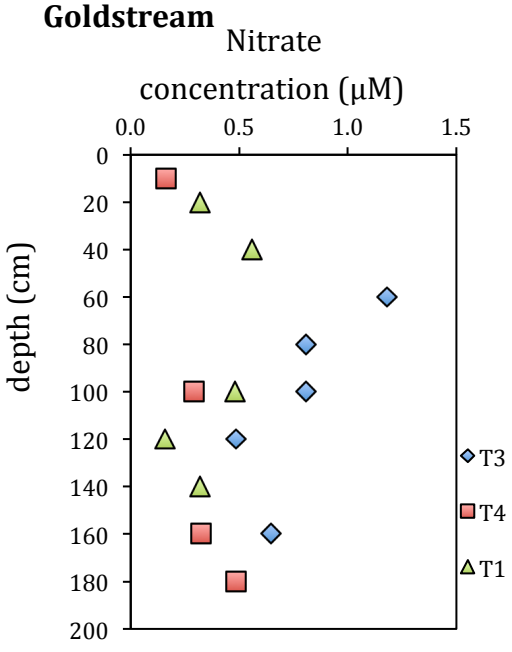

Blacksheep

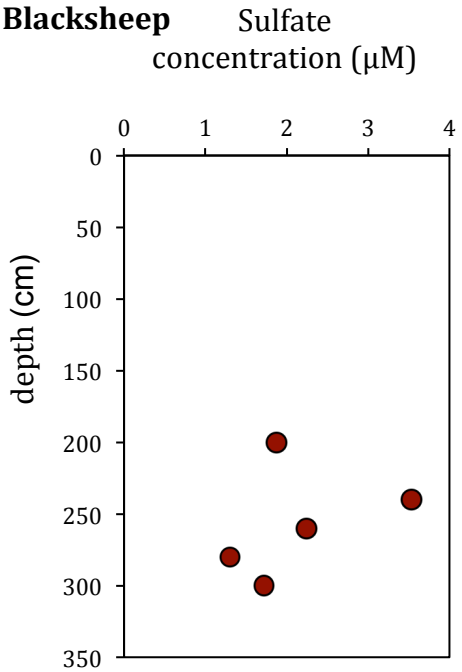

Blacksheep

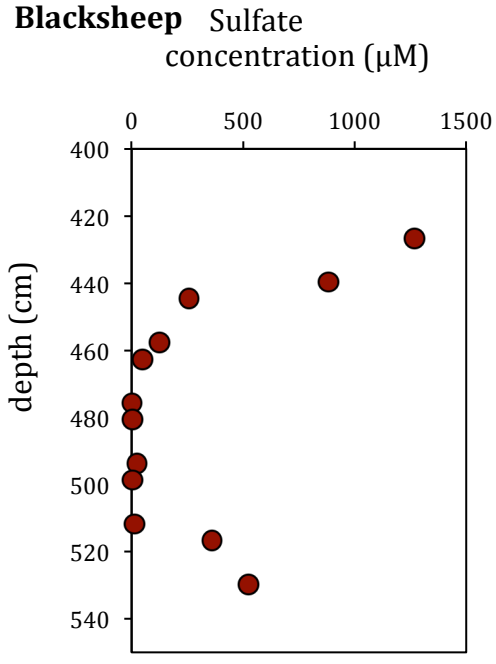

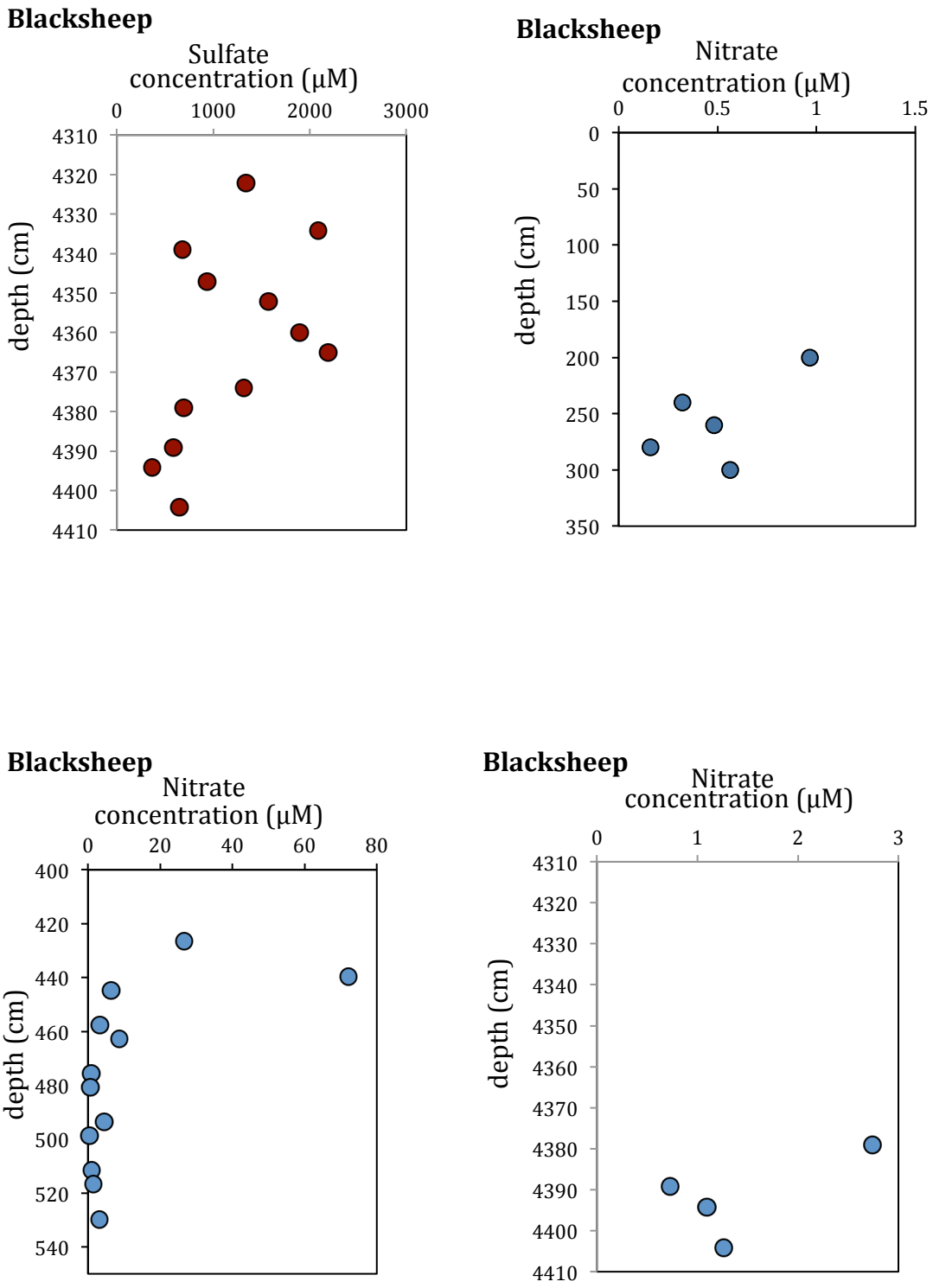

Figure 6- Dissolved concentration profiles of potential AOM electron acceptors, including NO_3^-, and SO_4^{2-} versus depth in the sediment in Goldstream (site T1, T3, and T4) and Blacksheep Lakes.

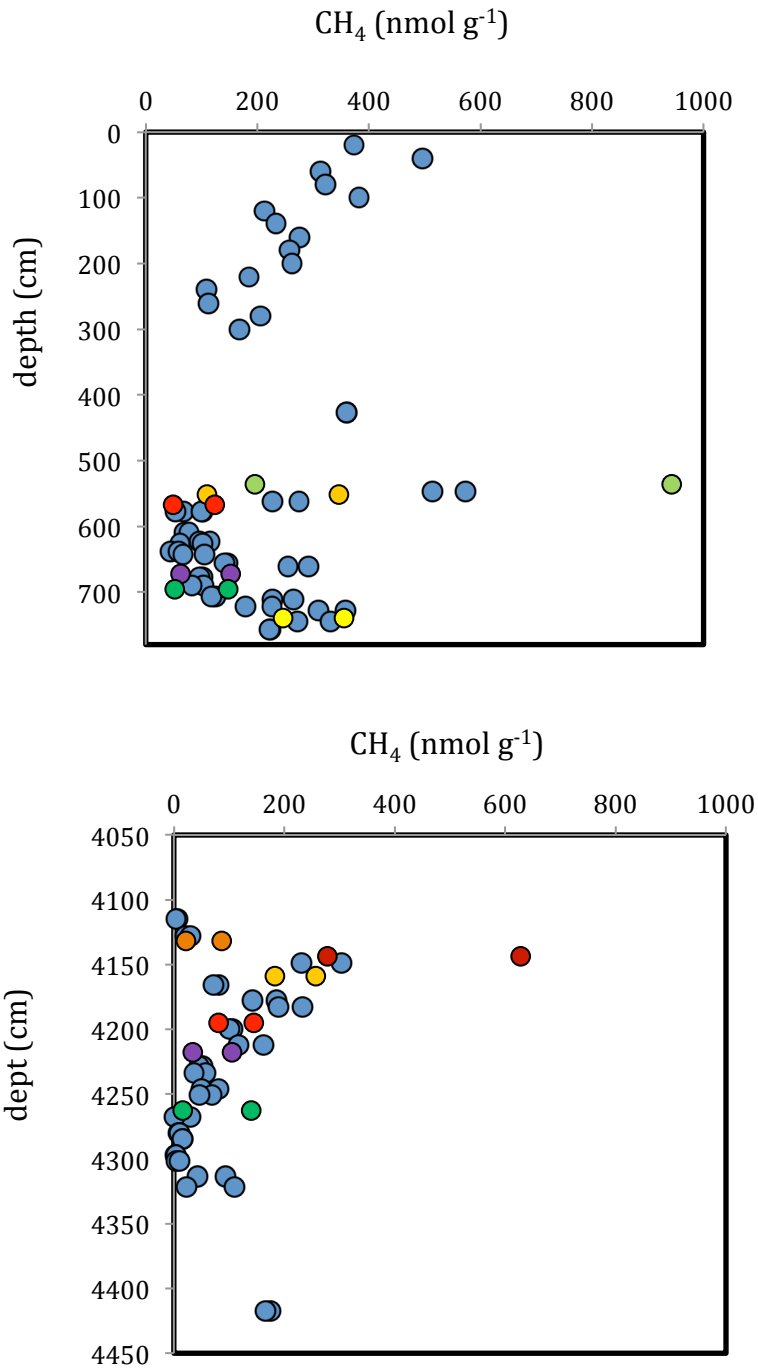

Figures 7- Concentration of dissolved CH_4 in different depths of Blacksheep Lake.

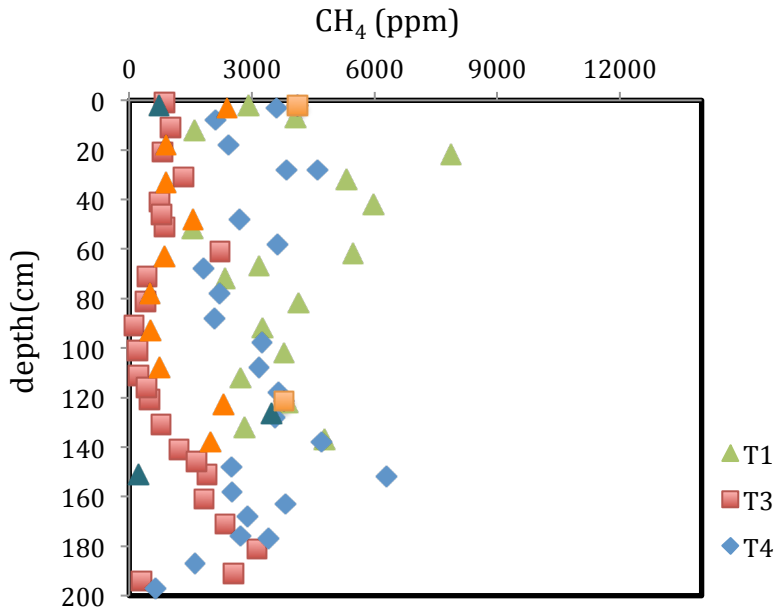
CH4 (ppm)
0
3000
6000
9000
12000
depth(cm)
0
20
40
60
80
100
120
140
160
180
200
T1
T3
T4

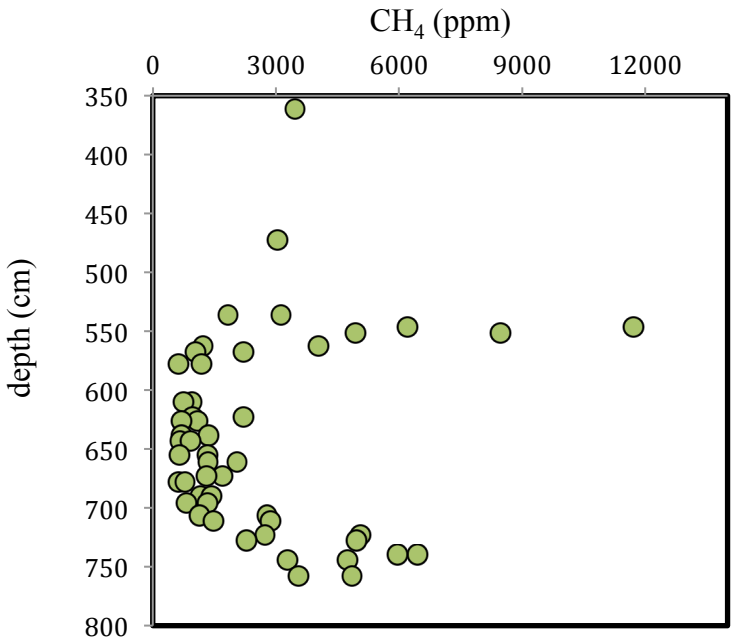
CH4 (ppm)
0
3000
6000
9000
12000
depth (cm)
350
400
450
500
550
600
650
700
750
800

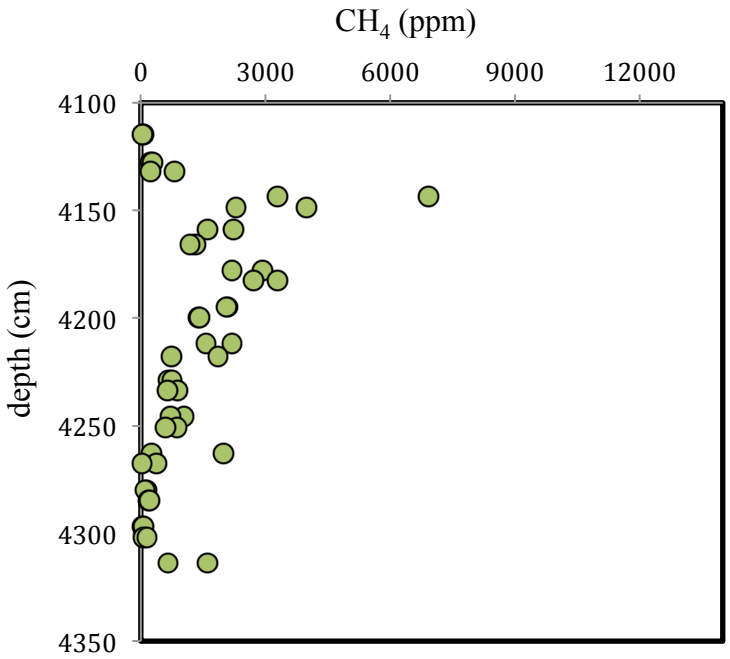

Figures 8- Concentration profile of dissolved CH_4 versus water depth in Goldstream Lake.

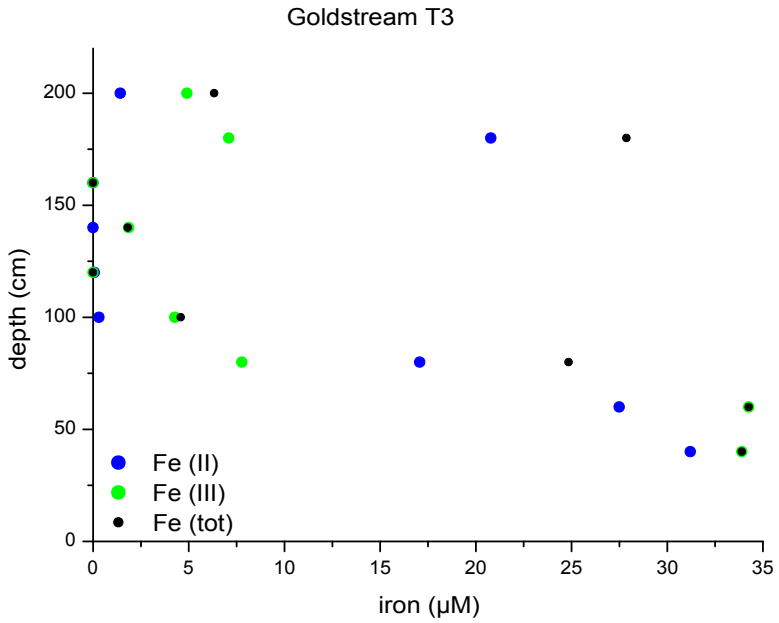

Figure 9- Dissolved concentration profile of Fe (potential AOM electron acceptor) versus depth in the sediment in Goldstream Lake - site T3 (Figure by Matthias Winkel).

As seen in Figure 10, three groups can be defined in our plot of $\Delta^{12}CH_2D_2$ vs. $\Delta^{13}CH_3D$: 1) the microbial array (produced by microbes through methanogenesis), which is close to the results from previous lab cultured samples, 2) the mixing array – samples falling near mixing curves between microbial samples and any end-member that has been equilibrated by AOM, and finally an AOM dominated (equilibrated) array.

Measured $\delta^{13}C$, δD, $\Delta^{13}CH_3D$, and $\Delta^{12}CH_2D_2$ values for all samples are shown in table 3.

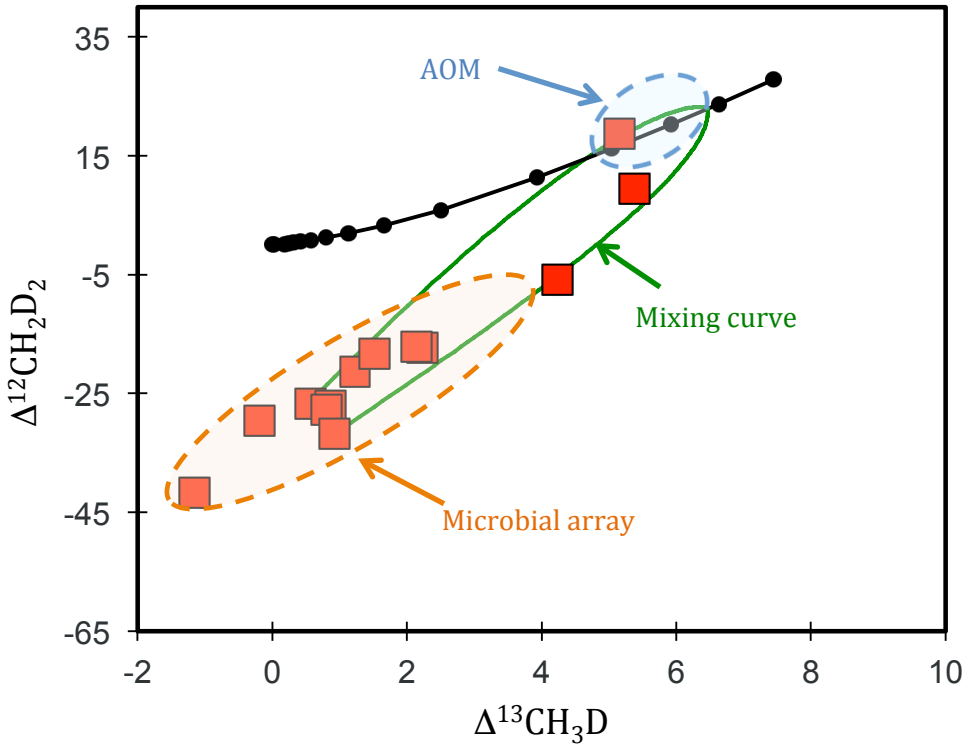

Figure 10- Hypothetical arrays: microbial array (brown curve) – the samples showing isotope signature of methanogenesis and resemble laboratory culture signatures, mixing (green curve) between this end-member (or range of possible end-members) and gas equilibrated at low temperatures by AOM (blue curve).

Table 3- Bulk and doubly substituted isotope signatures measured values for methane emitted from boreal natural lakes.

Lake	Region	$\delta^{13}C$ (‰)	δD (‰)	$\Delta^{13}CH_3D$(‰)	$\Delta^{12}CH_2D_2$(‰)
Blacksheep	Alaska	−62.6	−379.4	+0.9	−31.8
Blacksheep	Alaska	−82.1	−342.0	+4.2	−5.9
Cranberry	Alaska	−66.4	−367.8	+2.1	−17.2
Doughnut	Alaska	−55.5	−312.8	+5.2	+18.7
Goldstream	Alaska	−77.4	−397.1	+0.8	−27.7
Goldstream	Alaska	−61.2	−380.5	+0.6	−26.7
Octopus	Alaska	−73.3	−399.8	−1.2	−41.6
Vault	Alaska	−76.2	−408.0	−0.2	−29.6
Vault	Alaska	−70.9	−379.9	+0.9	−27.0
Golf	E. Canada	−71.1	−319.6	+2.2	−17.3
Pickhandle	W. Canada	−70.7	−346.1	+5.4	+9.4
Shuchi	Siberia	−84.0	−452.2	+1.2	−21.3
Shuchi	Siberia	−79.4	−419.2	+1.5	−18.2

Figures 11 and 12, respectively, present $\Delta^{13}CH_3D$ vs. $\delta^{13}C$ and δD. $\Delta^{12}CH_2D_2$ vs. $\delta^{13}C$ and δD are shown in Figures 13 and 14. Though there is not a strong correlation between doubly and singly substituted isotope signatures, the samples with highest values of $\Delta^{13}CH_3D$ and $\Delta^{12}CH_2D_2$ overall illustrate elevated values of δD (>−346‰) compared to the other samples. In contrast, $\delta^{13}C$ does not follow any clear pattern.

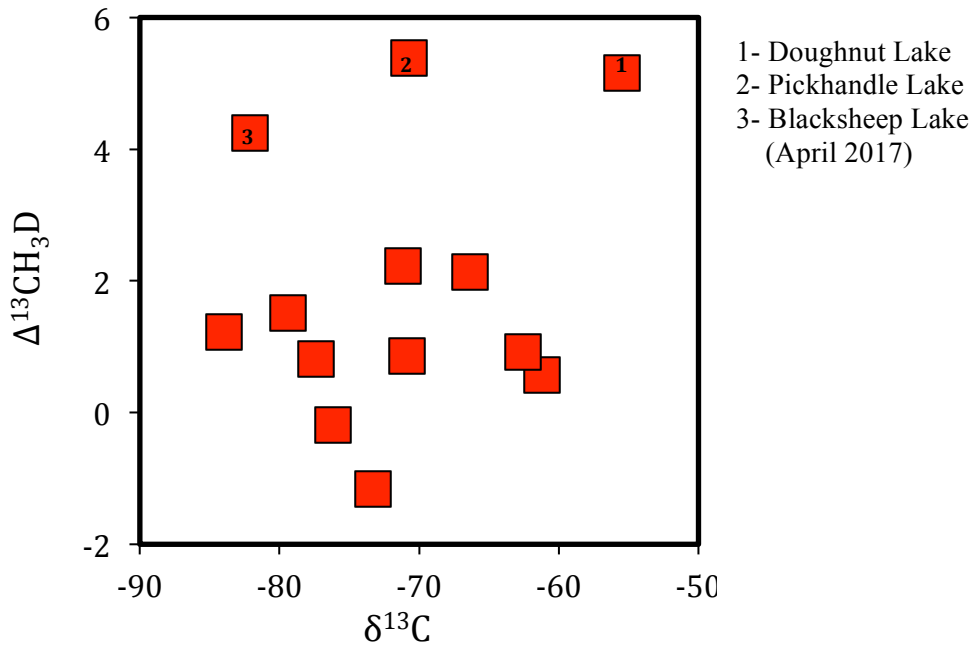

Figure 11- $\Delta^{13}CH_3D$ vs. $\delta^{13}C$ for all methane samples.

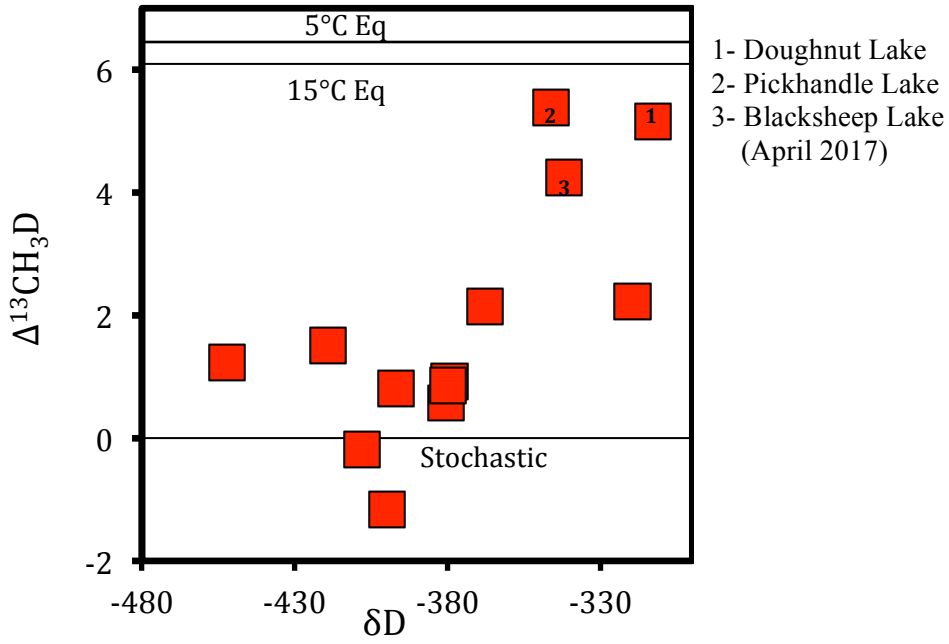

Figure 12- $\Delta^{13}CH_3D$ vs. δD for all methane samples.

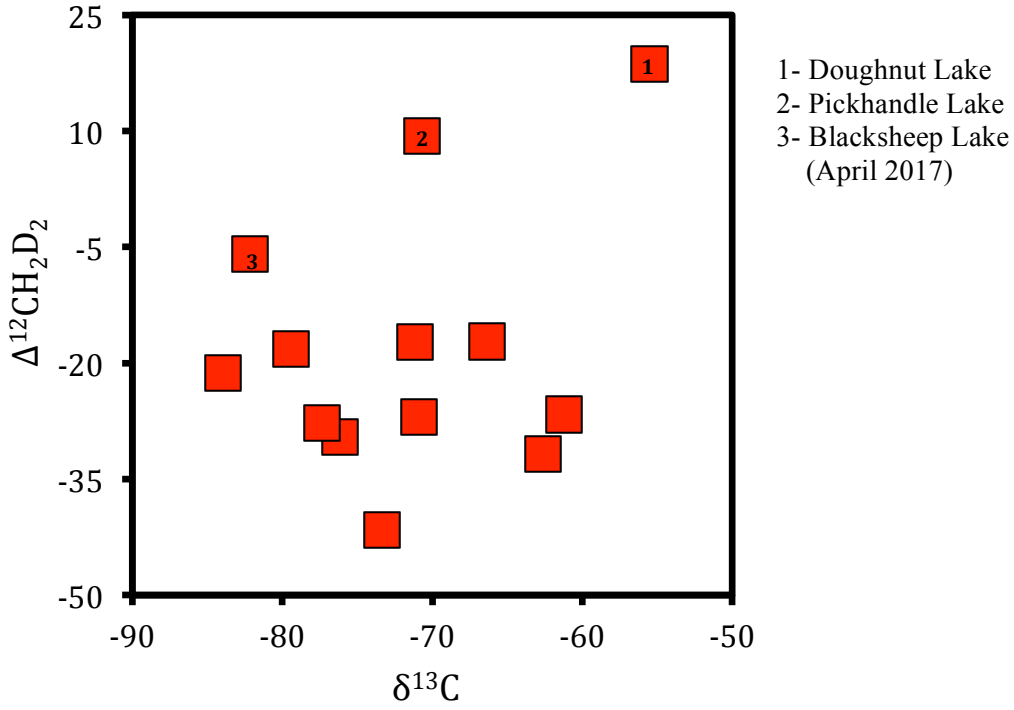

Figure 13- $\Delta^{12}CH_2D_2$ vs. $\delta^{13}C$ for all methane samples.

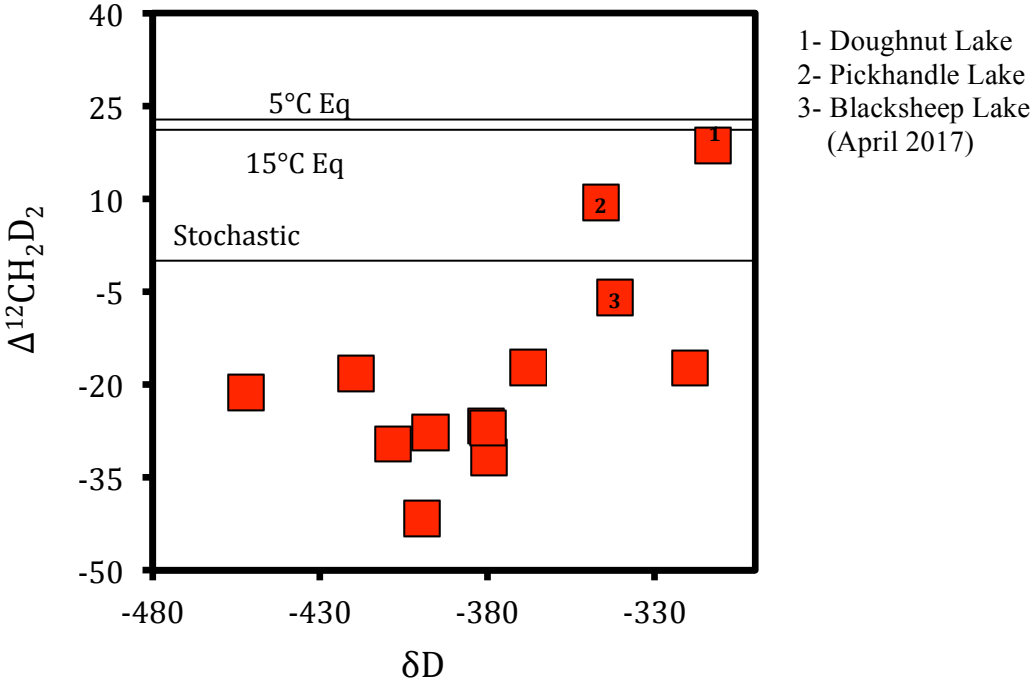

Figure 14- $\Delta^{12}CH_2D_2$ vs. δD for all methane samples.

3.2. Atmospheric methane model

3.2.1 Isotopologue budget for the atmosphere

We previously developed a theoretical one-box model to investigate the potential use of $^{13}CH_3D$ and $^{12}CH_2D_2$ as tools for tracking atmospheric methane sources and sinks [Haghnegahdar et al., 2017]. In that model, we used electronic structure methods to estimate kinetic isotope fractionations associated with the major sink reactions of CH_4 in air (reactions with OH and Cl radicals), and combined literature data with reconnaissance measurements of the relative abundances of $^{13}CH_3D$ and $^{12}CH_2D_2$ to estimate the compositions of the largest atmospheric sources. In this original model, we assumed equilibrium $\Delta^{13}CH_3D$ and $\Delta^{12}CH_2D_2$ for wetland sources. Our new measurements suggest that this assumption is incorrect; only one sample (Doughnut Lake) is close to equilibrium. In order to make a more realistic model of atmospheric methane budget containing both singly and doubly isotopes of methane, we assume our measured values for $\Delta^{13}CH_3D$ and $\Delta^{12}CH_2D_2$ of boreal lakes are representative of the global wetland methane source. This results in a shift of ~7‰ in $\Delta^{12}CH_2D_2$ and ~1‰ in $\Delta^{13}CH_3D$ of air at steady state including boreal and tropical wetlands. The newly estimated $\Delta^{13}CH_3D$ and $\Delta^{12}CH_2D_2$ values of air are +3.7‰ and +106.0‰ respectively; the net source compositions are respectively +3.3‰ and +5.1‰. We also made an alternate model assuming the least clumped composition, from Octopus Lake, as the net wetland source, as a sensitivity test. Figures 15 and 16 present a comparison between these results. This suggests that sink reactions play a more significant role in determining $^{12}CH_2D_2$ abundances (Figures15 and 16), whereas source compositions influence both $^{13}CH_3D$ and $^{12}CH_2D_2$.

Rice paddy sources of methane have also been classified as agricultural wetland sources [Bartlett and Harriss, 1992; Segers, 1997; Conrad 2002] as they share the same mechanisms and controls for methane emissions as natural wetlands. The production mechanism in both natural and agricultural wetlands is anaerobic methanogenesis through decomposition of organic materials [Bartlett and Harriss, 1992]. Consequently, we also applied the mean measured $\Delta^{13}CH_3D$ and $\Delta^{12}CH_2D_2$ of boreal lakes for rice paddies in our model. As the result, $\Delta^{12}CH_2D_2$ and $\Delta^{13}CH_3D$ of atmospheric at air steady state would be +98.3‰ and +2.9‰, respectively, a further decrease of ~8‰ and ~0.8‰ from the model with an equilibrated rice paddy source.

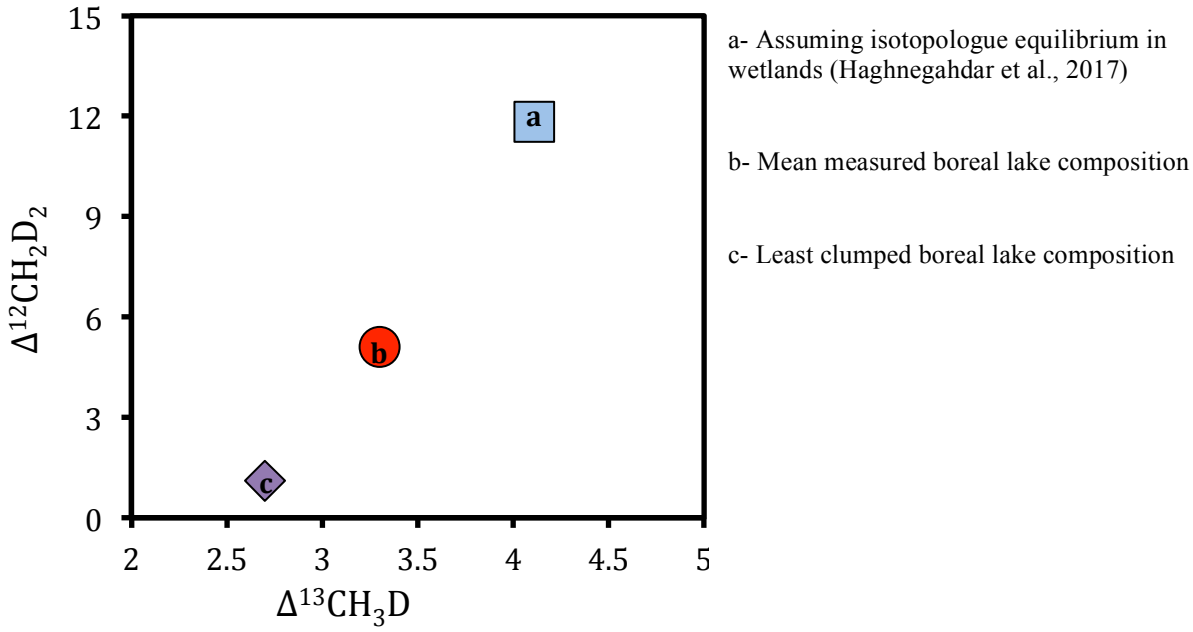

Figure 15- A comparison between doubly substituted isotopologues of atmospheric methane sources of original model assuming equilibrium in wetlands, applying the mean measured boreal lake values, and applying least clumped boreal lake values.

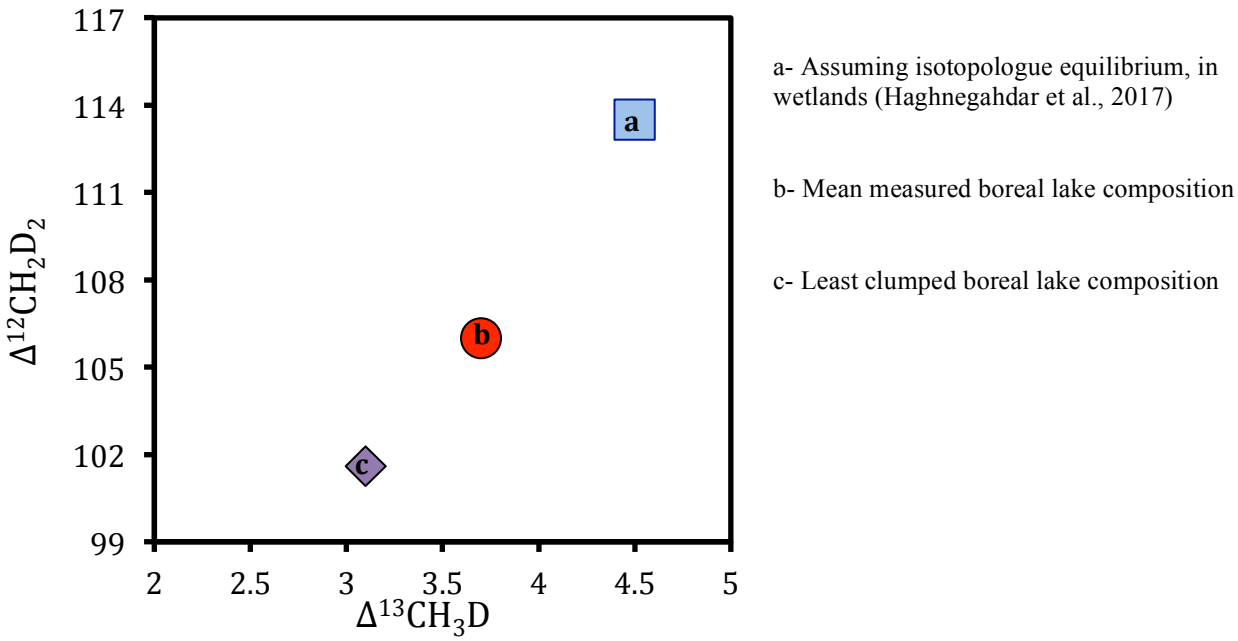

Figure 16- One-box model steady state of doubly substituted isotopologues of methane in air using original model assuming equilibrium in wetlands, applying the mean measured boreal lake values, and applying least clumped boreal lake values.

3.2.2 Sensitivity tests of isotoplogues

We manipulated our one-box model simulation to approximately reproduce changes in the atmospheric methane budget, starting from year 1890 with methane concentration of 836 ppb, and eventually reaching 1838 ppb in 2017. In this model, steady state is assumed before 1890. Then, emissions increase exponentially (0.81%/yr) from 1890 to 1990. From 1990 to 2006 a fixed (constant) source and sink is assumed (Figure 17).

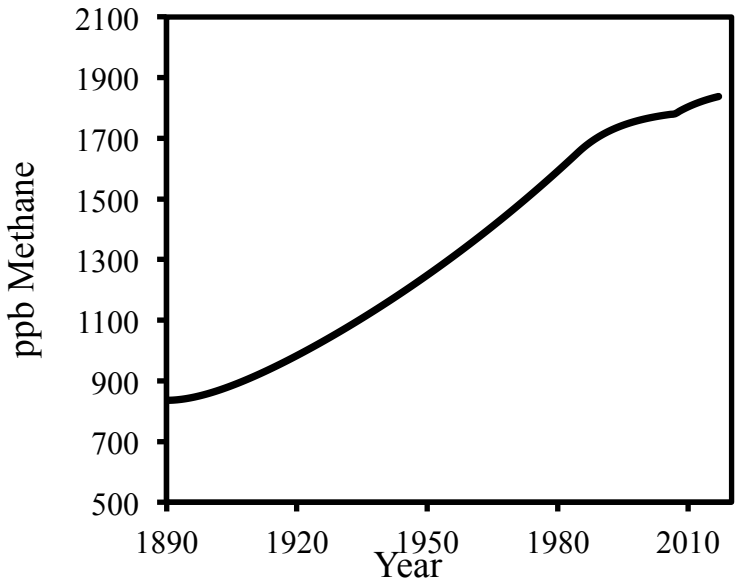

Figure 17- Model simulation of atmospheric methane concentration from year 1890 to 2017.

We constructed a sensitivity test for $\delta^{13}C$, δD, $\Delta^{13}CH_3D$ and $\Delta^{12}CH_2D_2$ in atmospheric methane along this time line by applying two different scenarios for renewed growth after 2007, following the approach of Turner et al. [2017] (Figure 18). In the first scenario, renewed growth is due to a one-time, instantaneous 20 Tg/yr increase in total emission of methane in the atmosphere in year 2007, assuming fixed atmospheric OH radical abundance (Figure 18-red dashed lines). In contrast, the second scenario assumes a 5% decrease in global mean OH radical concentration in the atmosphere in 2007 and fixed methane emissions (Figure 18-blue dashed line).

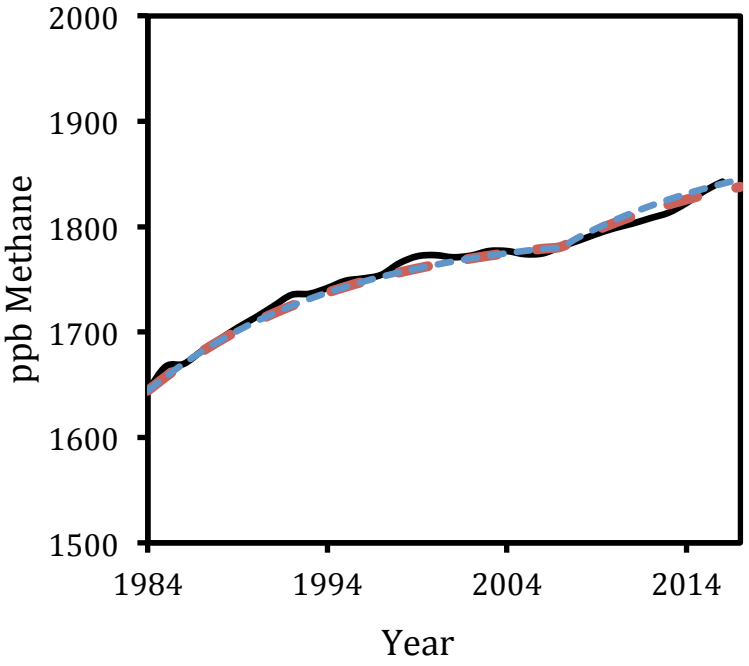

Figure 18- Atmospheric concentrations from reconstructed atmospheric methane budget compared to NOAA measurement records (solid black line), a 5% decrease in OH radical concentration in the atmosphere in year 2007 (blue dashed line) is difficult to distinguish from one time 20 Tg/yr increase in total sources emission (red dashed line).

In these models, $\Delta^{12}CH_2D_2$ decreased from 84.1‰ in 1985 to +78.6‰ in 2000 and then rose again to +83.1‰ in 2016 (Figure 19b). For $\Delta^{13}CH_3D$ the changes are not noticeable, raising from +2.72‰ in 1985 to +2.68 in 2000 then growing to +2.75‰ for the scenario of increasing emissions (Figure 19a, red dashed line) and 2.74‰ for the scenario of decreasing OH radical concentration (Figure 19d, blue dashed line). $\Delta^{12}CH_2D_2$ behaves the same in both scenarios; however, in comparison with $\delta^{13}C$ and δD it shows a sharper and more pronounced changes in the recent atmospheric methane trends.

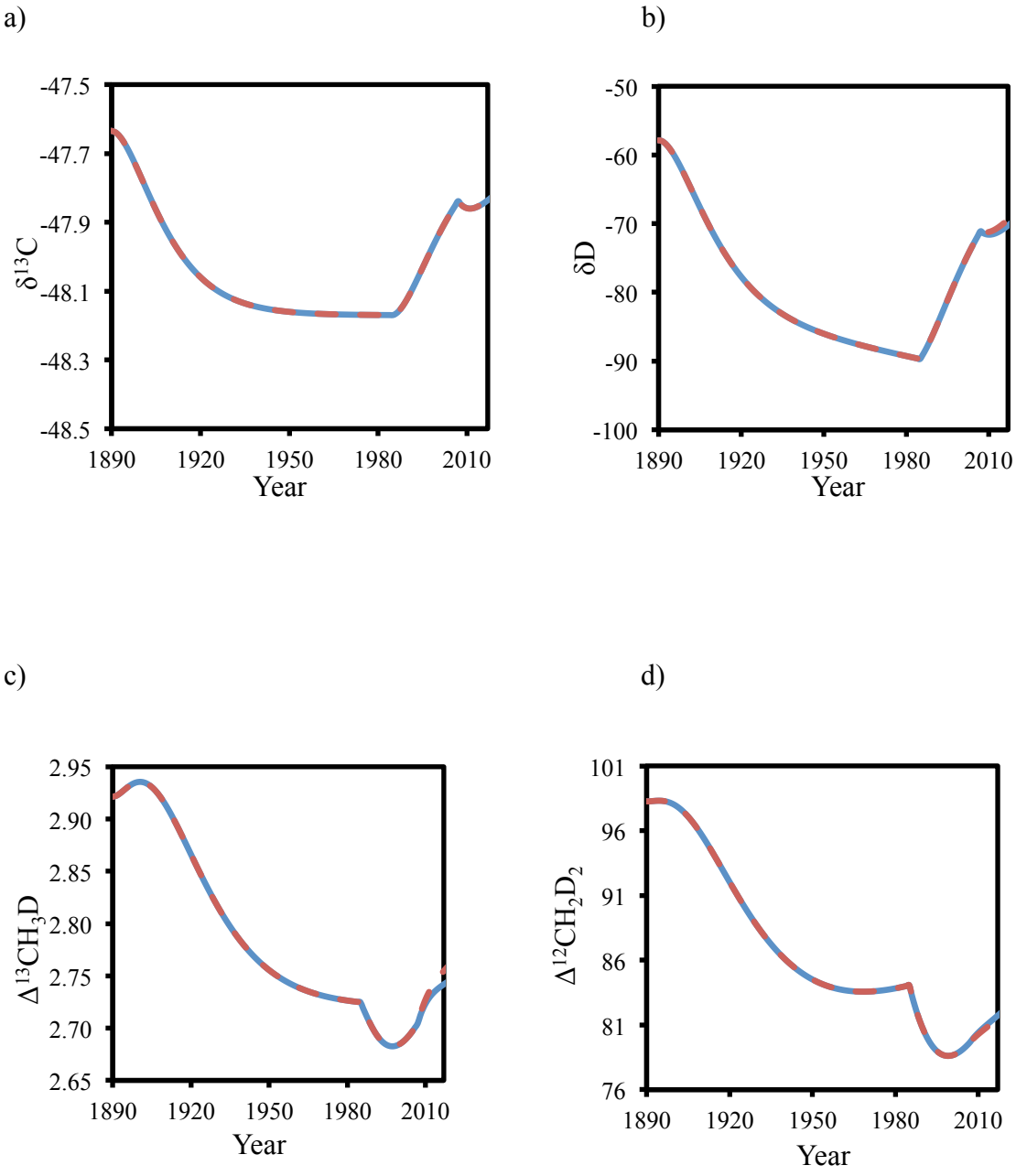

Figure 19- Singly and doubly substituted isotopologues of methane in the atmosphere (a) $\delta^{13}C$, (b) δD, (c) $\Delta^{13}CH_3D$, and (d) $\Delta^{12}CH_2D_2$ from 1890 to 2016. Red dashed line is based on a one time 20 Tg/yr increase in total emission of methane to the atmosphere in year 2007 and blue dashed line a decrease of 5% in OH radicals in the atmosphere in the same year.

3.2.3 Isolating the Impacts of Increasing Future Boreal Wetlands Fluxes

Annual emissions of methane from boreal lakes are predicted to continue rising through the end of this century [Chen et al., 2015; Wik et al., 2016]. We investigated the future impacts of increased boreal wetland emissions on the atmospheric methane budget through model $\Delta^{13}CH_3D$ and $\Delta^{12}CH_2D_2$ variations (Table 4). For this purpose, an exponential increase of 17 Tg/yr of methane emission from boreal wetlands by year 2100 was compared with a fixed emissions and sinks scenario. The model comparison predicts an approximately 2‰ difference in $\Delta^{12}CH_2D_2$ values (Figure 20b) relative to the fixed source and sink model. $\Delta^{13}CH_3D$ changes by less than ~0.1‰. δD displays an analogous behavior to $\Delta^{12}CH_2D_2$, but the response is on a shorter time scale - reaching a pseudo-steady state in ~50 years even with increasing boreal wetlands emission (Figure 20c). Likewise, $\delta^{13}C$ approaches a pseudo-steady state in ~50 years, with a total difference of just ~0.1‰. In this model $^{12}CH_2D_2$, compared to other isotopologues of methane, shows more sensitivity for tracking methane budget imbalances in the atmosphere.

Table 4- A model comparison between a fixed sources and sinks model from 2017 to 2100 and a scenario of a 17 Tg/yr gradual increase in boreal wetlands emission by 2100.

‰	2017	2100 (fixed)	17 Tg/yr gradual increase in boreal wetlands flux by 2100
$\delta^{13}C$	-47.8	-47.6	-47.6
δD	-69.4	-58.0	-59.7
$\Delta^{12}CH_2D_2$	81.5	97.1	95.6
$\Delta^{13}CH_3D$	2.8	2.9	2.9

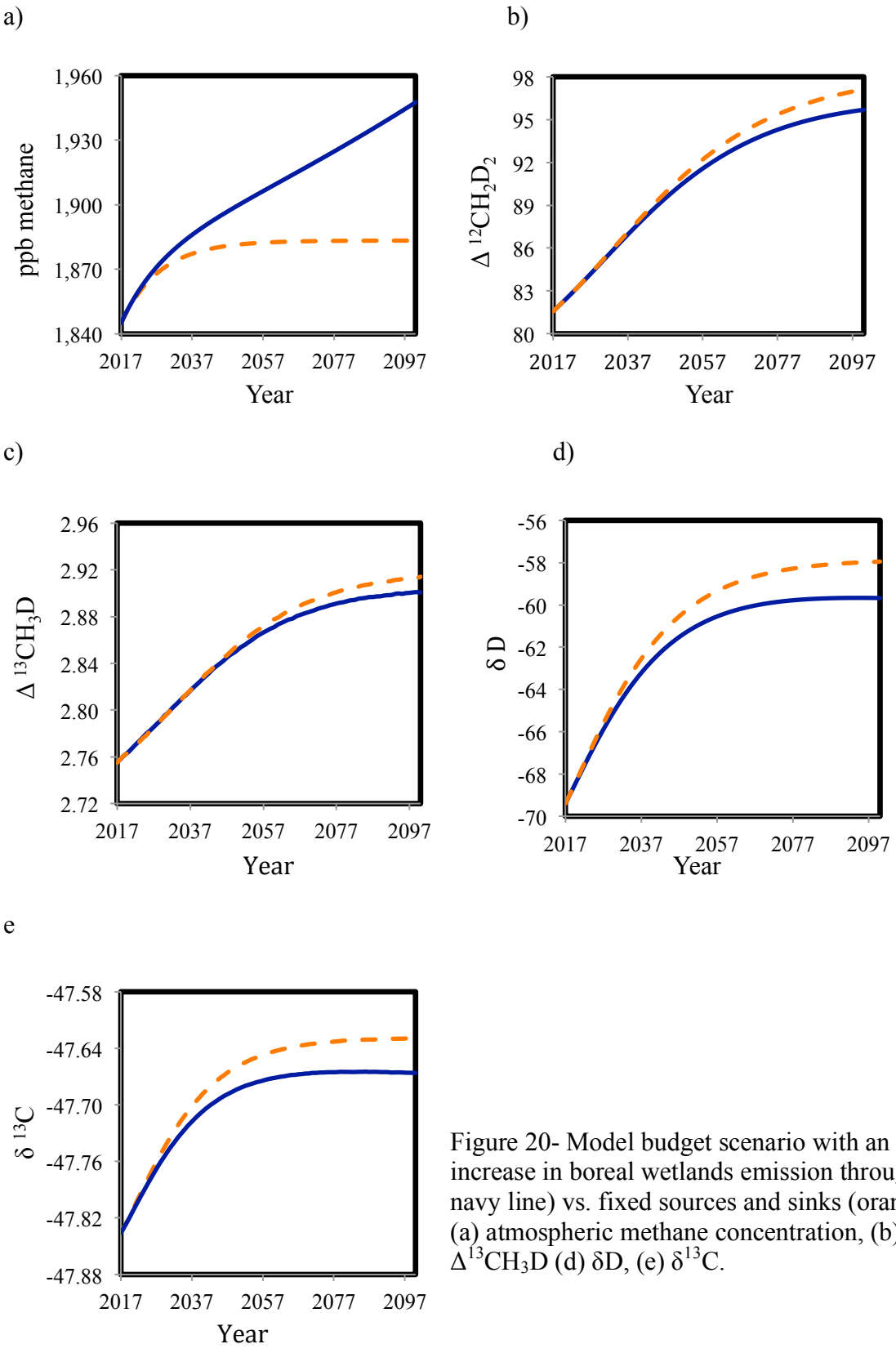

Figure 20- Model budget scenario with an exponential increase in boreal wetlands emission through 2100 (rigid navy line) vs. fixed sources and sinks (orange dashed line) (a) atmospheric methane concentration, (b) $\Delta^{12}CH_2D_2$, c) $\Delta^{13}CH_3D$ (d) δD, (e) $\delta^{13}C$.

4. Conclusions

For the first time, the abundances of both doubly substituted mass-18 methane isotopologues ($^{13}CH_3D$ and $^{12}CH_2D_2$, separately) of natural methane samples emitted from boreal lakes have been analyzed. These values in turn have been incorporated into a one-box model of the atmospheric methane budget including clumped isotopes signatures. The measured values for $\Delta^{12}CH_2D_2$ range from −41.6‰ to +18.7‰, while the range of $\Delta^{13}CH_3D$ is between −1.2‰ to +5.4‰. The values indicate that typical compositions fall within a microbial array with low, disequilibrium $\Delta^{12}CH_2D_2$ and $\Delta^{13}CH_3D$. Clumped isotope signatures of three lakes (Doughnut, Pickhandle, and Blacksheep – April sample) are closer to the equilibrium isotopologue distribution. These three samples likely were affected by AOM (Anaerobic Methane Oxidation by methanotrophs). The observed doubly substituted isotopologue signatures in these lakes could be the result of mixing between methanogenesis and gas equilibrated by methanothrophy. It is expected [Haghnegahdar et al., 2017] that sink reactions will play a more significant role in determining the $\Delta^{12}CH_2D_2$ in atmospheric methane than source variations, generating a distinctly elevated signature (by ~100‰) relative to the source composition. Our model isotopologue budget for the atmosphere predicts ~2‰ effect on both $\Delta^{12}CH_2D_2$ and δD as the result of a gradual rise of 17 Tg/yr in boreal wetland methane emissions by 2100, relative to a constant sources scenario. This sensitivity suggests a potential of $\Delta^{12}CH_2D_2$ measurements for tracking changes in the atmospheric methane budget.

References

Alei, M., Cappis, J.H., Fowler, M.M., Frank, D.J., Goldblatt, M., Guthals, P.R., Mason, A.S., Mills, T.R., Mroz, E.J., Norris, T.L., Perrin, R.E., Poths, J., Rokop, D.J., Shields, W.R., 1987. Determination of deuterated methanes for use as atmospheric tracers. Atmos. Environ. 21, 909–915. doi:10.1016/0004-6981(87)90087-4

Bartlett, K.B., Harriss, R.C., 1993. Reveiw and Assessment of Methane Emissions from Wetlands. Chemosphere 26, 261–320.

Bastviken, D., Tranvik, L.J., Downing, J., Crill, J. a, M, P., Enrich-prast, A., 2011. the Continental Carbon Sink. Science (80-.). 331, 50. doi:10.1126/science.1196808

Bloom, A.A., Palmer, P.I., Fraser, A., Reay, D.S., Frankenberg, C., 2010. Large-Scale Controls of Methanogenesis Inferred from Methane and Gravity Spaceborne Data. Science (80-.). 327, 322–325. doi:10.1038/nchem.467

Burke, 1993. Possible Influence of Hydrogen Concentration on Microbial Methane Stable. Chemosphere 26, 55–67. doi:10.1016/0045-6535(93)90412-X

Cao, X., Liu, Y., 2012. Theoretical estimation of the equilibrium distribution of clumped isotopes in nature. Geochim. Cosmochim. Acta 77, 292–303. doi:10.1016/j.gca.2011.11.021

Chen, X., Bohn, T.J., Lettenmaier, D.P., 2015. Model estimates of climate controls on pan-Arctic wetland methane emissions. Biogeosciences 12, 6259–6277. doi:10.5194/bg-12-6259-2015

Cicerone, R.J., Oremland, R.S., 1988. Biogeochemical Aspects of Atmospheric Methane. Global Biogeochem. Cycles 2, 299–327.

Conrad, R., 2002. Control of microbial methane production in wetland rice fields 59–69.

Douglas, P.M.J., Stolper, D.A., Smith, D.A., Walter Anthony, K.M., Paull, C.K., Dallimore, S., Wik, M., Crill, P.M., Winterdahl, M., Eiler, J.M., Sessions, A.L., 2016. Diverse origins of Arctic and Subarctic methane point source emissions identified with multiply-substituted isotopologues. Geochim. Cosmochim. Acta 188, 163–188. doi:10.1016/j.gca.2016.05.031

Fisher, R.E., France, J.L., Lowry, D., Lanoisellé, M., Brownlow, R., Pyle, J.A., Cain, M., Warwick, N., Skiba, U.M., Drewer, J., Dinsmore, K.J., Leeson, S.R., Bauguitte, S.J.B., Wellpott, A., O'Shea, S.J., Allen, G., Gallagher, M.W., Pitt, J., Percival, C.J., Bower, K., George, C., Hayman, G.D., Aalto, T., Lohila, A., Aurela, M., Laurila, T., Crill, P.M., McCalley, C.K., Nisbet, E.G., 2017. Measurement of the 13C isotopic signature of methane emissions from northern European wetlands. Global Biogeochem. Cycles 31, 605–623. doi:10.1002/2016GB005504

Giunta, T., Young, E. D., Warr, O., Kohl, I., Ash, J. L., Martini, A., Mundle, S. O C., Rumble, D., Wasley, M., Larowe, D. E., Gilbert, A., Sherwood, B.Sherwood, B. (2019). ScienceDirect Methane sources and sinks in continental sedimentary systems : New insights from paired clumped isotopologues, *245*, 327–351. https://doi.org/10.1016/j.gca.2018.10.030

Jorgenson, M.T., Shur, Y.L., Pullman, E.R., 2006. Abrupt increase in permafrost degradation in Arctic Alaska. Geophys. Res. Lett. 33, 2–5. doi:10.1029/2005GL024960

Haghnegahdar, M.A., Schauble, E.A., Young, E.D., 2017. A model for12CH2D2and13CH3D as complementary tracers for the budget of atmospheric CH4. Global Biogeochem. Cycles 31, 1387–1407. doi:10.1002/2017GB005655

Harriss, R., Bartlett, K., Frolking, S., Crill, P., 1993. Methane Emissions from Northern High-Latitude Wetlands. Biogeochem. Glob. Chang. 449–486. doi:10.1007/978-1-4615-2812-8_25

Kaye, J.A., Jackman, C.H., 1990. Comment on "detection of multiply deuterated methane 17, 659–660.

Khalil, M.A.K., Butenhoff, C.L., Rasmussen, R.A., 2007. Atmospheric methane: Trends and cycles of sources and sinks. Environ. Sci. Technol. 41, 2131–2137. doi:10.1021/es061791t

Kirschke, S. (2013). Three decades of global methane sources and sinks, *28*(September). https://doi.org/10.1038/NGEO1955

Lollar, B.S., Lacrampe-Couloume, G., Slater, G.F., Ward, J., Moser, D.P., Gihring, T.M., Lin, L.H., Onstott, T.C., 2006. Unravelling abiogenic and biogenic sources of methane in the Earth's deep subsurface. Chem. Geol. 226, 328–339. doi:10.1016/j.chemgeo.2005.09.027

Ma, Q., Wu, S., Tang, Y., 2008. Formation and abundance of doubly-substituted methane isotopologues (13CH3D) in natural gas systems. Geochim. Cosmochim. Acta 72, 5446–5456. doi:10.1016/j.gca.2008.08.014

Mroz, E.J., Alei, M., Cappis, J.H., Guthals, P.R., Mason, A.S., Rokop, D.J., 1989. presence of either of the natural isotopic abundances We found that release had an average Antarctica using fully deuterated as conservative tracers of atmospheric while we again Following the January and June releases Many of these samples were analyzed 16, 677–678.

Martinez-cruz, K., Sepulveda-jauregui, A., Casper, P., Walter, K., Smemo, K. A., & Thalasso, F. (2018). Ubiquitous and signi fi cant anaerobic oxidation of methane in freshwater lake sediments. *Water Research*, *144*(2), 332–340.

Martinez-cruz, K., Leewis, M., Charold, I., Sepulveda-jauregui, A., Walter, K., Thalasso, F., & Beth, M. (2017). Science of the Total Environment Anaerobic oxidation of methane by aerobic methanotrophs in sub-Arctic lake sediments. *Science of the Total Environment*, *607–608*, 23–31.

Martinez-cruz, K., Sepulveda-jauregui, A., Casper, P., Walter, K., Smemo, K. A., & Thalasso, F. (2018). Ubiquitous and signi fi cant anaerobic oxidation of methane in freshwater lake sediments. *Water Research*, *144*(2), 332–340. https://doi.org/10.1016/j.watres.2018.07.053

Nisbet, E.G., Dlugokencky, E.J., Manning, M.R., Lowry, D., Fisher, R.E., France, J.L., Michel, S.E., Miller, J.B., White, J.W.C., Vaughn, B., Bousquet, P., Pyle, J.A., Warwick, N.J., Cain, M., Brownlow, R., Zazzeri, G., Lanoisellé, M., Manning, A.C., Gloor, E., Worthy, D.E.J., Brunke, E., Labuschagne, C., Wolff, E.W., Ganesan, A.L., 2016. Global Biogeochemical Cycles 1–15. doi:10.1002/2016GB005406.Received

Olefeldt, D., Turetsky, M.R., Crill, P.M., Mcguire, A.D., 2013. Environmental and physical controls on northern terrestrial methane emissions across permafrost zones. Glob. Chang. Biol. 19, 589–603. doi:10.1111/gcb.12071

Piasecki, A., Sessions, A., Peterson, B., Eiler, J., 2016. Prediction of equilibrium distributions of isotopologues for methane, ethane and propane using density functional theory. Geochim. Cosmochim. Acta. doi:10.1016/j.gca.2016.06.003

Rice, A.L., Butenhoff, C.L., Teama, D.G., Röger, F.H., Khalil, M.A.K., Rasmussen, R.A., 2016. Atmospheric methane isotopic record favors fossil sources flat in 1980s and 1990s with recent increase. Proc. Natl. Acad. Sci. 113, 10791–10796. doi:10.1073/pnas.1522923113

Riley, W. J., Subin, Z. M., Lawrence, D. M., Swenson, S. C., Torn, M. S., Meng, L., … Hess, P. (2011). Barriers to predicting changes in global terrestrial methane fluxes : analyses using CLM4Me , a methane biogeochemistry model integrated in CESM, 1925–1953. https://doi.org/10.5194/bg-8-1925-2011

Saunois, M., Bousquet, P., Poulter, B., Peregon, A., Ciais, P., Canadell, J.G., Dlugokencky, E.J., Etiope, G., Bastviken, D., Houweling, S., Janssens-Maenhout, G., Tubiello, F.N., Castaldi, S., Jackson, R.B., Alexe, M., Arora, V.K., Beerling, D.J., Bergamaschi, P., Blake, D.R., Brailsford, G., Brovkin, V., Bruhwiler, L., Crevoisier, C., Crill, P., Covey, K., Curry, C., Frankenberg, C., Gedney, N., Höglund-Isaksson, L., Ishizawa, M., Ito, A., Joos, F., Kim, H.S., Kleinen, T., Krummel, P., Lamarque, J.F., Langenfelds, R., Locatelli, R., Machida, T., Maksyutov, S., McDonald, K.C., Marshall, J., Melton, J.R., Morino, I., Naik, V., O'Doherty, S., Parmentier, F.J.W., Patra, P.K., Peng, C., Peng, S., Peters, G.P., Pison, I., Prigent, C., Prinn, R., Ramonet, M., Riley, W.J., Saito, M., Santini, M., Schroeder, R., Simpson, I.J., Spahni, R., Steele, P., Takizawa, A., Thornton, B.F.,

Tian, H., Tohjima, Y., Viovy, N., Voulgarakis, A., Van Weele, M., Van Der Werf, G.R., Weiss, R., Wiedinmyer, C., Wilton, D.J., Wiltshire, A., Worthy, D., Wunch, D., Xu, X., Yoshida, Y., Zhang, B., Zhang, Z., Zhu, Q., 2016. The global methane budget 2000-2012. Earth Syst. Sci. Data 8, 697–751. doi:10.5194/essd-8-697-2016

Schaefer, H., Fletcher, S.E.M., Veidt, C., Lassey, K.R., Brailsford, G.W., Bromley, T.M., Dlugokencky, E.J., Michel, S.E., Miller, J.B., Levin, I., Lowe, D.C., Martin, R.J., Vaughn, B.H., White, J.W.C., 2016. A 21st-century shift from fossil-fuel to biogenic methane emissions indicated by13CH4. Science (80-.). 352, 80–84. doi:10.1126/science.aad2705

Segers, R., 1998. Methane production and methane consumption : a review of processes underlying wetland methane fluxes 23–51.

Stolper, D.A., Lawson, M., Davis, C.L., Ferreira, A.A., Santos Neto, E. V, Ellis, G.S., Lewan, M.D., Martini, A.M., Tang, Y., Schoell, M., Sessions, A.L., Eiler, J.M., 2014. Formation temperatures of thermogenic and biogenic methane. Science 344, 1500–3. doi:10.1126/science.1254509

Stolper, D.A., Martini, A.M., Clog, M., Douglas, P.M., Shusta, S.S., Valentine, D.L., Sessions, A.L., Eiler, J.M., 2015. Distinguishing and understanding thermogenic and biogenic sources of methane using multiply substituted isotopologues. Geochim. Cosmochim. Acta 161, 219–247. doi:10.1016/j.gca.2015.04.015

Stolper, D.A., Sessions, A.L., Ferreira, A.A., Santos Neto, E. V., Schimmelmann, A., Shusta, S.S., Valentine, D.L., Eiler, J.M., 2014. Combined 13C-D and D-D clumping in methane: Methods and preliminary results. Geochim. Cosmochim. Acta 126, 169–191. doi:10.1016/j.gca.2013.10.045

Tan, Z., Zhuang, Q., 2015. Arctic lakes are continuous methane sources to the atmosphere under warming conditions. Environ. Res. Lett. 10, 1–9. doi:10.1088/1748-9326/10/5/054016

Tsuji, K., Teshima, H., Sasada, H., Yoshida, N., 2012. Spectroscopic isotope ratio measurement of doubly-substituted methane. Spectrochim. Acta - Part A Mol. Biomol. Spectrosc. 98, 43–46. doi:10.1016/j.saa.2012.08.028

Turetsky, M.R., Kotowska, A., Bubier, J., Dise, N.B., Crill, P., Hornibrook, E.R.C., Minkkinen, K., Moore, T.R., Myers-Smith, I.H., Nykänen, H., Olefeldt, D., Rinne, J., Saarnio, S., Shurpali, N., Tuittila, E.S., Waddington, J.M., White, J.R., Wickland, K.P., Wilmking, M., 2014. A synthesis of methane emissions from 71 northern, temperate, and subtropical wetlands. Glob. Chang. Biol. 20, 2183–2197. doi:10.1111/gcb.12580

Turner, A.J., Frankenberg, C., Wennberg, P.O., Jacob, D.J., 2017. Ambiguity in the causes for decadal trends in atmospheric methane and hydroxyl. Proc. Natl. Acad.

Sci. 114, 5367–5372. doi:10.1073/pnas.1616020114

Valentine, D.L., Chidthaisong, A., Rice, A., Reeburgh, W.S., Tyler, S.C., 2004. Carbon and hydrogen isotope fractionation by moderately thermophilic methanogens. Geochim. Cosmochim. Acta 68, 1571–1590. doi:10.1016/j.gca.2003.10.012

Walter, K.M., Chanton, J.P., Chapin, F.S., Schuur, E.A.G., Zimov, S.A., 2008. Methane production and bubble emissions from arctic lakes: Isotopic implications for source pathways and ages. J. Geophys. Res. Biogeosciences 113. doi:10.1029/2007JG000569

Walter, K.M., Zimov, S.A., Chanton, J.P., Verbyla, D., Chapin, F.S., 2006. Methane bubbling from Siberian thaw lakes as a positive feedback to climate warming. Nature 443, 71–75. doi:10.1038/nature05040

Wang, D.T., Gruen, D.S., Lollar, B.S., Hinrichs, K.-U., Stewart, L.C., Holden, J.F., Hristov, A.N., Pohlman, J.W., Morrill, P.L., Könneke, M., Delwiche, K.B., Reeves, E.P., Sutcliffe, C.N., Ritter, D.J., Seewald, J.S., McIntosh, J.C., Hemond, H.F., Kubo, M.D., Cardace, D., Hoehler, T.M., Ono, S., 2015. Methane cycling. Nonequilibrium clumped isotope signals in microbial methane. Science 348, 428–31. doi:10.1126/science.aaa4326

Webb, M.A., Miller, T.F., 2014. Position-specific and clumped stable isotope studies: Comparison of the urey and path-integral approaches for carbon dioxide, nitrous oxide, methane, and propane. J. Phys. Chem. A 118, 467–474. doi:10.1021/jp411134v

Whalen, S.C., 2005. Natural Wetlands and the Atmosphere. Environ. Eng. Sci. 22, 73–94. doi:10.1089/ees.2005.22.73 doi:10.1016/S0009-2541(99)00092-3

Whiticar, M.J., Faber, E., Schoell, M., 1986. Biogenic methane formation in marine and freshwater environments: CO2 reduction vs. acetate fermentation-Isotope evidence. Geochim. Cosmochim. Acta 50, 693–709. doi:10.1016/0016-7037(86)90346-7

Wik, M., Varner, R.K., Anthony, K.W., MacIntyre, S., Bastviken, D., 2016. Climate-sensitive northern lakes and ponds are critical components of methane release. Nat. Geosci. 9, 99–105. doi:10.1038/ngeo2578

Wuebbles, D.J., Hayhoe, K., 2002. Atmospheric methane and global change. Earth-Science Rev. 57, 177–210. doi:10.1016/S0012-8252(01)00062-9

Young, E.D., Rumble, D., Freedman, P., Mills, M., 2016. A large-radius high-mass-resolution multiple-collector isotope ratio mass spectrometer for analysis of rare isotopologues of O2, N2, CH4 and other gases. Int. J. Mass Spectrom. 401, 1–10. doi:10.1016/j.ijms.2016.01.006

Young, E.D., Kohl, I.E., Sherwood Lollar, B., Etiope, G., Rumble III, D., Li, S., Haghnegahdar, M. a., Schauble, E. a., Mccain, K. a, Foustoukos, D.I., Sutclife, C., Warr, O., Onstott, T.C., Hosgormez, H., Neubeck, a, Marques, J.M., Rowe, R., Larowe, D.E., Bryndzia, T., 2017. The relative abundances of resolved 12 CH 2 D 2 and 13 CH 3 D and mechanisms controlling isotopic bond ordering in abiotic and biotic methane gases. Geochim. Cosmochim. Acta 203, 235–264. doi:10.1016/j.gca.2016.12.041